

7. (P.J.V.)

Measurement of τ Production and Decay Parameters with the Process

$$e^+e^- \rightarrow Z^0 \rightarrow \tau^+\tau^-; \tau \rightarrow \mu\nu_\tau\nu_\mu$$

CERN LIBRARIES, GENEVA



CM-P00048015

Dissertation
zur Erlangung des Grades
"Doktor der Naturwissenschaften"
am Fachbereich Physik
der Johannes-Gutenberg-Universität
in Mainz

Steffen Roehn
geboren in Mainz

Mainz 1991

Thesis-1991-Roehn

**Measurement of τ Production and
Decay Parameters with the Process**

$$e^+e^- \rightarrow Z^0 \rightarrow \tau^+\tau^-; \tau \rightarrow \mu\nu_\tau\nu_\mu$$

Dissertation
zur Erlangung des Grades
"Doktor der Naturwissenschaften"
am Fachbereich Physik
der Johannes-Gutenberg-Universität
in Mainz

Steffen Roehn
geboren in Mainz

Mainz 1991

1. Gutachter: Prof. Dr. K. Kleinknecht
2. Gutachter: Prof. Dr. H. G. Sander

Tag der Einreichung: 17. Mai 1991
Tag der mündlichen Prüfung: 26. Juni 1991

Contents

1	Introduction and Summary	1
2	τ Production and Decay	7
2.1	Production of $\tau^+\tau^-$ in e^+e^- -Annihilation	7
2.2	Asymmetries A_{FB} , A_{pol} and A_{pol}^{FB}	10
2.3	Determination of Couplings from Γ_{ll} and A_{FB}	13
2.4	τ Decay	14
2.4.1	$\tau^- \rightarrow \pi^- \nu$	15
2.4.2	$\tau^- \rightarrow \mu^- \nu \nu, e^- \nu \nu$	15
2.4.3	$\tau^- \rightarrow \rho^- \nu$ and $\tau^- \rightarrow a_1 \nu$	16
2.4.4	Comparison of Different Decay Channels	18
2.5	Observables A_τ , A_e , ξ , ρ and δ in $\tau \rightarrow \mu \nu \nu$ Decays	18
2.5.1	Dependence of the Momentum Spectrum on Polarization and Lorentz-Structure	19
2.5.2	Angular Information	22
2.6	Radiative Corrections and their Implementation	23
2.6.1	Electroweak Radiative Corrections	25
2.6.2	QED Radiative Corrections	28
2.6.3	Monte Carlo Simulation of τ Production and Decay including Radiative Corrections with KORALZ	29
2.6.4	Monte Carlo Technique	30
2.6.5	Implementation of QED Radiative Corrections in a Semi-analytical Way	30
2.6.6	Monte Carlo Checks of Fitting Methods	36
3	Experimental Setup	40
3.1	The LEP Collider	40
3.2	The ALEPH Experiment	41
3.2.1	General Features of a LEP Experiment	41
3.2.2	Overview of the ALEPH Detector	41
3.2.3	Inner Tracking Chamber (ITC)	43
3.2.4	Time Projection Chamber (TPC)	44
3.2.5	Electromagnetic Calorimeter (ECAL)	50
3.2.6	Magnet and Superconducting Coil	51
3.2.7	Hadronic Calorimeter (HCAL) and Muon Chambers	51
3.2.8	Luminosity Monitors	54
3.2.9	Trigger System	55
3.2.10	Data Acquisition and Reconstruction	56

4	Data Selection	58
4.1	Selection of $\tau \rightarrow \mu\nu\nu$ Events	59
4.1.1	Monte Carlo Simulation	59
4.1.2	Definition of a Good Track	60
4.1.3	Muon Identification	60
4.1.4	Cuts at the Event Level	64
4.1.5	Cuts at the Single-Track Level	67
4.1.6	Acceptance	68
4.1.7	Efficiency of Muon Identification	71
4.1.8	Requirements on Detector Quality	76
4.1.9	Trigger Efficiency	76
4.2	Background to the Process $\tau \rightarrow \mu\nu\nu$	77
4.2.1	$\tau^\pm \rightarrow \text{Hadron}^\pm, \text{Neutrino}$ and any Number of Neutral Pions	77
4.2.2	Muon Pair Background	81
4.2.3	Two-Photon Processes	85
4.2.4	Hadronic Z^0 Decays	85
4.2.5	Cosmic Rays	85
4.2.6	Electron in the Final State Misidentified as Muon	85
4.3	Final Distributions, Branching Ratio and Luminosity	86
4.3.1	Final Two-dimensional Distribution in Momentum and Angle	86
4.3.2	Determination of Branching Ratio as a Cross Check	88
4.3.3	Total Luminosity Used	89
5	Results and Conclusions	90
5.1	Fit Procedure and Treatment of Efficiency, Resolution and Background	90
5.2	Systematic Studies	91
5.2.1	Experimental Uncertainties	91
5.2.2	Variations due to Input Parameters	94
5.2.3	Systematic Uncertainty of Fitting Method	94
5.3	Results	94
5.3.1	Determination of $\bar{g}_{\nu_\tau}/\bar{g}_{\alpha_\tau}$	94
5.3.2	Determination of $\bar{g}_{\nu_e}/\bar{g}_{\alpha_e}$ and $\bar{g}_{\nu_\tau}/\bar{g}_{\alpha_\tau}$	95
5.3.3	Determination of $\bar{g}_{\nu_{\text{lepton}}}/\bar{g}_{\alpha_{\text{lepton}}}$	95
5.3.4	Determination of $\bar{g}_{\nu_\tau}/\bar{g}_{\alpha_\tau}$ and ξ	96
5.4	Comparison with the Theoretical Predictions	98
5.5	Comparison with Other Measurements	100
5.6	Conclusions	103
A	Further Equations, Formulas and Checks	104
A.1	Lorentz Transformation	104
A.2	Validity of Approximations for the Analytical Calculations	105
A.3	Formulas for Radiative Corrections	107
B	Miscellaneous	110
B.1	Definition of CLASS 15	110
B.2	Electron Identification	110

C Alignment of ITC and TPC	112
C.1 Parameters and Basic Equations	112
C.2 Imperfections of the TPC	114
C.3 Strategy	116
C.4 Simulation	116
C.5 Reconstruction	116
C.5.1 ITC Reconstruction	116
C.5.2 TPC Reconstruction	119
C.5.3 Cuts	119
C.6 Results on Monte Carlo	119
C.6.1 Determination of Alignment Constants	119
C.6.2 Measuring Imperfections	123
C.6.3 Systematic Effects	123
C.7 Results on Data	124
C.7.1 Alignment 1989	124
C.7.2 Alignment 1991	125
C.8 Conclusions	125
 Bibliography	 126
List of Figures	130
List of Tables	132
Danksagung	133
Lebenslauf	135

1. Introduction and Summary

Historical Overview

The first observation of a weak interaction process was the discovery of β decay in 1896 by Becquerel [1]. In 1933 and 1934 a four-fermion contact interaction was described by Fermi [2] which explained the observations of the weak processes known at that time. The strength of this interaction was described by the Fermi coupling constant G_F which is measured today to $1.16637(2) \times 10^{-5} \text{ GeV}^{-2}$ [3]. The result of the ^{60}Co experiment by Wu in 1957 [4] proved that the parity is not conserved in weak interaction which led to a modification of the four-fermion contact interaction of Fermi. However, this model was not satisfactory from the theoretical point of view: Going to higher and higher energies one was in principle able to violate the unitary boundaries. This nonrenormalizability manifests itself in the fact that the strength of the coupling G_F is not dimensionless as it is for the theory of electromagnetic interaction. This problem led to the idea that the weak interaction is mediated by a vectorboson W (as the photon for the electromagnetic interaction); the short range of the weak interaction was explained by a rather large mass of this intermediate vectorboson. The Fermi theory is then just the low energy limit of the two-point coupling of two currents.

In 1961 a consistent formulation of the unification of weak and electromagnetic interaction was given by Glashow [5]. The corresponding prediction of a neutral current was confirmed by the heavy-liquid bubble chamber Gargamelle at CERN in 1973 [6] with the discovery of the process $\bar{\nu}_\mu + e \rightarrow \bar{\nu}_\mu + e$. This neutral current is mediated by a neutral massive vectorboson Z^0 . Still, the theory of massive intermediate vectorbosons is only shifting the problem of renormalizability to higher energies. As a matter of fact, a theory with massive vectorbosons cannot be renormalized. The final formulation of the unification of electromagnetic and weak interaction in the framework of $SU(2)_{\text{weak Isospin}} \times U(1)_{\text{weak Hypercharge}}$ by Glashow, Weinberg and Salam in 1967/68 [5] uses therefore only massless particles (leptons, quarks and vectorbosons). The theory is a so-called "Gauge Theory". It is based on the requirement of invariance under local gauge transformations. The final masses of the particles are obtained by a formalism described by Higgs [7] and Kibble [8]. This "spontaneous symmetry breaking" (called the Higgs mechanism) breaks the symmetry of the ground state without changing the symmetry of the equations of the theory itself. As a consequence a new particle—the Higgs particle—was predicted. The renormalizability of the theory was proved by 'tHooft [9] in 1971 leading to a consistent field theory describing the electromagnetic and weak interaction as unified electroweak interaction.

The three new bosons were discovered by the experiments UA1 and UA2 [10, 11] at the $\bar{p}p$ collider SPS at CERN in 1983. The mass of the W^\pm bosons has been measured recently by CDF [12] to $(79.83 \pm 0.44) \text{ GeV}$, the ratio $\frac{M_W}{M_Z}$ by CDF and UA2 [13] to (0.8831 ± 0.0055) . The MARK-II collaboration [14] at the Stanford Linear Collider at SLAC has observed 106 Z^0 decays in 1989. The CERN Large Electron-Positron Collider

LEP has produced nearly a million Z^0 in 1989 and 1990 collected at the four experiments ALEPH, DELPHI, L3 and OPAL. The combined measurements in 1989 and 1990 lead to a mass $M_Z = (91.177 \pm 0.021) GeV$ and a total width $\Gamma_Z = (2.496 \pm 0.014) GeV$ [15].

The Standard Model

The Standard Model of the electroweak interaction is characterized by several parameters. Not counting the fermion masses, the Higgs mass and the fermion mixings three parameters cannot be predicted by the theory. The most natural choice of these three parameters is M_W , M_Z and α_0 . Nevertheless, as these parameters must be determined by experiment, it is more sensible to choose a set of parameters in which they are measured very precisely. Usually this set consists of the fine structure constant $\alpha_0 = 1/137.035990(6)$ [3] (measured by the magnetic moment anomaly $g - 2$ of the electron), the Fermi coupling constant $G_F = 1.16637(2) \times 10^{-5} GeV^{-2}$ [3] (measured by the muon decay rate) and the mass of the Z^0 (M_Z) or the sine of the Weinberg angle $\sin^2\theta_W$ (measured by the ratio of charged/neutral current in neutrino experiments or by Z^0 production). The latter describes the mixing of the neutral vectorbosons of the pure $U(1)$ and of the pure $SU(2)$. One state is identified with the massless photon. The orthogonal neutral state is called the neutral vectorboson Z^0 . The remaining charged doublet in $SU(2)$ is assigned to the two intermediate charged vectorbosons W^+ and W^- mediating the charged current in weak interaction.

Using α_0 , G_F and M_Z as parameter set, $\sin^2\theta_W$ is fixed by these three parameters. In the so-called *on shell* renormalization scheme $\sin^2\theta_W$ is determined by the ratio of M_W/M_Z , where M_W can be expressed in terms of the other parameters. As α_0 and G_F are determined rather accurately, precise measurements of $\sin^2\theta_W$, M_W and M_Z as given above provide a good test for the Standard Model.

The top quark and the Higgs particle are still subject of extensive searches by several experiments. The best direct lower limit for the Higgs mass given by ALEPH is $48 GeV$ with 95 % C.L. [16]. CDF [17] has set the best direct lower limit of $89 GeV$ for the top mass with 95 % C.L.

At the precision level which is achieved by experiments nowadays electroweak radiative corrections become very important. These consist of higher order contributions in perturbation theory, which is used for calculating physical processes. One very important parameter in this context is Δr which takes the radiative corrections into account for the connection of the low energy parameter G_F and the high energy parameter M_W . The interesting property of this quantity is the fact that it depends on the top and the Higgs mass via fermion loop corrections. Interpreting the ALEPH results in this context they are consistent with a top mass of $M_{top} = (172^{+44}_{-58}) GeV$ assuming a Higgs mass below $1000 GeV$ [18]. This result is consistent with the direct lower limit of CDF given above.

The predictions for the Lorentz structure of the charged current (described by the parameters ρ , ξ , δ and η [3]) and the couplings g_v and g_a of the Z^0 to the fermions (neutral current) provide another crucial check of the Standard Model. For the charged current "V-A" structure is predicted while the neutral current couplings depend on the actual value of $\sin^2\theta_W$.

Up to now, no deviations from the Standard Model have been found.

The τ Lepton

The τ lepton has been discovered at the e^+e^- collider SPEAR in 1975 [19]. The fermionic character and the introduction of a new conserved lepton number were established at SPEAR and DORIS (for a review see [20]). The τ lepton and its neutrino is the third family of leptons besides the electron and the muon family. So far no deviations from the lepton universality hypothesis have been found comparing the τ with the other leptons. The mass of the τ is measured to $m_\tau = 1784.2_{-3.6}^{+2.7} \text{ MeV}$ [3]. This rather large mass allows the τ to decay into hadrons (e.g. π or ρ) which is not possible for the lighter leptons. The main source of τ 's are e^+e^- colliders which allow detailed studies. Due to the rather short lifetime of the τ of $(3.03 \pm 0.08) \cdot 10^{-13} \text{ s}$ [3] only the decay products can be detected. This has the advantage that the decay products can be used as "spin analysers" for the helicity of the τ 's. This allows stringent tests of the Standard Model which gives precise predictions for the polarization of the τ 's produced by photons or Z^0 's.

Only one of the parameters describing the structure of the charged current in leptonic τ decays is measured up to now [21]. The knowledge of this parameter ρ is not enough to prove "V-A" structure. It is therefore very important to get determinations of other parameters as well.

Measurements with the Process $e^+e^- \rightarrow Z^0 \rightarrow \tau^+\tau^-; \tau \rightarrow \mu\nu\nu$

After the overview given in the last three sections the topics and the summary of this thesis are given below.

The production of τ 's via the process $e^+e^- \rightarrow Z^0 \rightarrow \tau^+\tau^-$ and the subsequent decay $\tau \rightarrow \mu\nu\nu$ are investigated. The aim is to determine on one hand the properties of the *neutral current* including the τ polarization. On the other hand there are several parameters describing the structure of the *charged current* in the leptonic decay $\tau \rightarrow \mu\nu\nu$. Only one of them (ρ) has been determined up to now [21]. The second topic of this thesis covers the study of possibilities for measuring the remaining parameters and an actual measurement of one of them (ξ).

For this purposes the complete data set taken in 1989 and 1990 at ALEPH has been processed. The muons from τ decays are selected. Altogether a total luminosity of about 8 pb^{-1} at eleven center-of-mass energies between 88 and 95 GeV is used.

The ALEPH collaboration has published recently a determination of the τ polarization [22]. This measurement includes the decay channels $e\nu\nu$, $\mu\nu\nu$, $\pi\nu$, $\rho\nu$ and $a_1\nu$ and results in $P_{\tau^-} = (-14.3 \pm 4.5)\%$. The results of this thesis are contained in this publication for the muon channel.

Summary of this Thesis

A detailed description of the method to measure the ratios of the couplings of the Z^0 to the τ and the electron $\bar{g}_{\nu_\tau}/\bar{g}_{\alpha_\tau}$, $\bar{g}_{\nu_e}/\bar{g}_{\alpha_e}$ and the τ decay parameters is given. For this purpose for the first time the two-dimensional momentum and angular distribution of the muons from $\tau \rightarrow \mu\nu\nu$ decays is used. This is accompanied with a detailed description of the underlying physical processes and radiative corrections. Monte Carlo samples are used to check the performance of this method. After a description of the ALEPH detector with its main components the selection of the events is explained and sources of systematic

errors are described. The selection finds 1509 candidates which are used to perform a fit extracting four different sets of parameters. The corresponding results are (the bar on the couplings denotes the effective couplings taking electroweak radiative corrections into account):

- (1) The measurement of the τ polarization of

$$P_{\tau^-} = (-20 \pm 12_{stat} \pm 6_{syst}) \% \text{ or } \frac{\bar{g}_{\tau\tau}(s=M_Z^2)}{\bar{g}_{\alpha\tau}(s=M_Z^2)} = 0.101 \pm 0.064_{stat} \pm 0.031_{syst}$$

from the momentum spectrum only.

- (2) The simultaneous determination of

$$\frac{\bar{g}_{\tau\tau}(s=M_Z^2)}{\bar{g}_{\alpha\tau}(s=M_Z^2)} = 0.109 \pm 0.059_{stat} \pm 0.018_{syst} \text{ and}$$

$$\frac{\bar{g}_{\tau\tau}(s=M_Z^2)}{\bar{g}_{\alpha\tau}(s=M_Z^2)} = 0.119 \pm 0.057_{stat} \pm 0.028_{syst}.$$

- (3) The measurement of

$$\frac{\bar{g}_{\alpha_{lepton}}(s=M_Z^2)}{\bar{g}_{\alpha_{lepton}}(s=M_Z^2)} = 0.113 \pm 0.031_{stat} \pm 0.016_{syst} \text{ assuming lepton universality.}$$

- (4) The simultaneous determination of the τ decay parameter

$$\xi = 0.72^{+0.52}_{-0.34_{stat}} \pm 0.30_{U_{ncert. on \bar{g}_{\tau\tau}, \rho}} \pm 0.18_{syst} \text{ and}$$

$$\frac{\bar{g}_{\tau\tau}(s=M_Z^2)}{\bar{g}_{\alpha\tau}(s=M_Z^2)} = 0.202 \pm 0.071_{stat} \pm 0.013_{syst}^{+0.154}_{-0.056_{U_{ncert. on \bar{g}_{\tau\tau}, \rho}}}$$

using the constraint from the forward-backward asymmetry measurement in the τ channel [23], previous measurements of ρ [21] and assuming $\delta = 3/4$.

Result (1) is given for comparison with other measurements of the τ polarization. The precision of the ratio of the couplings of the τ (result 2) using the two-dimensional momentum and angular distribution is roughly one order of magnitude better than previous measurements [24] and shows no deviation from lepton universality. The measurement of the couplings assuming lepton universality results in a value for \bar{g}_v which is nonzero by more than three standard deviations (result 3). The resulting effective sine of the Weinberg angle is given by

$$\overline{\sin^2\theta_W}(s = M_Z^2) = 0.2211 \pm 0.0087. \quad (1.1)$$

in agreement with previous measurements.

For the first time the τ decay parameter ξ has been determined (result 4). The corresponding assumption of $\delta = 3/4$ (which is needed only due to the lack of statistics) still allows one to decide whether “V-A” ($\xi = 1$, $\rho = 3/4$, $\delta = 3/4$) or “V+A” ($\xi = -1$, $\rho = 3/4$, $\delta = 3/4$) at both (τ and μ) vertices of the W in $\tau \rightarrow \mu\nu\nu$ decays is realized in nature: The “V+A” alternative is excluded by more than 3.5σ .

All measurements are thus in agreement with the Standard Model.

A method to align the two tracking detectors Inner Tracking Chamber (ITC) and Time Projection Chamber (TPC) to the precision of $\approx 50 \mu\text{m}$ leading to a momentum resolution of $\frac{\Delta p}{p} = 0.8 \times 10^{-3} (\text{GeV}/c)^{-1}$ is described in the appendix. This procedure uses cosmic rays which are taken in a dedicated run of the ALEPH detector. Besides the geometrical alignment this method results in a measurement of the relative transverse drift velocities in the TPC with a precision at the level of 10^{-5} .

2. τ Production and Decay

In this chapter an overview of the relevant part of the Standard Model is given. It starts with the calculation of the production of τ 's at the Z^0 resonance. This calculation is done taking the helicity state of the outgoing particles into account. From these equations some commonly used observables (asymmetries) are derived to be compatible with other publications. Nevertheless, in this thesis the physics and the measurements are discussed mainly in terms of the neutral current coupling constants. The τ decay and the various decay channels are described with special emphasis on the possibility to measure the mean τ polarization. Specializing on the $\tau \rightarrow \mu\nu\nu$ channel the production and decay parameters and the possibilities of their measurement are discussed. The largest part deals with the treatment of radiative corrections and their implementation. Finally extensive Monte Carlo studies are presented exploiting all possible measurements.

2.1 Production of $\tau^+\tau^-$ in e^+e^- -Annihilation

To understand the fundamental physics in e^+e^- -annihilations into Z^0 all processes are considered on the tree level. The vertex in Born approximation of a Z^0 going into fermion-antifermion pair is shown in figure 2.1, and given by

$$i \frac{e}{2\cos\theta_W \sin\theta_W} \gamma_\mu (g_{\nu_f} - g_{a_f} \gamma_5). \quad (2.1)$$

In this Ansatz only axial (g_{a_f}) and vector currents (g_{ν_f}) are taken into account. The Standard Model gives a precise prediction for g_{ν_f} and g_{a_f} , describing the neutral current:

$$g_{\nu_f} = I_3^f - 2Q_f \sin^2\theta_W,$$

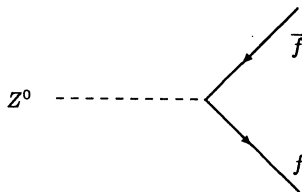


Figure 2.1: Vertex of Z^0 going into fermion-antifermion.

$$\begin{aligned}
g_{a_f} &= I_3^f, \\
\frac{g_{v_f}}{g_{a_f}} &= 1 - 2\frac{Q_f}{I_3^f}\sin^2\theta_W,
\end{aligned}
\tag{2.2}$$

where I_3^f is the third component of the weak Isospin and Q_f the charge of the fermion f . The Weinberg angle θ_W describes the mixing between pure U(1) and pure SU(2) in the Standard Model. Grouping the three different species of leptons (e , μ and τ) together with their neutrinos according to their helicity¹ one gets three singlets and three doublets:

$$\begin{aligned}
I^f &= 0 & (e)_R & & (\mu)_R & & (\tau)_R \\
I^f &= 1/2 & \begin{pmatrix} \nu_e \\ e \end{pmatrix}_L & & \begin{pmatrix} \nu_\mu \\ \mu \end{pmatrix}_L & & \begin{pmatrix} \nu_\tau \\ \tau \end{pmatrix}_L.
\end{aligned}$$

One consequence of the Standard Model is that only the left-handed doublets couple to the Z^0 . The value of $\sin^2\theta_W = 0.2259 \pm 0.0046$ given in [3] yields $g_{v_f}/g_{a_f} = 0.080$ as expected value for the Standard Model. Any value differing from this expectation would give a hint to problems in the understanding of the electroweak theory.

To get the differential cross-section for the process $e^+e^- \rightarrow \tau^+\tau^-$ for unpolarized electrons and positrons the two vertices are combined with the propagator of the Z^0 and the photon. The same expression is valid for $e^+e^- \rightarrow \mu^+\mu^-$ whereas the treatment of the electron-channel in the final state is more sophisticated because of the t-channel exchange. At the tree level the result is [25]

$$\begin{aligned}
\frac{d\sigma^{\text{Born}}}{d\cos\theta}(p; s, \cos\theta) &= \left[(1 + \cos^2\theta)F_0(s) + 2\cos\theta F_1(s) \right] - \\
&\left[(1 + \cos^2\theta)F_2(s) + 2\cos\theta F_3(s) \right] p,
\end{aligned}
\tag{2.3}$$

where θ is the angle of the outgoing τ^- relative to the incoming e^- , s the center-of-mass energy squared ($s = 4E_{\text{Beam}}^2$) and p the helicity state of the τ^- (or μ^- for $\mu^+\mu^-$ final state). As the Z^0 has spin 1 the corresponding helicity of the τ^+ is $-p$ because of angular momentum conservation. The F_i are given by

¹The subscript 'R' refers to right-handed, 'L' to left-handed particles

$$\begin{aligned}
F_0(s) &= \frac{G_F^2 M_Z^4 \rho_0^2}{32 \pi s} |\chi(s)|^2 (g_{\nu_e}^2 + g_{a_e}^2)(g_{\nu_\tau}^2 + g_{a_\tau}^2) + \frac{\sqrt{2} G_F M_Z^2 \rho_0}{16 s} 2 \operatorname{Re}\{\alpha^* \chi(s)\} q_e q_\tau g_{\nu_e} g_{\nu_\tau} \\
&\quad + \frac{\pi |\alpha|^2}{4 s} q_e^2 q_\tau^2 \\
F_1(s) &= \frac{G_F^2 M_Z^4 \rho_0^2}{32 \pi s} |\chi(s)|^2 2 g_{\nu_e} g_{a_e} 2 g_{\nu_\tau} g_{a_\tau} + \frac{\sqrt{2} G_F M_Z^2 \rho_0}{16 s} 2 \operatorname{Re}\{\alpha^* \chi(s)\} q_e q_\tau g_{a_e} g_{a_\tau} \\
F_2(s) &= \frac{G_F^2 M_Z^4 \rho_0^2}{32 \pi s} |\chi(s)|^2 (g_{\nu_e}^2 + g_{a_e}^2) 2 g_{\nu_\tau} g_{a_\tau} + \frac{\sqrt{2} G_F M_Z^2 \rho_0}{16 s} 2 \operatorname{Re}\{\alpha^* \chi(s)\} q_e q_\tau g_{\nu_e} g_{a_\tau} \\
F_3(s) &= \frac{G_F^2 M_Z^4 \rho_0^2}{32 \pi s} |\chi(s)|^2 2 g_{\nu_e} g_{a_e} (g_{\nu_\tau}^2 + g_{a_\tau}^2) + \frac{\sqrt{2} G_F M_Z^2 \rho_0}{16 s} 2 \operatorname{Re}\{\alpha^* \chi(s)\} q_e q_\tau g_{a_e} g_{\nu_\tau},
\end{aligned} \tag{2.4}$$

$$\chi(s) = \frac{s}{s - M_Z^2 + i s \Gamma_Z / M_Z}. \tag{2.5}$$

Two different coupling strengths are used: α and $\sqrt{2} G_F M_Z^2$. The latter one originates historically from the four-point Fermi interaction used to describe the muon decay. The relation between this coupling constant and α is given in the Standard Model:

$$\frac{4\pi\alpha}{4s \sin^2 \theta_W \cos^2 \theta_W} = \sqrt{2} G_F M_Z^2 \rho_0, \tag{2.6}$$

where ρ_0 describes the Higgs sector of the Standard Model; a Higgs doublet implies $\rho_0 = 1$. As it will be very useful for the treatment of radiative corrections to 'mark' the couplings of the photon and the Z^0 by different constants, α and $\sqrt{2} G_F M_Z^2$ are kept separately. For the same reason, α is used as a complex number (α^* is the complex conjugate). The imaginary part of the propagator takes the finite width of the Z^0 into account (Improved Born Approximation).

To look at the dependence of the total cross-section on s , equation (2.3) must be integrated over $\cos\theta$ and summed over the two helicity states of the outgoing τ^- . This leads to

$$\sigma^{Born}(s) = \frac{16}{3} F_0(s), \tag{2.7}$$

which is plotted in figure 2.2 where the Standard Model values for the couplings are assumed. At low energies the cross-section is dominated by photon exchange which decreases like $1/s$. At energies around M_Z the cross-section is dominated by Z^0 exchange.

At the peak, equations (2.4) can be simplified. Here, $\operatorname{Re}\{\alpha^* \chi(s)\} = 0$ (only true for real α , which means no radiative corrections) and one can neglect the pure photon exchange term $q_e q_\tau$. The F_i become

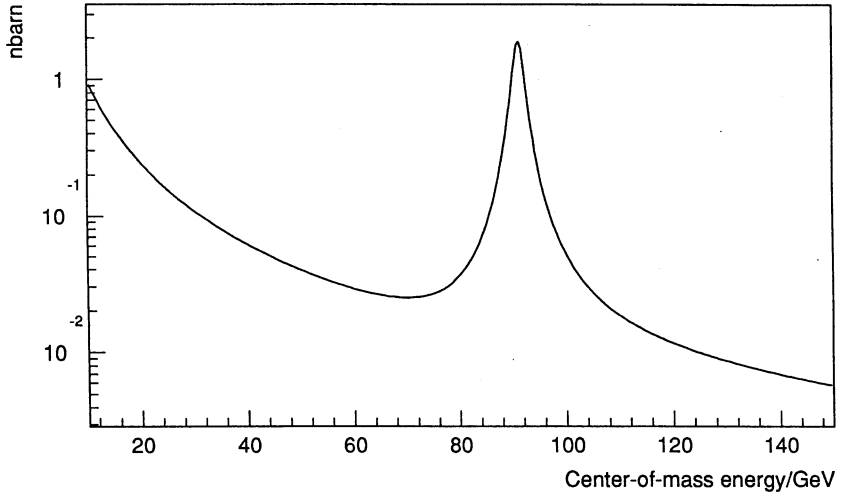


Figure 2.2: Total Born cross-section versus s .

$$\begin{aligned}
 F_0(s = M_Z^2) &= \frac{G_F^2 M_Z^4 \rho_0^2}{32 \pi \Gamma_Z^2} (g_{\nu_e}^2 + g_{a_e}^2)(g_{\nu_\tau}^2 + g_{a_\tau}^2), \\
 \frac{F_1(s = M_Z^2)}{F_0(s = M_Z^2)} &= A_e A_\tau, \\
 \frac{F_2(s = M_Z^2)}{F_0(s = M_Z^2)} &= A_\tau, \\
 \frac{F_3(s = M_Z^2)}{F_0(s = M_Z^2)} &= A_e, \\
 \text{with } A_j &= \frac{2g_{\nu_j} g_{a_j}}{g_{\nu_j}^2 + g_{a_j}^2}. \tag{2.8}
 \end{aligned}$$

A_i is predicted to be $2(1 - 4\sin^2\theta_W) \approx 16\%$ by the Standard Model according to equation (2.2).

2.2 Asymmetries A_{FB} , A_{pol} and A_{pol}^{FB}

In this section the commonly used observables A_{FB} , A_{pol} and A_{pol}^{FB} are described. This is done to allow a comparison of measurements in this thesis with direct measurements of these asymmetries elsewhere. The main emphasis in this thesis is the use of equation (2.3) for extracting A_e and A_τ rather than the various asymmetries.

The expressions for F_i at the Z^0 peak given in equation (2.8) show the different possibilities for extracting information from the production equation (2.3). F_0 , which determines the total cross-section (see equation 2.7), serves as normalization, so that only the ratios $\frac{F_i}{F_0}$ are considered as given in equation (2.8). Determining F_2 or F_3 gives a measurement linear in A_r or A_e , respectively. Therefore they provide a higher sensitivity than F_1 , which is the product of the two rather small quantities A_r and A_e . The ratios $\frac{F_i}{F_0}$ are usually discussed in terms of three asymmetries. They are

- (i) the forward-backward asymmetry A_{FB} ,
- (ii) the polarization asymmetry A_{pol} and
- (iii) the forward-backward polarization asymmetry A_{pol}^{FB} ,

which will now be defined

The *forward-backward asymmetry* A_{FB} is defined as the number of τ^- which are produced in the forward direction ($\cos\theta > 0$) minus the number produced in the backward direction ($\cos\theta < 0$) normalized by the sum of the two quantities:

$$\begin{aligned}
 A_{FB} &\equiv \frac{N_{\cos\theta > 0} - N_{\cos\theta < 0}}{N_{\cos\theta > 0} + N_{\cos\theta < 0}} \\
 &= \frac{1}{\sigma_0} [\sigma(\cos\theta > 0) - \sigma(\cos\theta < 0)] = \frac{3}{4} \frac{F_1(s)}{F_0(s)} \\
 &\stackrel{(*=M_Z^2)}{=} \frac{3}{4} A_e A_r.
 \end{aligned} \tag{2.9}$$

Usually the whole $\cos\theta$ range is not covered by the detector. If the range is restricted to $[-|\cos\theta|, +|\cos\theta|]$ rather than $[-1, 1]$, the formula becomes

$$A_{FB}(\cos\theta) = \frac{3|\cos\theta|}{3 + \cos^2\theta} \frac{F_1(s)}{F_0(s)}, \tag{2.10}$$

which means that the sensitivity with respect to $\frac{F_1(s)}{F_0(s)}$ gets smaller.

The *polarization asymmetry* A_{pol} is defined as the number of τ^- with positive helicity minus the number of τ^- with negative helicity normalized by the sum of the two:

$$\begin{aligned}
 A_{pol} &\equiv \frac{N_{p=+1} - N_{p=-1}}{N_{p=+1} + N_{p=-1}} \\
 &= \frac{1}{\sigma_0} [\sigma(p = +1) - \sigma(p = -1)] = -\frac{F_2(s)}{F_0(s)} \\
 &\stackrel{(*=M_Z^2)}{=} -A_r.
 \end{aligned} \tag{2.11}$$

Hence, A_{pol} gives a handle to measure the ratio g_{ν_r}/g_{a_r} via A_r . Furthermore it is more sensitive to A_r compared to the forward-backward asymmetry because it depends

linearly on it. It should be stressed that equation (2.11) is still valid if the $\cos\theta$ range is limited due to the detector, as long as the angular range is symmetrical around $\cos\theta = 0$ (typically $|\cos\theta| < 0.95$). On the other hand, A_{pol} can be looked at differentially without integrating over $\cos\theta$:

$$A_{pol}(\cos\theta) = \frac{\frac{F_2(s)}{F_0(s)} + \frac{2\cos\theta}{1+\cos^2\theta} \frac{F_3(s)}{F_0(s)}}{1 + \frac{2\cos\theta}{1+\cos^2\theta} \frac{F_1(s)}{F_0(s)}} \underset{(s=M_Z^2)}{=} \frac{A_r + \frac{2\cos\theta}{1+\cos^2\theta} A_e}{1 + \frac{2\cos\theta}{1+\cos^2\theta} A_r A_e} \quad (2.12)$$

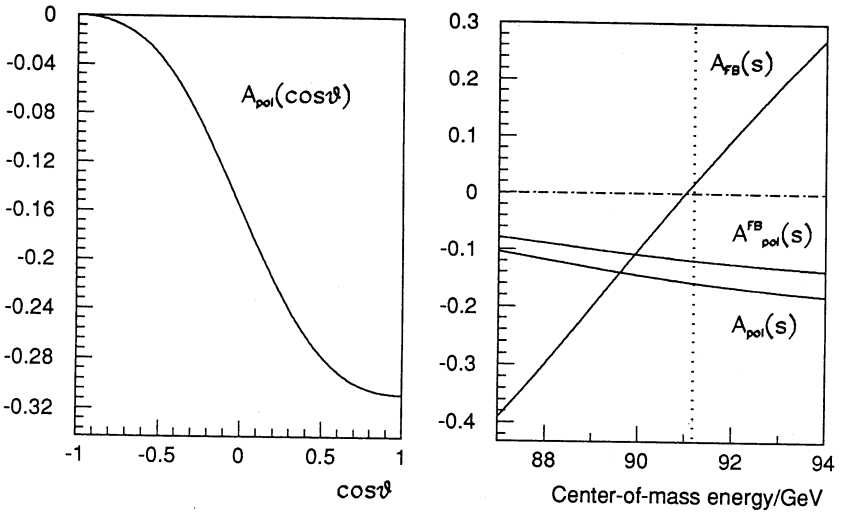


Figure 2.3: A_{pol} as a function of $\cos\theta$ (left) and A_{pol} , A_{FB} and A_{pol}^{FB} as function of the center-of-mass energy (right).

Figure 2.3 (left) shows the variation of A_{pol} with $\cos\theta$. The strength of this variation is determined by A_e , which leads to the next observable.

The *forward-backward polarization asymmetry* A_{pol}^{FB} is defined as the polarization asymmetry measured in the forward direction ($\cos\theta > 0$) minus the one measured in the backward direction ($\cos\theta < 0$) normalized by the sum of the two:

$$\begin{aligned}
A_{pol}^{FB} &\equiv \frac{[N_{\cos\theta > 0, p=+1} - N_{\cos\theta > 0, p=-1}] - [N_{\cos\theta < 0, p=+1} - N_{\cos\theta < 0, p=-1}]}{[N_{\cos\theta > 0, p=+1} + N_{\cos\theta > 0, p=-1}] + [N_{\cos\theta < 0, p=+1} + N_{\cos\theta < 0, p=-1}]} \\
&= \frac{1}{\sigma_0} [\sigma(\cos\theta > 0, p = +1) - \sigma(\cos\theta > 0, p = -1) \\
&\quad - \{\sigma(\cos\theta < 0, p = +1) - \sigma(\cos\theta < 0, p = -1)\}] \\
&= -\frac{3}{4} \frac{F_3(s)}{F_0(s)} \\
&\stackrel{(s=M_Z^2)}{=} -\frac{3}{4} A_e.
\end{aligned} \tag{2.13}$$

A_{pol}^{FB} measures linearly the vector coupling A_e of the initial electron. The sensitivity to this coupling is therefore substantially higher than the one of A_{FB} . A plot of the behaviour of A_{pol} , A_{FB} and A_{pol}^{FB} as a function of the center-of-mass energy is given in figure 2.3(right).

The three variables A_{FB} , A_{pol} and A_{pol}^{FB} are obtained by a different form of integration over $\cos\theta$ or summation over p with respect to equation (2.3) and demonstrate what kind of information about A_e and A_τ can be extracted from the data. Nevertheless they cannot give conceptually better information on A_e and A_τ than a fit to this equation. Before considering this possibility of using the complete formula, other methods to measure the couplings g_v and g_a at the Z^0 pole are briefly discussed.

2.3 Determination of Couplings from Γ_{ll} and A_{FB}

The total width of the Z^0 is given by the sum of all partial widths into all possible final states:

$$\Gamma_Z = \Gamma_{had} + \Gamma_{ee} + \Gamma_{\mu\mu} + \Gamma_{\tau\tau} + \Gamma_{inv}. \tag{2.14}$$

They correspond to the final states $q\bar{q}$, e^+e^- , $\mu^+\mu^-$, $\tau^+\tau^-$ and $\nu\bar{\nu}$. The leptonic widths depend on the actual couplings to the Z^0 by the relation [26]

$$\Gamma_{ff} = \frac{G_F M_Z^3}{6\pi\sqrt{2}} (g_{v_f}^2 + g_{a_f}^2). \tag{2.15}$$

Together with the asymmetries given in section 2.2 a measurement of g_v and g_a is possible. It is ambiguous only to a common sign due to the quadratic dependence in equation (2.15). This has been done by ALEPH [18] using the forward-backward asymmetry for all channels. The result is

$$\begin{aligned}
g_{v_{lepton}} &= -0.039 \pm 0.008 \\
g_{a_{lepton}} &= -0.498 \pm 0.002.
\end{aligned}$$

τ^- decay channel		Branching Ratio (%)
topological	exclusive	
one charged particle	$\mu^- \nu \nu$	86.1 ± 0.3
	$e^- \nu \nu$	17.8 ± 0.4
	$\pi^- \nu$	17.7 ± 0.4
	$K^- \geq 0 \text{ neutrals } \nu$	11.0 ± 0.5
	$\rho^- \nu$	1.7 ± 0.2
	$\pi^- \pi^0 \nu$ non-resonant	22.7 ± 0.8
	$hadron^- \geq 2 hadron^0 \nu$	$0.37^{+0.30}_{-0.22}$
		14.7 ± 0.8
three charged particles	$\pi^- \pi^- \pi^+ \nu$	13.8 ± 0.3
	$\pi^- \pi^- \pi^+ \geq 1 \gamma \nu$	7.1 ± 0.6
	$K^- \pi^+ \pi^- \geq 0 \pi^0 \nu$	6.7 ± 0.7
	$K^- K^+ \pi^- \nu$	$0.22^{+0.16}_{-0.13}$
		$0.22^{+0.17}_{-0.11}$
five charged particles		$(11 \pm 3) \times 10^{-2}$
	$3\pi^- 2\pi^+ \nu$	$(5.6 \pm 1.6) \times 10^{-2}$
	$3\pi^- 2\pi^+ \pi^0 \nu$	$(5.1 \pm 2.2) \times 10^{-2}$

Table 2.1: τ^- decay channels (topological and exclusive).

The ambiguity of the sign has been solved by the τ polarization measurement of ALEPH [22] and electron-neutrino scattering experiments [27, 28, 29]. While g_{alephon} is measured essentially by Γ_{ll} , $g_{\nu\text{lepton}}$ is determined by the forward-backward asymmetries.

2.4 τ Decay

The τ lifetime is $(3.03 \pm 0.08) \cdot 10^{-13}$ s [3]. Thus a τ with an energy of $M_Z/2$ decays within a couple of millimeters. Therefore only the directions and the momenta of the decay products are available. The information about the helicity of the τ can then be extracted from those quantities as it has been done for the muon [30]. The different known decay channels are given in table 2.1 [3].

Looking at this table the final states $\pi^- \nu$, $\rho^- \nu$, $hadron^- \pi^+ \pi^- \nu$ (via the resonance a_1), $\mu^- \nu \nu$ and $e^- \nu \nu$ can be used for measurements of the helicity state of the τ because their branching ratios are reasonably large.

The energy/angle distribution of the decay product for final states with only one charged particle in the center-of-mass system of the decaying τ can be written as

$$\frac{d\sigma}{dx^* d\cos\theta^*} = K(f_1(x^*) + \cos\theta^* f_2(x^*)). \quad (2.16)$$

K is some constant, x^* the ratio $E_{\text{particle}}^{cms}/E_{\text{particle}}^{\text{max},cms}$ and $\cos\theta^*$ the angle of the charged particle with respect to the τ spin. f_1 and f_2 are functions which depend on the particular properties of the decay particles (spin and mass). To get this equation, no assumption

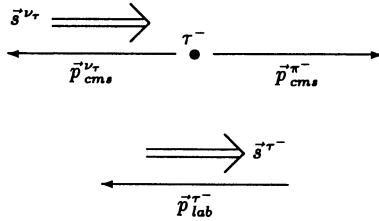


Figure 2.4: $\tau^- \rightarrow \pi^- \nu$ in the τ rest frame.

about the Lorentz structure of the weak charged currents is needed. Nevertheless, for the actual equations in the next sections, “V-A” is assumed for the charged current, which will be dropped later on. Finally equation (2.16) has to be transformed into the laboratory frame. The specific results are shown in the next sections.

2.4.1 $\tau^- \rightarrow \pi^- \nu$

This 2-body decay into a spin 0 (π^-) and a spin $\frac{1}{2}$ particle is shown in figure 2.4 in the center-of-mass system of the decaying τ^- . Assuming a left-handed ν_r , the π^- gets less momentum in the laboratory system for a left-handed τ^- compared to the case of a right-handed τ^- because the emission of the π^- antiparallel to the τ^- direction is preferred. Therefore the π^- has more often a lower momentum (the spectrum has a negative slope) for τ^- with negative helicity state (on average). This means that the determination of the polarization consists of a measurement of the slope of the momentum spectrum of the final pion. Using equation (2.16) with the appropriate properties of the pion in the laboratory frame, the energy distribution in the variable $x = p_{\text{particle}}/E_\tau$ is given by [25]

$$h_\tau(x; P_{r-}) = 1 + P_{r-}(2x - 1). \quad (2.17)$$

The mean polarization $P_{r-} = \langle p \rangle$ has been introduced to clearly separate it from the helicity state p of one τ^- as used in equation (2.3) and the Standard Model prediction $P_{r-} = -A_r$, introduced in equation (2.11).

2.4.2 $\tau^- \rightarrow \mu^- \nu \nu, e^- \nu \nu$

Lepton number conservation demands two ν in the final state for the leptonic τ decay channels. Therefore the three spin $\frac{1}{2}$ particles in the final state form a 3-body decay. The corresponding considerations are hence not as easy as in the 2-body-case. Nevertheless the higher end of the momentum spectrum can be explained with a simple argument. Figure 2.5 shows the situation for the highest possible muon momentum (the whole recoil momentum of the two ν is given to the muon, which goes in the direction of the τ momentum). Assuming a right-handed $\bar{\nu}_\mu$ and a left-handed ν_r the μ^- has to take the helicity of the τ^- in this final state. The “V-A” structure of the charged weak

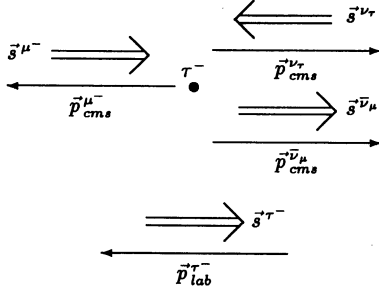


Figure 2.5: $\tau^- \rightarrow \mu^- \nu \nu$ in the τ rest frame.

current demands the μ^- to have negative helicity. Therefore the final state with maximum momentum of the μ^- is only possible for a τ^- with negative helicity. This explains why the upper end of the momentum spectrum is more populated for negative helicity of the τ^- than for positive helicity. Again, the momentum spectrum of the final state particle is used to determine the mean polarization according to the distribution

$$\begin{aligned}
 h_{\mu,e}(x; P_{\tau^-}) &= h_0^{\mu,e}(x) - P_{\tau^-} h_1^{\mu,e}(x) \\
 \text{with } h_0^{\mu,e} &= \frac{5}{3} - 3x^2 + \frac{4}{3}x^3 \\
 \text{and } h_1^{\mu,e} &= -\frac{1}{3} + 3x^2 - \frac{8}{3}x^3.
 \end{aligned} \tag{2.18}$$

These formulas are derived in section 2.5.1 and can be found also in [25]. The sensitivity for measuring the helicity of the initial state τ^- is clearly smaller than that for 2-body-case. The higher statistics of the leptonic decays compensates partially for their smaller sensitivity. The spectra for the polarizations $0, \pm 1$ can be found in figure 2.6.

2.4.3 $\tau^- \rightarrow \rho^- \nu$ and $\tau^- \rightarrow a_1 \nu$

The final states with more than one hadron are usually mediated via a resonance ($\rho^\pm \rightarrow \pi^\pm \pi^0$ or $a_1^\pm \rightarrow \rho^\pm \pi^0$) in the decay. In principle they can be treated the same way as the channels described before. This leads to a distribution in $\cos\theta^*$

$$\frac{d\sigma}{d\cos\theta^*} \propto 1 + \alpha P_{\tau^-} \cos\theta^*, \tag{2.19}$$

where $\cos\theta^*$ is the angle between the ρ/a_1 direction and the τ spin in the τ rest frame. It can be expressed by the sum of all normalized hadron energies x_i in the laboratory frame (i runs from 1 to 2 for the ρ channel and from 1 to 3 for the a_1 channel; m_h corresponds to m_ρ or m_{a_1}):

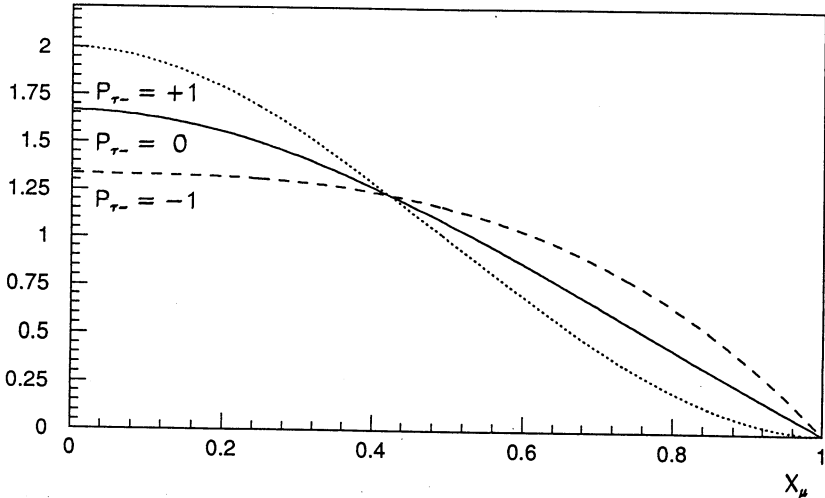


Figure 2.6: Momentum spectrum of muons from τ decays for polarizations $0, \pm 1$.

$$\cos\theta^* = \frac{2(\Sigma_i x_i) - 1 - \left(\frac{m_h}{m_r}\right)^2}{1 - \left(\frac{m_h}{m_r}\right)^2}. \quad (2.20)$$

The sensitivity α in equation (2.19) for spin 1 systems is given by the ratio

$$\alpha = \frac{1 - 2\left(\frac{m_h}{m_r}\right)^2}{1 + 2\left(\frac{m_h}{m_r}\right)^2}. \quad (2.21)$$

This sensitivity is 1 for spin 0 systems (as the pion channel). For the ρ and the a_1 channel α is 0.46 and 0.001, respectively. In other words, the ρ channel is only partially useful while the a_1 channel does not help at all. The underlying physical explanation is the spin of the decay particle: while the pion has no spin, a_1 and ρ have spin 1.

A way to substantially increase the sensitivity is to introduce two angles which take into account the two helicity amplitudes which originate in the spin 1 of the ρ and the a_1 [31]. For this purpose a second angle ψ is used. It characterizes the decay distribution into the final hadrons. With this additional angle it is possible to distinguish between the two helicity amplitudes for hadronic spin-1 systems. For the ρ channel, ψ is the ρ decay angle relative to the ρ laboratory line of flight:

$$\cos\psi_\rho = \frac{m_\rho}{\sqrt{m_\rho^2 - 4m_\pi^2}} \frac{E_{\pi^\pm} - E_{\pi^0}}{|\vec{p}_{\pi^\pm} - \vec{p}_{\pi^0}|}. \quad (2.22)$$

For the a_1 (which decays into a three pion system) the corresponding ψ is the angle between the normal to the plane of the three pions in their rest frame and the three pions' laboratory line of flight:

$$\cos\psi = \frac{8m_{a_1}^2 \vec{p}_1 \cdot (\vec{p}_2 \times \vec{p}_3) / |\vec{p}_1 + \vec{p}_2 + \vec{p}_3|}{\sqrt{-\lambda(m_{a_1}^2, m_{12}^2, m_\pi^2), \lambda(m_{a_1}^2, m_{13}^2, m_\pi^2), \lambda(m_{a_1}^2, m_{23}^2, m_\pi^2)}}, \quad (2.23)$$

where $\lambda(x, y, z) = x^2 + y^2 + z^2 - 2xy - 2yz - 2zx$ and m_{ij} the invariant mass of the 2π system (i, j).

The distributions of the angle $\cos\theta^*$ and $\cos\psi$ which depend on the τ polarization are different for the two final states and can be found in [31, 32].

2.4.4 Comparison of Different Decay Channels

The sensitivity for the different channels is usually described in terms of the “figure of merit”. The sensitivity S is defined as $S = 1/(\sqrt{N} \Delta P_{\tau-})$, where N is the number of decays of the corresponding mode. This number does not include the different branching ratios. The sensitivity is shown in figure 2.7. As the branching ratios are not included in this figure, table 2.2 shows the corresponding weights ($\propto 1/\sigma_{P_\tau}^2$). The sensitivity and the weights are obtained by assuming perfect acceptance and no systematic error.

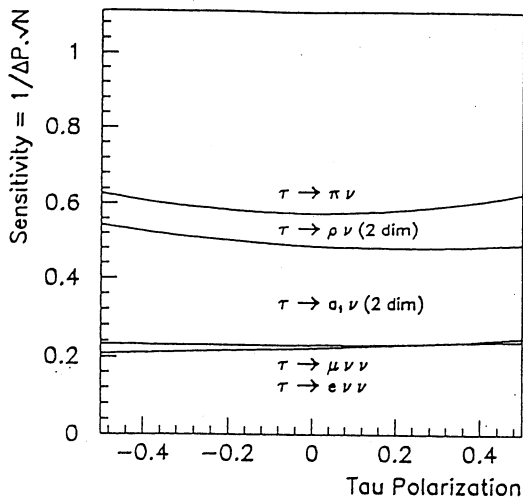


Figure 2.7: Sensitivity S for the different decay channels [33].

The pion and the ρ channel show up as the channels with the maximum information about the polarization for perfect detector conditions. In section 5.5 the actually measured numbers are compared for the different channels.

2.5 Observables A_τ , A_e , ξ , ρ and δ in $\tau \rightarrow \mu\nu\nu$ Decays

After the overview given in the sections 2.4.1–2.4.3 the possibilities of measuring A_τ (and furthermore A_e , ξ , ρ and δ as well) using the muon-channel are described in this

Channel	$e\nu\nu$	$\mu\nu\nu$	$\pi\nu$	$\rho\nu$	$a_1\nu$
Sensitivity \mathcal{S}	0.22	0.22	0.60	0.52	0.24
Branching Ratio	0.18	0.18	0.11	0.23	0.07
Weight	0.07	0.07	0.32	0.50	0.03

Table 2.2: Sensitivities and weights for different decay channels [93].

section. Every formula is valid for the electron-channel as well—only the mass needs to be exchanged. For the basic understanding section 2.5.1 explains in some detail how the momentum spectrum is obtained. Then the angular information will be used to get information about A_e , ξ , ρ and δ and increase the accuracy in determining A_τ in section 2.5.2.

In order to focus on the fundamental physics of these processes, they will be considered only in the Born approximation. Radiative effects are introduced later (see section 2.6).

The discussion of the observables is made in terms of A_e and A_τ which are essentially the ratio of vector to axialvector couplings. These observables are more appropriate for the discussion of the methods described in this thesis than the usual asymmetries described in section 2.2.

2.5.1 Dependence of the Momentum Spectrum on Polarization and Lorentz-Structure

In Born approximation the (leptonic) decay of the τ can be considered as a decay into a ν_τ and a W^\pm boson which decays into $\mu\nu_\mu$. This assumes “V-A” structure as the underlying physics of the decay (charged current). Even though “V-A” structure is very well established in weak interaction [3] for the electron and the muon, there are only very few measurements for the τ [21]. Thus all the parameters describing the Lorentz-structure of the τ decay are kept within the formulas.

To compute the final momentum spectrum for the charged decay product (μ^-) three steps are needed:

- (i) The polar angle $\cos\theta$ of the τ^- and its polarization are determined from equation (2.3).
- (ii) The momentum and decay angle of the muon relative to the τ^- spin in the τ^- rest-frame are determined.
- (iii) The polar angle and momentum in the laboratory frame are determined by a subsequent Lorentz boost.

Step (i) is already explained in detail in section 2.1. For step (ii) one takes the muon decay formula from [30]. After summing over the spins of the final state muon the differential decay probability in the τ^- rest-frame is given by

Parameter	Predictions		Measurements
	"(V - A) _{τμ} "	"(V + A) _{τμ} "	
Michel Parameter ρ	3/4	3/4	0.731 ± 0.030 [21]
Low energy Parameter η	0	0	none
Asymmetry Parameter ξ	+1	-1	none
Asymmetry Parameter δ	3/4	3/4	none

Table 2.3: Predictions and measurements of τ decay parameters.

$$\begin{aligned}
\frac{d^2\Gamma(x^*, \cos\theta^*)}{dx^* d\cos\theta^*} &= \frac{m_\tau^5 G_F^2}{32\pi^3} \left[1 + \left(\frac{m_\mu}{m_\tau}\right)^2 \right] \sqrt{x^{*2} - x_0^{*2}} \\
&\left\{ \left[x^*(1-x^*) + \frac{2}{9}\rho(4x^{*2} - 3x^* - x_0^{*2}) + \eta x_0^*(1-x^*) \right] \right. \\
&\left. - \frac{1}{3}\xi\sqrt{x^{*2} - x_0^{*2}} \cos\theta^* \left[1 - x^* + \frac{2}{3}\delta(4x^* - 3 - \frac{m_\mu}{m_\tau}x_0^*) \right] \right\}, \quad (2.24)
\end{aligned}$$

where $G_F = 1.16637(2) \cdot 10^{-5} \text{ GeV}^{-2}$ (Fermi coupling constant) [3],

$$x^* = \frac{E_\mu^{cms}}{E_\mu^{cms,max}} \quad \text{and}$$

$$x_0^* = \frac{m_\mu}{E_\mu^{cms,max}} = 0.117, \quad \text{with}$$

$$E_\mu^{cms,max} = \frac{m_\tau}{2} \left[1 + \left(\frac{m_\mu}{m_\tau}\right)^2 \right] = 0.895 \text{ GeV}.$$

(2.25)

The angle between the momentum of the μ^- with respect to the spin direction of the τ^- is denoted by $\cos\theta^*$. The ansatz used is the most general four-fermion interaction consisting of scalar, vector, axial vector, pseudoscalar and tensor operators. The relative strength and phase of these specific interactions are characterized by the parameters ρ , η , ξ , δ (see [3] and [30] for details). The parameter ρ must not be confused with ρ_0 in equation (2.6) describing the Higgs sector of the Standard Model. The predictions for the “V-A” and “V+A” structure at both vertices (muon and τ) of the W for $\tau \rightarrow \mu\nu\nu$ decays are given in table 2.3 (together with the measurements carried out so far).

To treat the equation analytically some simplifications have to be made. The ratio $m_\mu/m_\tau = 0.06$ can safely be neglected in the overall normalization factor. Furthermore it shows up in the last term with a factor x_0^* . This product of two small quantities (≈ 0.007) can be neglected as well. The parameter η has a factor x_0^* together with a quantity smaller than 1. As η is predicted to be 0, ηx_0^* is a small quantity even for slight “V+A” contributions to the Lorentz-structure and is also neglected. The term $\sqrt{x^{*2} - x_0^{*2}}$ is a

global factor. For energies of the decay particle not too close to x_0^* , this term can be set simply to x^* . Using the same argument the term $\frac{2}{9}\rho x_0^{*2}$ is dropped as well. Clearly all these approximations have to be checked with a full simulation of this process (see appendix A.2).

Equation (2.24) becomes

$$\frac{d^2\Gamma(x^*, \cos\theta^*)}{dx^* d\cos\theta^*} = \frac{m_\tau^5 G_F^2}{32\pi^3} x^{*2} \left\{ \left[(1-x^*) + \frac{2}{9}\rho(4x^*-3) \right] - \frac{1}{3}\xi \cos\theta^* \left[1-x^* + \frac{2}{3}\delta(4x^*-3) \right] \right\}. \quad (2.26)$$

It should be stressed that η has vanished from this equation due to the approximations. The three parameters ρ , δ and ξ are left.

The τ^- rest-frame has to be boosted by a Lorentz transformation into the laboratory-frame. Starting with the full Lorentz transformation, two approximations are used: m_τ/E_τ and m_μ/E_μ^{CMS} are set to zero. It is not quite clear that setting m_μ/E_μ^{cms} to zero is valid as E_μ^{cms} may get as small as m_μ . Nevertheless Monte Carlo shows (see appendix A.2) that this is a good approximation as long as only particles with some minimum momentum in the *laboratory-frame* are used. The Lorentz transformation becomes (see appendix A.1)

$$x = \frac{x^*}{2}(1 + p \cos\theta^*), \quad \text{where} \quad (2.27)$$

$$x = \frac{E_\mu}{E_\tau} \quad (\text{both in the laboratory - frame})$$

and p is the helicity state of the τ^- . What remains is to transform the CMS energy into the laboratory-frame and to integrate over $\cos\theta^*$ (see appendix A.1), as θ^* is not a measurable quantity. The result is (now using the mean helicity P_{τ^-})

$$\begin{aligned} \frac{d\Gamma(x)}{dx} &= \frac{m_\tau^5 G_F^2}{192\pi^3} h^\mu(x; \xi P_{\tau^-}, \rho, \delta), \text{ with} \\ h^\mu(x; \xi P_{\tau^-}, \rho, \delta) &= [h_0^\mu(x; \rho) - \xi P_{\tau^-} h_1^\mu(x; \delta)], \\ h_0^\mu(x; \rho) &= 2 - 6x^2 + 4x^3 + \frac{4}{9}\rho(-1 + 9x^2 - 8x^3) \\ h_1^\mu(x; \delta) &= -\frac{2}{3} + 4x - 6x^2 + \frac{8}{3}x^3 + \frac{4}{9}\delta(1 - 12x + 27x^2 - 16x^3) \end{aligned} \quad (2.28)$$

Setting ρ , δ and ξ to their ‘‘V-A’’ values leads to equation (2.18) already discussed.

Looking only at the momentum of the decay particles (keeping in mind, that the corresponding $\cos\theta$ range must be symmetrical—see section 2.2) one is able to get in principle a measurement of three quantities: $\xi \times P_{\tau^-}$, ρ and δ . It should be stressed that it is not possible to distinguish between a “V-A”-breaking effect ($\xi \neq 1$) and a finite polarization, if only the momentum of the particle is measured. The parameter ρ can be determined, while the sensitivity with respect to δ is rather small, as the δ dependent term is suppressed by the mean polarization (roughly 16%).

2.5.2 Angular Information

To take the angular information of the τ into account one can only use the angle of the final muon. Later, this approximation is found to be good for particles with momenta larger than 3 GeV. Combining equation (2.3) and (2.28), this is done in the following way:

$$\begin{aligned}
\frac{d^2 \sigma^{Born}}{d\cos\theta dx}(s, \cos\theta, x) &= \frac{d\sigma^{Born}}{d\cos\theta}(p = +1, s, \cos\theta) [h_0^\mu(x; \rho) - \xi h_1^\mu(x; \delta)] + \\
&\frac{d\sigma^{Born}}{d\cos\theta}(p = -1, s, \cos\theta) [h_0^\mu(x; \rho) + \xi h_1^\mu(x; \delta)] \\
&= \left\{ (1 + \cos^2\theta)F_0(s) + 2\cos\theta F_1(s) \right\} h_0^\mu(x; \rho) + \\
&\left\{ (1 + \cos^2\theta)F_2(s) + 2\cos\theta F_3(s) \right\} \xi h_1^\mu(x; \delta) \quad (2.29) \\
&\stackrel{(s=M_2^2)}{=} \left\{ (1 + \cos^2\theta) + 2\cos\theta A_e A_\tau \right\} h_0^\mu(x; \rho) + \\
&\left\{ (1 + \cos^2\theta)A_\tau + 2\cos\theta A_e \right\} \xi h_1^\mu(x; \delta) F_0(M_2^2) \quad (2.30)
\end{aligned}$$

The result is a formula which describes the cross-section in terms of the polar angle $\cos\theta$ and the momentum x of the τ decay product. One is now able to use all the information available from a track to extract different parameters from equation (2.29). To explain the basic possibilities of different measurements it is enough to consider the formula on the peak (equation 2.30):

- *A Measurement of the Production Parameters A_e and A_τ .* This can be obtained by assuming “V-A” in the decay process. Using the angular and momentum information allows one to be sensitive to A_e , A_τ and the product $A_e A_\tau$. When integrating over the angle one is sensitive only to A_τ . Comparing equation (2.29) with those given in section 2.2 shows that fitting the full expression to the data gives a measurement of A_{pol} , A_{FB} and A_{pol}^{FB} simultaneously. But as those asymmetries are quantities merely designed to measure A_e and A_τ , the fit to the combined momentum and

$\cos\theta$ distribution is the best method to extract the desired information on A_τ and A_e . It should be stressed that the sensitivity to A_τ itself becomes slightly higher using the angular information in addition to the momentum, because of the correlation between A_e and A_τ due to the term $2\cos\theta A_e A_\tau$. For the case of lepton universality the 2-dimensional equation clearly gives a much better sensitivity to A_{lepton} than a polarization measurement only. More quantitative statements will be given in section 2.6.6.

- *A Measurement of the Decay Parameters ρ , ξ and δ .* For this purpose the production parameters are fixed to their values given by the measured forward-backward asymmetries and the widths of the electron and τ channel. Then equation (2.29) depends on three parameters. The best way would be to extract them simultaneously. Unfortunately the statistics is at the present stage at LEP too poor for this task. To demonstrate the sensitivity with respect to the single parameters (e.g. for comparison with the correlation formalism given in [34]) results are given in section 2.6.6 on Monte Carlo.
- *A Measurement of One Decay Parameter and One Production Parameter.* This is of particular interest, as the relevant quantities of the τ production and decay should be measured together. For this purpose it is necessary again to concentrate on some interesting parameters. As ρ is measured quite accurately by [21], it is fixed to its measured value, while ξ and δ have not been measured so far at all. Looking at the possibility of "V-A" or "V+A" at both vertices of the W in the τ decay, ρ and δ have in both cases the value $3/4$, while ξ is either 1 ("V-A") or -1 ("V+A"). Therefore A_τ and ξ are chosen to be measured simultaneously. Furthermore the possibility exists to incorporate the measurement of A_τ from the forward-backward asymmetry in the τ channel as well. This can be done by using this measurement as a constraint in the fit.

2.6 Radiative Corrections and their Implementation

Radiative corrections contribute significantly to the shape of the momentum distributions. Two different corrections have to be considered:

- (i) QED. At first order they consist of all diagrams with an additional real photon (figure 2.8 right) or virtual photon loops (figure 2.8 left). Furthermore bremsstrahlung of the decay product (muon) must be taken into account. As they form a gauge invariant subset and depend on the experimental cuts, it is sensible to separate them from the
- (ii) Electroweak corrections. They consist of all the other possible one-loop diagrams as shown in figure 2.9 (modifications of the propagator γ , Z^0) and in figure 2.10 (box diagrams with two massive boson exchange). For

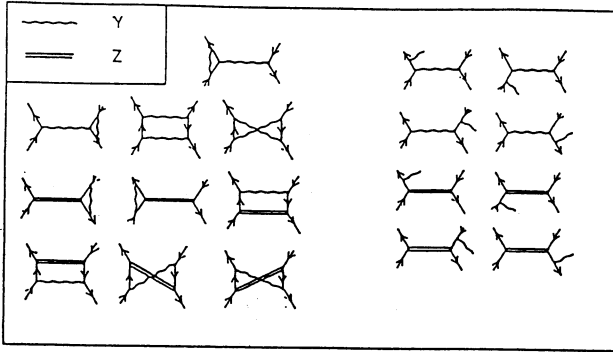


Figure 2.8: *QED corrections to $e^+e^- \rightarrow \tau^+\tau^-$ [26].*

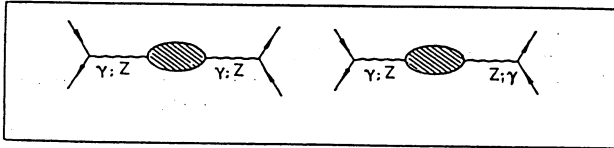


Figure 2.9: *Propagator corrections to $e^+e^- \rightarrow \tau^+\tau^-$ [26].*

the case of the τ (and clearly all lighter fermions), the vertex corrections in figure 2.10 consist only of W^\pm and Z^0 virtual states. These do not depend on experimental cuts.

Both radiative corrections can either be treated via a full simulation of the radiation processes with the Monte Carlo technique (section 2.6.3) or in a (semi-)analytical way (sections 2.6.5).

While the QED corrections are very important with respect to the experimental conditions, as they change the shape of the production (2.3) and decay formula (2.28), the electroweak corrections can be treated the following way (see [26] for a complete study).

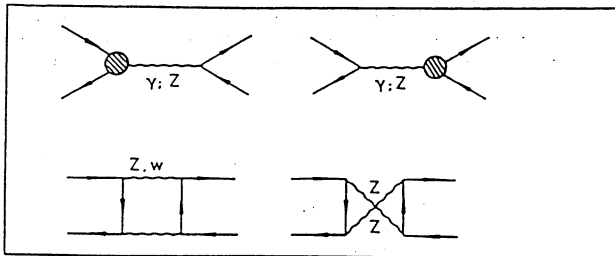


Figure 2.10: *Vertex corrections and box contributions to $e^+e^- \rightarrow \tau^+\tau^-$ [26].*

2.6.1 Electroweak Radiative Corrections

The electroweak radiative corrections do not depend on experimental cuts and contain information about hidden physics (e.g. t^+t^- - loops). The radiative corrections are closely related to the renormalization scheme—the way “physical” observables are obtained. The so called on-shell renormalization scheme uses the three constants $\alpha_0 = 1/137.036$ (measured by the magnetic moment anomaly $g - 2$ of the electron), the Fermi coupling constant $G_F = 1.16637 \times 10^{-5} \text{ GeV}^{-2}$ (measured by the muon decay rate) and the mass of the Z^0 M_Z . The underlying concept of this choice is to take those constants as parameters of the theory which are measured most precisely. Then the sine of the Weinberg angle $\sin^2\theta_W$ is fixed by the relation

$$\sin^2\theta_W \equiv 1 - \frac{M_W^2}{M_Z^2}. \quad (2.31)$$

So, the ratio of the physical masses of the W^\pm and the Z^0 defines the Weinberg angle. Because M_W itself is none of the three fundamental constants mentioned above it is related to the low energy Fermi coupling constant G_F in leading order by

$$M_W^2 \sin^2\theta_W = \frac{\pi\alpha_0}{\sqrt{2}G_F} \equiv A_0^2 = (37.281 \text{ GeV})^2. \quad (2.32)$$

Hence, $\sin^2\theta_W$ is given by

$$\sin^2\theta_W = \frac{1}{2} \left(1 - \sqrt{1 - \frac{4A_0^2}{M_Z^2}} \right). \quad (2.33)$$

While the implication of electroweak radiative corrections on a specific process (here $e^+e^- \rightarrow l^+l^-$) will be considered below, these corrections do change already the simple tree-level relations (2.32) and (2.33). These changes are characterized by Δr which depends on top quark and Higgs masses and relates the low energy parameter G_F to the high energy parameter M_W . The corresponding relations are

$$M_W^2 \sin^2\theta_W = \frac{A_0^2}{1 - \Delta r} \quad \text{and} \quad \sin^2\theta_W = \frac{1}{2} \left(1 - \sqrt{1 - \frac{4A_0^2}{M_Z^2(1 - \Delta r)}} \right). \quad (2.34)$$

The shift Δr is predicted to be 0.0574 ± 0.0013 [3] for a top and a Higgs mass of each 100 GeV.

Keeping these relations in mind, the radiative corrections are discussed for the Z^0 production and decay. They are separated into the vacuum polarization ($\cdots \bigcirc \cdots$), vertex corrections ($\cdots \triangleleft$) and box corrections ($\begin{array}{c} \diagup \quad \diagdown \\ \diagdown \quad \diagup \end{array}$). All those corrections consist of a real and an imaginary part, which have to be treated separately. For an estimate of the size, figure 2.11 shows the different contributions in descending order of magnitude.

The individual contributions are discussed in some detail:

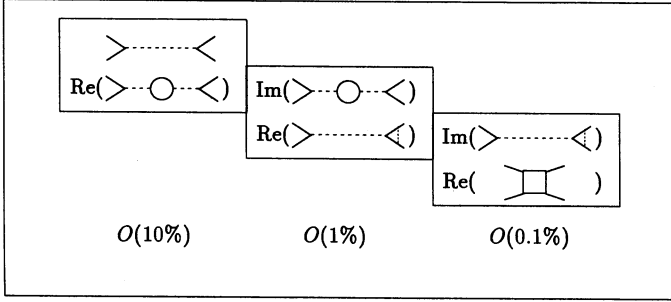


Figure 2.11: Size of electroweak radiative corrections.

- The *Vacuum Polarization* consists of three different contributions: The Z^0 exchange ($\text{---}\overset{Z}{\circ}\text{---}$), the γ - Z^0 interference ($\text{---}\overset{\gamma}{\circ}\text{---}\overset{Z}{\circ}\text{---}$) and the γ exchange ($\text{---}\overset{\gamma}{\circ}\text{---}$).

The last contribution is taken into account by a redefinition of the electromagnetic coupling constant α_0 :

$$\alpha_0 \rightarrow \alpha(s) = \frac{\alpha_0}{1 - \text{Re}\{\Delta\alpha(s)\} - i\text{Im}\{\Delta\alpha(s)\}}, \quad (2.35)$$

with $\alpha_0 = 1/137.04$ and $\Delta\alpha(s = M_Z^2) = 0.0602 + i0.0134$ [26]. This corresponds to a change of $|\alpha(s)|$ from $1/137.0$ at $s = 0$ to $1/128.8$ at $s = M_Z^2$.

The ($\text{---}\overset{Z}{\circ}\text{---}$) contribution leads to a modified propagator. At the same time it is very convenient to multiply this modified propagator with the factor $e/(2 \sin\theta_W \cos\theta_W)$ squared which is usually part of the vertex term (see equation 2.1). The resulting expression is

$$\underbrace{\frac{e^2}{4 \sin^2\theta_W \cos^2\theta_W}}_I \frac{1}{1 + \hat{\Pi}_Z(s)} \underbrace{\frac{1}{s - M_Z^2 + i \frac{\text{Im}\Sigma_Z(s)}{1 + \hat{\Pi}_Z(s)}}}_{II}. \quad (2.36)$$

The functions $\hat{\Pi}(s)$ and $\Sigma_Z(s)$ are the so called self energies and can be found e.g. in [26]. Using equations (2.34) the term “I” can be absorbed in an effective $\bar{\rho}(s)$ (compare with nonradiative form in equation 2.6):

$$\frac{e^2}{4 \sin^2\theta_W \cos^2\theta_W} \frac{1}{1 + \hat{\Pi}_Z(s)} = \sqrt{2} G_F M_Z^2 \underbrace{\rho_0 \frac{1 - \Delta\rho}{1 + \hat{\Pi}_Z(s)}}_{\bar{\rho}(s)}, \quad \text{where}$$

$$\bar{\rho}(s) = \rho_0(1 + \Delta\rho(s)). \quad (2.37)$$

$1 - \Delta r$ includes the modifications of equation (2.6) due to the corrections going from the low energy parameter G_F to the high energy parameter M_Z (or M_W) as mentioned above for equation (2.34). The $\bar{\rho}(s)$ itself is needed to connect the charged current parameter G_F to the neutral current process considered here. $\Delta\rho(s)$ depends on the Higgs and top mass. For a special set $m_H = 200 \text{ GeV}$ and $m_t = 150 \text{ GeV}$ the value for $\Delta\rho(s = M_Z^2)$ is 0.010. Term “ Π ” can be absorbed in the “physical” (thus observable) width Γ_Z of the Z^0 by setting

$$\frac{Im\Sigma_Z(s)}{1 + \hat{\Pi}_Z(s)} = \frac{s}{M_Z} \Gamma_Z. \quad (2.38)$$

This leads to the $\chi(s)$ as given in equation (2.5). So, the imaginary part of the $(\cdot \cdot \cdot \overset{Z}{\circ} \cdot \cdot \cdot)$ leads to the propagator with the finite width of the Z^0 .

The last correction of this type is the γ - Z^0 mixing $(\cdot \cdot \cdot \overset{Z}{\circ} \cdot \cdot \cdot)$. The real part of it can be taken into account by a redefinition of $\overline{\sin^2\theta_W}$ into an s dependent “effective” $\overline{\sin^2\theta_W}(s)$:

$$\begin{aligned} \sin^2\theta_W \rightarrow \overline{\sin^2\theta_W}(s) &= \sin^2\theta_W \left(1 - \frac{\cos\theta_W}{\sin\theta_W} \frac{\hat{\Pi}_{\gamma,Z}(s)}{1 + \hat{\Pi}_\gamma(s)} \right) \\ &= \sin^2\theta_W (1 + \Delta\kappa(s)). \end{aligned} \quad (2.39)$$

The interesting observable is thus $\overline{\sin^2\theta_W}(s = M_Z^2)$. This redefinition of $\sin^2\theta_W$ clearly affects the weak couplings g_v , via equation (2.2). For a top mass of 150 GeV and a Higgs mass of 200 GeV $\Delta\kappa = 0.027$ [35]. The dependence on Higgs and top mass is not negligible (see discussion in section 5.5). It should be stressed that all corrections so far result in a redefinition of α_0 , ρ_0 and $\sin^2\theta_W$ and the introduction of a complex propagator. All these corrections are universal in the sense that they do not depend on the individual initial/final state. This is just a consequence of the fact that the effects described so far have been absorbed in a redefinition and modification of the propagator.

- The *Vertex Corrections* for photon exchange can be absorbed in a flavour dependent redefinition of $\sin^2\theta_W$:

$$\sin^2\theta_W \rightarrow \overline{\sin^2\theta_{W,f}}(s) = \overline{\sin^2\theta_W}(s) (1 + \Delta\kappa_f(s)). \quad (2.40)$$

$\Delta\kappa_f$ is the same for all leptons but different for quarks. For leptons one gets $\Delta\kappa_f(M_Z^2) = 3.2 \times 10^{-3}$ for a top mass of 150 GeV and a Higgs mass of 200 GeV . The dependence on Higgs and top mass is very small.

The vertex corrections for Z^0 exchange can be absorbed in a redefinition of the weak coupling constants g_{v_f} and g_{a_f} via

$$\begin{aligned}
g_v, \rightarrow \bar{g}_v, (s) &= \sqrt{\bar{\rho}_f(s)} (I_3^f - 2 Q_f \overline{\sin^2 \theta_{W,f}}(s)) \\
g_a, \rightarrow \bar{g}_a, (s) &= \sqrt{\bar{\rho}_f(s)} I_3^f, \\
\bar{\rho}_f(s) &= \bar{\rho}(s)(1 + \Delta\rho_f(s)).
\end{aligned}$$

$\Delta\rho_f(s = M_Z^2)$ is calculated to be -0.006 [35] and shows only a very weak dependence on the top and the Higgs mass. As measurements within this thesis are only ratios of \bar{g}_v, \bar{g}_a , this correction turns out to cancel for the relevant observables.

All corrections due to the real part of the vertex corrections are different for leptons and quarks. As only leptons are involved these changes are not relevant here. The imaginary part of the vertex correction is neglected.

- The *Box corrections* are of the order $\frac{\alpha}{\pi}$ of the photon exchange amplitude near the peak as they are non-resonant [26]. Therefore they can be safely neglected.

After looking at the different radiative corrections and the resulting modifications in $\sin^2 \theta_W$, ρ_0 and α_0 , the differential cross-section as given in equation 2.3 can be kept if the relevant substitutions are made. This is called the Improved Born Approximation. The results for g_v and g_a (and correspondingly $\sin^2 \theta_W$) in the Improved Born Approximation must then be interpreted the way explained above.

2.6.2 QED Radiative Corrections

In this section the effects of QED corrections are considered. In principle vertices as seen in figure 2.1 have to be modified including graphs as shown in figure 2.8. Radiated photons can originate from the

- (i) initial-state fermion-pair (e^+e^-),
- (ii) final-state fermion-pair ($\tau^+\tau^-$) or
- (iii) final-state charged particle (e.g. muon or pion).

The last point refers to real photons radiated from the decay products—a process not mentioned so far.

The photons of process (i) usually vanish into the beam pipe because they are more or less collinear to the incoming beam. Hence, they escape the apparatus undetected. On the other hand, the photons of both kinds of final-state radiation ((ii) and (iii)) are measurable in the detector. Before studying them in details their influence onto the measurement is discussed.

- *Kinematic effects:* For equations (2.28) and (2.29) the τ energy E_τ is used to build the quantity $x = p_\mu/E_\tau$. As the ν_τ escapes the detection, E_τ is not an observable. So, E_τ can be taken to be E_{Beam} which is strictly true only in the absence of radiative correction. But, if photons are radiated from the beam particles (electrons), they lose energy— E_τ is smaller than the beam energy. Thus x is overestimated by setting $E_\tau = E_{Beam}$ due to process (i). The same thing happens if a τ in the final state radiates a photon.

Radiation of the decay particle (e.g. muon, e or pion) reduces the energy of the particle which is measured. This leads also to smaller x values, provided the energy of the radiated photon is neglected.

For the case of the channel $\tau \rightarrow \mu\nu\nu$ this effect changes the polarization by roughly 5 – 10% (see section 2.6.6).

- *Direct QED effects:* Radiation of a real photon, which carries spin 1 can lead to a spin flip of the radiating spin $\frac{1}{2}$ particle. This clearly can influence the net polarization. Nevertheless, the effect is shown to be around 0.21% in the polarization [25] and can therefore be safely neglected.

2.6.3 Monte Carlo Simulation of τ Production and Decay including Radiative Corrections with KORALZ

This section describes briefly the physical content of the Monte Carlo program KORALZ used throughout this thesis. KORALZ was written by S. Jadach, B.F. Ward and Z. Was and it is described in detail in [36]. It simulates the processes $e^+e^- \rightarrow \mu^+\mu^-, \tau^+\tau^-$ at energies around the Z^0 -peak including the following physical effects:

- Multiple QED hard bremsstrahlung in the initial-state and single photon in the final-state.
- $O(\alpha)$ radiative corrections from the standard electroweak model [5].
- Longitudinal spin polarization of the beams (not used).
- the most frequent decay modes of the τ : $\nu\nu e$, $\nu\nu\mu$, $\nu\pi$, $\nu\rho$, νK_1 , νK^* , νa_1 , $\nu 4\pi$, $\nu 5\pi$, $\nu 6\pi$.
- Spin polarization effects in τ decay process.
- Single bremsstrahlung in the τ decay modes.

It therefore takes all the radiative effects as described in section 2.6 into account. The limitations relevant for this thesis are:

- No QED initial-final state bremsstrahlung interference included for multiple QED hard bremsstrahlung in the initial state.

- QED $O(\alpha)$ corrections in the τ decay are only in “leading-logarithmic approximation”.

The last two points do not lead to any sizeable bias (see [25] and section 2.6.2).

KORALZ generates only the kinematics of an event. The Monte Carlo program used for the detector is described briefly in section 4.1.1.

2.6.4 Monte Carlo Technique

As equation (2.18) is not true any more once radiative corrections are incorporated, KORALZ can be used to obtain a measurement of different parameters from the data. This has the advantage that radiative corrections are taken into account at the level of the simulation as described in section 2.6.3. On the other hand one has to rely completely on the simulation and the statistical error of the Monte Carlo sample enlarges the total error. The method for fitting the momentum spectrum is described in this section.

Events are generated separately with positive and negative τ helicity leading to the momentum distributions f_- and f_+ , respectively. Equation (2.18) depends linearly on P_{τ^-} . This property does not change once one includes radiative corrections. This allows one to fit a linear combination of $f_-(x)$ and $f_+(x)$ according to

$$f(x; N, p) = \frac{N}{2} \{ (1 + P_{\tau^-}) f_+(x) + (1 - P_{\tau^-}) f_-(x) \}. \quad (2.41)$$

This strategy is unbiased as long as the simulation describes the data. This is true at the level we need for the measurement of P_{τ^-} (see section 2.6.3). As a check this method and a simple fit to equation (2.18) (or the radiative case) can be performed. This gives a hint to the systematic error induced.

It should be stressed that the Monte Carlo method does not allow one to use the angular information via a simple superposition of two functions as done in equation (2.41).

2.6.5 Implementation of QED Radiative Corrections in a Semi-analytical Way

The Monte Carlo method can get quite sophisticated, especially for complex fitting procedures with more than one dimension or more than one parameter (as in section 2.6.4). In this case it is easier to use a (semi-)analytical expression to fit the data. Such an expression is derived in this section.

The strategy used for taking the QED radiative corrections into account semi-analytically is developed in [25]: In principle all effects do interfere, which means they have to be treated together. However, a good approximation is to look at it as a noninterfering fragmentation process as shown in figure 2.12 (called the “leading-logarithmic approximation”).

The process starts with (from left to right) the initial-state fermion-pair e^+e^- which is allowed to radiate n photons which have the total energy of \sqrt{vs} . The remaining energy $\sqrt{s(1-v)}$ is used to produce the $\tau^+\tau^-$ via Z^0 - or photon-exchange. Carrying on with the produced τ^- only, it radiates a photon according to the fragmentation function D_τ (Altarelli-Parisi distribution) and loses the fraction $(1-z)$ of its energy. The subsequent

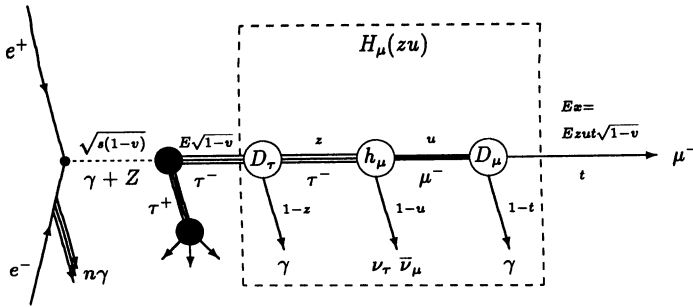


Figure 2.12: Radiative corrections as a chain of fragmentation processes.

τ decay is described with the “fragmentation function” h_μ , the function given in (2.28). The $\nu_\tau - \bar{\nu}_\mu$ system carries the fraction u of the τ energy. At last the bremsstrahlung photon of the muon is radiated described by the function D_μ . In the end the muon has the fraction $x = uzt\sqrt{1-v}$ of $\sqrt{s}/2$.

The initial-state radiation is accounted for by taking a convolution over the Born cross-section [37]. One substitutes the functions $F_i(s)$ given in equation (2.4) by

$$F_i^*(s, x) = \int_0^{1-x^2} \frac{dv}{\sqrt{1-v}} \rho(v) F_i(s(1-v)). \quad (2.42)$$

The functions F_i^* do now depend on x because of the allowed integration range. The radiation function $\rho(v)$ (see appendix A.3) is infinite at $v = 0$, but the integration can be performed out. The effect of the initial-state radiation is shown in figure 2.13. As A_{pol} depends only weakly on \sqrt{s} the influence is very small. However, A_{FB} is steep with respect to \sqrt{s} and thus is sensitive to initial-state radiative corrections. It is therefore essential to correct for this effect if the angular information is used (section 2.5.2).

Considering the first step of figure 2.12 the whole $\tau^+\tau^-$ system is moving because of the initial-state photons. A check of the angular distribution in [37] and the results in section 2.6.6 indicate that neglecting this movement does not lead to a bias. With this approximation the master formula for all corrections is given by (the terms are: initial-state radiation, final-state radiation, τ decay and bremsstrahlung of the muon, respectively):

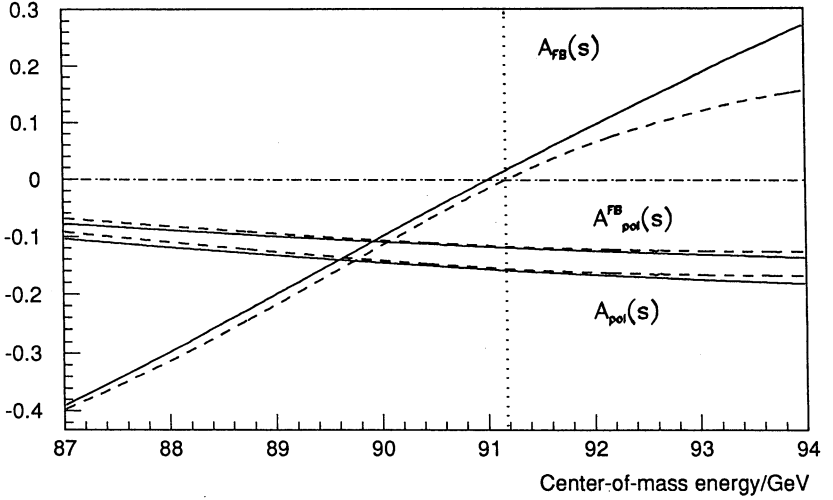


Figure 2.13: A_{pol} , A_{FB} and A_{pol}^{FB} with (dashed line) and without initial-state radiative corrections (solid line).

$$\begin{aligned}
 \frac{d^2\sigma}{d\cos\theta dx}(s, \cos\theta, x) &= \frac{1}{2} \left\{ \int_0^{1-x^2} dv \rho(v) \frac{d\sigma^{Born}}{d\cos\theta}(p = +1; s(1-v), \cos\theta) \right. \\
 &\quad \int_0^1 dz D_\tau \left(\frac{m_\tau^2}{s(1-v)}, z \right) \\
 &\quad \int_0^1 du h^\mu(u; p = +1) \\
 &\quad \int_0^1 dt D_\mu(t) \delta(x - uzt\sqrt{1-v}) \\
 &\quad \left. + \dots p = -1 \dots \right\}, \tag{2.43}
 \end{aligned}$$

where $h^\mu(x; p)$ is given by equation (2.28). The functions $D_\tau(m_\tau^2, z)$, $D_\mu(t)$ are given in appendix A.3. There the rearrangements and simplifications are done as well, which lead to

$$\frac{d^2\sigma}{dcos\theta dx}(s, \cos\theta, x; \rho, \delta, \xi) = \left[(1 + \cos^2\theta)W_0(s, x; \rho) + 2\cos\theta W_1(s, x; \rho) \right] + \left[(1 + \cos^2\theta)W_2(s, x; \delta) + 2\cos\theta W_3(s, x; \delta) \right] \xi,$$

$$\text{where } W_i(s, x; \rho/\delta) = \int_0^{1-x^2} \frac{dv}{\sqrt{1-v}} \rho(v) F_i(s(1-v)) H_{(i/2)}^\mu\left(\frac{x}{\sqrt{1-v}}; \rho/\delta\right). \quad (2.44)$$

The function H_0^μ and H_1^μ are the general (radiative) cases for the functions h_i^μ given in equation (2.28) and are given in appendix A.3, where $\rho(v)$ can be found as well. The bremsstrahlung distribution is $\rho(v)$ and must not be confused with the Michel parameter ρ or the parameter ρ_0 describing the Higgs sector of the Standard Model. To see the influence of the radiative corrections as given in equation (2.44), the functions W_i are plotted in figure 2.14.

Comparing the structure of equation (2.44) with that of (2.29), it becomes clear that all manipulations mentioned above *do not change the structure* of the nonradiative equation. This guaranties that all the statements concerning fitting momentum only or the combined momentum and $\cos\theta$ distribution (as given in 2.5.1, and 2.5.2) are still valid. Only W_i has to be used instead of $F_i h_{(i/2)}$. It is worth comparing equation (2.44) with the Born expression (equation 2.29) with respect to the dependence on the production parameters g_{a_e} , g_{v_e} , g_{a_τ} and g_{v_τ} in some detail: Equation (2.30) at $s = M_Z^2$ is dependent merely on A_e and A_τ , which are essentially the ratios g_{v_e}/g_{a_e} and g_{v_τ}/g_{a_τ} . This simple behaviour is not conserved going to equation (2.44) due to the convolution integral which has to take into account the function F_i over the whole range of s and not only at $s = M_Z^2$. Therefore every function W_i depends nontrivially on the parameters g_{a_e} , g_{v_e} , g_{a_τ} and g_{v_τ} itself (and not their ratios) via the convolution over the complete s range. But, having now a closer look to the convolution integral and using the fact that the function $\rho(v)$ in equation (2.44) shows a δ -function like behaviour with a sharp maximum at $v = 0$, the main contribution to the integral comes from F_i at $s = M_Z^2$. Therefore the W_i are expected to depend mainly on A_e and A_τ as given in equation (2.30). In other words: If a fit is performed to equation (2.44) fitting g_{v_e} and g_{v_τ} while fixing g_{a_e} and g_{a_τ} to some value, g_{v_e}/g_{a_e} and g_{v_τ}/g_{a_τ} should depend only weakly on g_{a_e} and g_{a_τ} . To give a quantitative understanding of this statement a check is performed: Integrating equation (2.44) over $\cos\theta$, a likelihood fit to

$$f(s, x; g_{v_\tau}, g_{a_\tau}, g_{v_e}, g_{a_e}) = \frac{1}{W_0} [W_0(s, x; g_{v_\tau}, g_{a_\tau}, g_{v_e}, g_{a_e}) + W_2(s, x; g_{v_\tau}, g_{a_\tau}, g_{v_e}, g_{a_e})] \quad (2.45)$$

is performed extracting A_τ as result (setting ρ , ξ and δ to their ‘‘V-A’’ values). The input reference values are $g_{a_{lepton}} = -0.5$ and $g_{v_{lepton}} = -0.040$. These are very close to the measured values $g_{a_{lepton}} = -0.498 \pm 0.002$ and $g_{v_{lepton}} = -0.039 \pm 0.008$ in [18]. These measurement errors are used to vary g_{a_τ} and g_{a_e} within more than 5σ . For 7268 Monte Carlo entries the results are shown in table 2.4. It becomes evident that the resulting

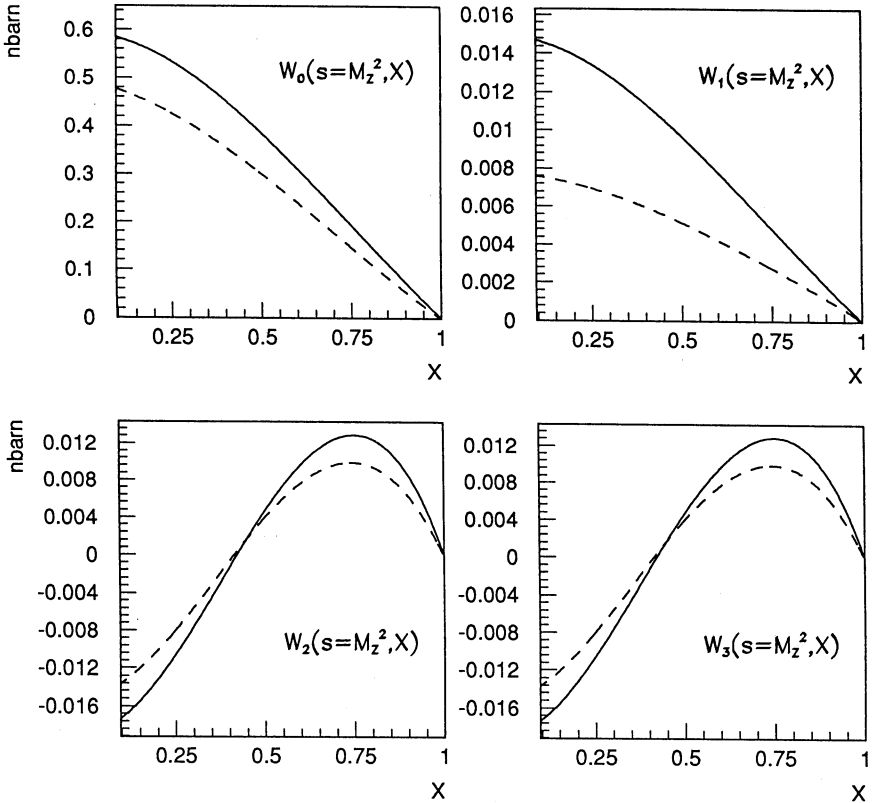


Figure 2.14: Comparison of the functions $W_i(s, x)$ with (dashed line) and without (solid line) radiative corrections.

changes in polarization are only marginal, and therefore equation (2.44) is sensitive only to the ratios A_e and A_τ as long as one stays at the peak. Going away from $s = M_Z^2$, this is not true anymore so that g_{a_e} and g_{a_τ} from the measurements of Γ_H have to be used.

Figure 2.15 shows the spectrum for the Standard Model polarization of about -16% with and without radiative corrections. Looking at the rather large change in the spectrum it is not surprising that the effect on the measured polarization is also large. Fitting the dashed line in figure 2.15 with equation (2.18) gives $(-8.6 \pm 5.1)\%$ while using the (correct) equation (2.45) gives $(-18.7 \pm 5.3)\%$. This change is a very large effect and makes it evident that radiative corrections have to be taken into account (compare e.g. with [25]).

Input			Fit result
Reference value $g_{a_l} = -0.500$	Ref. value $g_{v_e} = -0.040$		
change g_{a_s} by	change g_{a_r} by	change g_{v_s} by	change in P_{τ^-}
+0.009	-	-	< 0.00005
-	+0.009	-	+0.0002
+0.009	+0.009	-	+0.0002
-0.009	-	-	+0.0003
-	-0.009	-	+0.0001
-0.009	-0.009	-	+0.0008
-	-	+0.048	+0.0023
-	-	-0.045	-0.0010

Table 2.4: Change in polarization varying g_{a_s} , g_{v_s} and g_{a_r} within reasonable range.

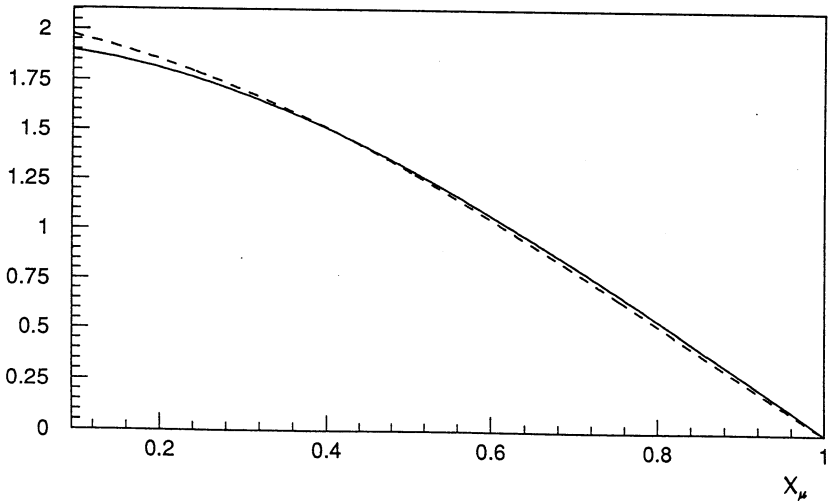


Figure 2.15: Momentum spectrum for muon for the Standard Model value of P_{τ^-} with (dashed line) and without (solid line) radiative corrections.

Fit-Method	Fit results				
	g_{v_e}/g_{a_e}	g_{v_τ}/g_{a_τ}	ξ	ρ	δ
1) Fit to simple momentum spectrum (2.18) without rad. corr.	not relevant	0.043 ± 0.026	fixed	fixed	fixed
2) Fit to momentum spectrum (2.45) including rad. corr.	fixed	0.094 ± 0.030	fixed	fixed	fixed

Table 2.5: Results for check with Monte Carlo (semi-analytical approach), part 1.

2.6.6 Monte Carlo Checks of Fitting Methods

To check the performance of the methods described above and to compare them several samples are used:

- (i) 10000 $\tau \rightarrow \mu\nu\nu$ at the generator level, momentum not smeared, all radiative effects switched on.
- (ii) 100000 $\tau \rightarrow \mu\nu\nu$ at the generator level, momentum smeared, all radiative effects switched on.
- (iii) 30000 $\tau \rightarrow all$, processed through the full detector simulation, no cuts are applied.

They are used to get tables 2.5, 2.6 and 2.7, where many combinations of fitting methods are compared. The input values for g_{a_e} and g_{a_τ} are -0.5 , those for g_{v_e} and g_{v_τ} are -0.040 ($g_v/g_a = 0.079$). This corresponds to a value of -15.6% for the polarization. The range for $x = p_\mu/E_{Beam}$ and $\cos\theta$ are $[0.1;0.95]$ and $[-0.9;0.9]$ respectively.

Fits (1 – 10) use sample (i) as “data”-sample. As the fitting methods using equation (2.44) do not yet include the resolution effects, nonsmearing is appropriate to check the method. Some comments to the results:

- Result (1) shows the necessity for taking radiative corrections into account (as already seen in section 2.6.2), which is done for result (2) where good agreement with the expected value is obtained. The effect of the radiative corrections is roughly $\Delta(g_{v_\tau}/g_{a_\tau}) \approx 0.05$.
- Result (3) shows the extension to the 2-dimensional distribution in momentum and $\cos\theta$. g_{v_e}/g_{a_e} can be measured as well and is found to be in agreement with the expected value. The correlation coefficient is given

Fit-Method	Fit results				
	g_{v_e}/g_{a_e}	g_{v_r}/g_{a_r}	ξ	ρ	δ
3) Fit to $x/\cos\theta$ distribution (2.44) including rad. corr.	0.043 ± 0.028	0.091 ± 0.029	fixed	fixed	fixed
4) As (3), assuming $g_v = g_{v_r} = g_{v_e}$	$0.068^{+0.016}_{-0.018}$		fixed	fixed	fixed
5) As (3), fixing $g_{v_e} = -0.040$, fitting ξ as well	fixed	$0.081^{+0.034}_{-0.028}$	$0.95^{+0.37}_{-0.32}$	fixed	fixed
6) As (3), fixing $g_{v_e} = g_{v_r} = -0.040$, $\delta = 3/4$, fitting ξ and ρ	fixed	fixed	0.58 ± 0.47	0.819 ± 0.068	fixed
7) As (6), but fixing $\rho = \delta = 3/4$	fixed	fixed	0.96 ± 0.30	fixed	fixed
8) As (6), but fixing $\xi = 1$, $\delta = 3/4$	fixed	fixed	fixed	0.773 ± 0.043	fixed
9) As (6), but fixing $\xi = 1$, $\rho = 3/4$	fixed	fixed	fixed	fixed	0.51 ± 0.29
10) As (6), but fixing $\rho = 3/4$	fixed	fixed	1.57 ± 0.56	fixed	$0.29^{+0.31}_{-0.20}$

Table 2.6: Results for check with Monte Carlo (semi-analytical approach), part 2.

by +0.15. It should be stressed once more, that the accuracy for measuring $g_{\nu_e}/g_{\alpha_e} \approx A_e$ in this case is mainly determined by the term $2\cos\theta A_e$ in equation (2.30), which is linear in A_e , while the measurement of the forward-backward asymmetry allows only a measurement quadratic in A (term $2\cos\theta A_e A_\tau$ in equation 2.30).

- Result (4) demonstrates the possibility of fitting $g_{\nu_{lepton}}/g_{\alpha_{lepton}}$ assuming lepton universality. The accuracy on $g_{\nu_{lepton}}/g_{\alpha_{lepton}}$ is slightly higher than the combined error in fit (3) due to a small correlation induced by the term $2\cos\theta A_e A_\tau$ in equation (2.30).
- For result (5) ξ is included as a fit parameter. It shows that equation (2.29) is quite sensitive to this parameter of "V-A" as well. As the main interest in this context is on the τ sector, g_{ν_e} has been fixed to -0.040 . For data it can be taken e.g. from the forward-backward asymmetry measurements in the electron channel. While the result on the polarization with respect to variation of g_{ν_e} is rather insensitive (see table 2.4), the result on ξ depends linearly on the value assumed for g_{ν_e} . The correlation coefficient of ξ and g_{ν_e}/g_{α_e} is 0.54.
- Result (6) shows a combined fit of ξ and ρ , setting g_{ν_e} and g_{ν_τ} to their Standard Model value. ξ and δ are found to be consistent with the input values. The correlation coefficient is -0.77 .
- Result (7) shows the possibility of measuring ξ as accurately as possible. ρ has to be taken from other (precise) experiments. So far ([3]) this would lead to the first measurement of this quantity.
- The sensitivity with respect to ρ can be seen in result (8), where ξ and δ are fixed to their Standard Model values.
- The same for δ is shown in result (9), where ξ and ρ are fixed to their Standard Model values.
- Result (10) shows the possibility of fitting ξ and ρ simultaneously. Both variables are rather strongly correlated (correlation coefficient -0.96) resulting in larger errors.

Using the Monte Carlo technique (section 2.6.4) for fully simulated events including detector effects, table 2.7 shows the corresponding results.

- Result (11) demonstrates again that the simple equation (2.18) is not sufficient.
- The effect of the radiative corrections is taken into account by choosing a sample of 100 000 events of the kind (*i*) for result (12): The result is already compatible with the input.

<i>Fit-Method</i>	<i>Fit results</i>
	g_{ν_e}/g_{α_e}
11) Fit simple equation (2.18) to sample (iii)	0.009 ± 0.026
12) Fit to sample (iii) per MC method (2.6.4), using a sample of 100 000 events of type (i)	0.059 ± 0.027
13) Fit to sample (iii) per MC method (2.6.4), using sample (ii)	0.087 ± 0.028

Table 2.7: *Results for check with Monte Carlo (MC approach).*

- Result (13) includes the finite resolution, because a smeared sample is used as for the fit. The effect is roughly 6% and hence not negligible.

The results demonstrate that both techniques (semi-analytical and Monte Carlo) work pretty well.

3. Experimental Setup

3.1 The LEP Collider

The electron-positron collider LEP ("Large Electron-Positron collider") at CERN in Geneva allows the study of the weak bosons (Z^0 and W^\pm) with a high precision. LEP has a circumference of 27 km crossing twice the French-Swiss border. The beam energies of up to 55 GeV , which are obtained with the first stage of LEP, allow the production of a large number of Z^0 . Four electron and four positron bunches are running in opposite direction in the same beam pipe. They collide at four different interaction points where the experiments ALEPH, DELPHI, L3 and OPAL are located. The design luminosity of LEP for 91 GeV center-of-mass energy is $1.7 \times 10^{31}\text{ cm}^{-2}\text{ sec}^{-1}$. LEP 100 started operation successfully in August 1989. Further plans for higher luminosities include the operation with 8 or even 32 bunches. In the next step LEP will be upgraded with superconducting cavities allowing CMS energies of roughly 200 GeV . This will allow the production of W^\pm boson pairs.

In the running periods in 1989 and 1990 roughly 140 000 to 190 000 Z^0 per experiment [15] have been collected at 11 different center of mass energies between 88 GeV and 95 GeV . The highest peak luminosity was $7 \times 10^{30}\text{ cm}^{-2}\text{ sec}^{-1}$ with currents of roughly 3.4 mA . A typical lifetime of a LEP fill was 10 hours, the longest lasted 22.5 hours. The integrated luminosity versus the time is shown in figure 3.1.

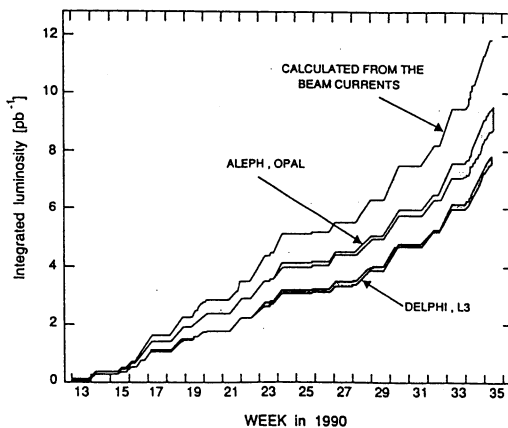


Figure 3.1: *Integrated luminosity versus time [15]. All LEP experiments and a measurement from the beam currents is shown.*

3.2 The ALEPH Experiment

- ¿El ALEPH ? - repetí.
- Sí, el lugar donde están, sin confundirse, todos los lugares del orbe, vistos desde todos los ángulos. [...]

From *El Aleph*, J.L. Borges¹

3.2.1 General Features of a LEP Experiment

A large fraction of the Z^0 decay into $q\bar{q}$ events. These hadronic events are quite complex, consisting on average of 20 charged tracks plus a similar number of neutral particles, which are distributed over the whole solid angle. For LEP experiments it is therefore essential to measure the momentum of charged tracks and the energy of neutral particles in as much of the solid angle as possible. Particle identification is essential to distinguish between different leptonic decays of the Z^0 and to study heavy quarks. For various measurements the luminosity has to be determined to an accuracy of 0.5 – 1.0 % using a measurement of the rate of small angle Bhabha events.

All these various requirements lead to a detector consisting of various (more or less independent) subdetectors. The general geometrical layout (common to all the LEP detectors) is a cylindrical detector divided into a so-called “barrel” and two “endcaps”. With this construction the whole solid angle is covered leaving only the beampipe in the center for particles to escape. At the same time it allows access for maintenance by just opening the detector via a movement of the endcaps.

The detector ALEPH (“A detector for LEP Physics”) is one of the four detectors at LEP. This detector is built and operated by a collaboration of 30 institutes from Europe, America and Asia. The complete description can be found in [38]. In this context it is sufficient to describe those parts which are relevant for this analysis in some detail.

3.2.2 Overview of the ALEPH Detector

The subdetectors and their main purpose are described here from the inner to the outer parts of the detector (see figure 3.2). Details are given in the following sections. The coordinate system for the description of the detector is defined with the z -axis pointing into the direction of the electron beam which goes from side B to side A of the detector. The horizontal axis is x and the vertical y . The electron/positron beams collide (ideally) at the origin of this coordinate system in the center of the detector. The (x,y) -plane

¹ - “The ALEPH ?”
- ‘Yes, the place where all places on earth are located without blending, seen from all viewpoints. [...]’

is often referred to as (r, ϕ) -plane. This implies the use of cylindrical coordinates: very often the polar angle θ is used, which describes the angle to the z direction (direction of electron beam).

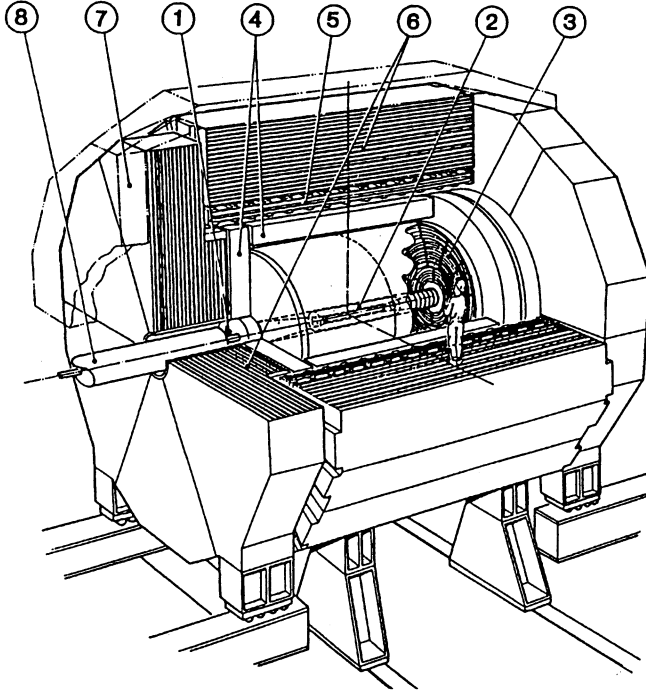


Figure 3.2: *The ALEPH Detector. The individual subdetectors are labeled by numbers: (1) luminosity monitors, (2) inner tracking chamber, (3) time projection chamber, (4) electromagnetic calorimeter, (5) superconducting coil, (6) hadronic calorimeter, (7) muon chambers and (8) superconducting quadrupoles.*

The *Beampipe* has a diameter of 16 cm and is mounted in the center of the detector and allows the beam to go through vacuum minimizing interaction with gas. It consists of $500\ \mu\text{m}$ thick aluminum-magnesium alloy. It supports the *Micro-Vertex Detector (MVD)*, a silicon-strip detector with a high spatial resolution for measurements near the interaction point (the MVD was completed in the beginning of 1991). The *Inner Tracking Chamber (ITC)* covers a larger solid angle and is mainly used for triggering purposes. It is a conventional drift chamber (wires along the z -axis) with high precision in the (r, ϕ) -plane covering a radial range from 13 cm to 29 cm . It measures up to 8 points of a track with an accuracy of $\approx 100\ \mu\text{m}$. The most important detector for tracking, the *Time Projection Chamber (TPC)*, measures charged tracks in three space dimensions. As the TPC is placed in a magnetic field of 1.5 T , charged tracks are curved. This curvature

is measured with the TPC and can be translated into a momentum. The combined momentum resolution of TPC and ITC is $\Delta p/p^2 = 0.8 \times 10^{-3} (GeV/c)^{-1}$ [39]. Furthermore information about dE/dx is provided by the TPC and is used to identify particles.

All parts described so far consist only of a barrel-part. The remaining subdetectors are divided into barrel and endcap. The TPC is surrounded by the *Electromagnetic Calorimeter (ECAL)*, a lead/proportional chamber-sandwich with a depth of 22 radiation lengths (X_0). This provides information about the energy of neutral and charged particles (mainly electrons and photons). A high granularity (73 728 projective towers, divided into three depth zones) of $\Delta\phi = \Delta\theta \approx 1^\circ$ together with a good energy resolution of $\Delta E/E = 18\%/\sqrt{E/GeV}$ allows particle identification and reconstruction of π^0 s. The detectors described so far are located within the *Superconducting Coil* which has an inner radius of 248 cm, an outer radius of 265 cm and a length of 633 cm. It generates a homogenous magnetic field of 1.5 T, which is shaped by the iron of the *Hadronic Calorimeter (HCAL)*. Consisting of 22 layers of iron (total depth 1.2 m), it measures the energy of strongly interacting particles (mainly pions, protons and neutrons). It is read out in 4608 projective towers. Additional digital information allows one to track penetrating muons. Muons penetrating the HCAL are furthermore detected by *Muon Chambers (MUCH)* covering the whole solid angle with two layers.

The determination of the luminosity has to be very accurate to allow the precision measurement of the cross-section for the processes $e^+e^- \rightarrow Z^0 \rightarrow l\bar{l}$ and $e^+e^- \rightarrow Z^0 \rightarrow q\bar{q}$. This is done with the help of the *Luminosity Monitors*.

The detectors (except for the MVD) are described in more detail in the following sections.

3.2.3 Inner Tracking Chamber (ITC)

The ITC is a cylindrical wire chamber (wires along z) with single hit electronics. The mechanics is described in detail in [40]. The ITC covers an active volume of 2 m length, 12.7 cm inner and 28.5 cm outer radius. It provides information about the (r, ϕ) - (resolution $\approx 100 \mu m$) and z -coordinates (resolution $\approx 3 cm$) of charged tracks. For tracks with $\theta > 14^\circ$ eight hits are determined. The (r, ϕ) coordinate is measured via the drift distance within drift cells. The z information is extracted by measuring the time difference of the signal at the two ends of the wire. The (r, ϕ) information improves the momentum resolution of the TPC. For this application a very precise alignment of the ITC/TPC is needed. A procedure to perform this alignment with cosmic rays is described in appendix C. The ITC serves as important component for the first level trigger (see section 3.2.9) with the help of associated processors.

The 960 sense wires (gold-plated tungsten, 30 μm diameter) are strung between the aluminum endplates in z -direction in 8 concentric layers, 96 per layer in the inner 4 layers, 144 in the outer 4 layers. They sit in the middle of the hexagonal drift cells, which are built up with the additional 3840 field wires (gold-plated tungsten, 147 μm diameter) as shown in figure 3.3. The smallest drift cells are in layer 5 with a maximal drift distance of 4.7 mm, while the largest can be found in layer 4 with 6.5 mm drift distance. As the ITC is used as a triggering device, the drift distance has to be kept as short as possible to guarantee fast information. The sense wires are kept at a positive potential of 1.8–2.5 kV,

the field wires are at ground potential. One of the field wires per cell is insulated from the endplate to allow a calibration pulse to be put onto this wire (see figure 3.3). The drift cells in contiguous layers are shifted by half a cell width to allow a good two track separation. Each two layers (double layers) are separated from the others by a layer of guard wires.

The resolution of a single coordinate in the ITC is between 100 and 180 μm . The improvement of the momentum resolution of the TPC alone (see equation 3.3) leads to a combined resolution of

$$\left(\frac{\Delta p}{P^2}\right)_{\text{TPC and ITC}} = 0.8 \times 10^{-3} (\text{GeV}/c)^{-1}. \quad (3.1)$$

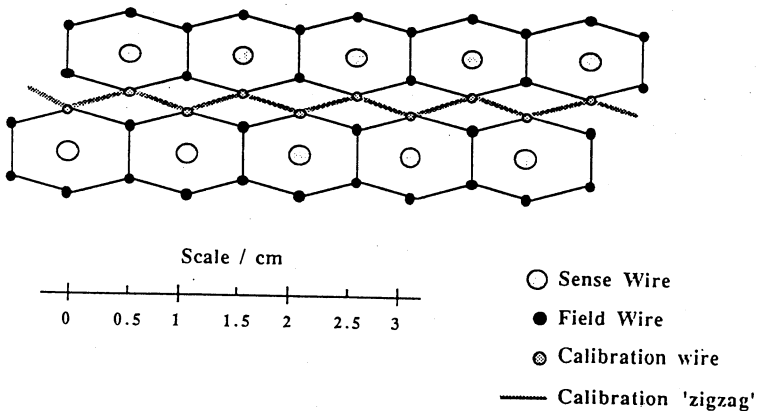


Figure 3.3: An ITC drift cell.

The ITC is operated with a mixture of either $Ar + C_2H_6$ (50:50) or $Ar + CO_2$ (80:20) at atmospheric pressure. The operating voltage lies between 1.9 and 2.4 kV. The gas gain is roughly 5×10^4 , which results in an efficiency of $\epsilon_{hit} > 98\%$ for a track crossing a single layer of the ITC.

Trigger signals for the first level trigger of ALEPH are provided by (r, ϕ, z) space-point processors, which get their signals from processors searching for tracks in radial patterns of wire cells in the (r, ϕ) projection and from the signal for the z coordinate.

3.2.4 Time Projection Chamber (TPC)

The TPC is a large three-dimensional imaging drift chamber. The active volume covered is 440 cm in z with a radial range from 30 cm to 180 cm. The three-dimensional reconstruction of tracks allow a precise determination of single tracks within e.g. a hadronic jet. This includes both the absolute value and the direction of the momentum. Furthermore dE/dx is measured for particle identification purposes.

The TPC has no wires in the active volume. Instead, the ionization along the track is drifted by an (anti)parallel electric and magnetic field to the endcaps. Those consist of the drift chambers measuring the ionization on wires (strung tangentially) and the induced pulse on pads laying behind the wires. The latter allows the measurement of the (r, ϕ) coordinates of the track. The time of arrival of those pulses gives information about the z coordinate, provided the drift velocity is known. Typical drift velocities of $5 \text{ cm}/\mu\text{s}$ lead to drift times of the order of $50 \mu\text{s}$. These long drift times—compared to conventional drift chambers—do not matter at LEP, because of beam crossing intervals of $\approx 22.5 \mu\text{s}$. So, only one beam crossing is missed after a successful readout of a triggered event.

For tracks with $\theta > 40^\circ$, 21 coordinates are measured. The resolution of a single coordinate is $\approx 160 \mu\text{m}$ in (r, ϕ) and $\approx 1 - 2 \text{ mm}$ in z . A sagitta error of $100 \mu\text{m}$ for the most energetic tracks expected at LEP II (100 GeV) results in a momentum resolution of 10% assuming a lever arm of 1.4 m and a magnetic field of 1.5 T .

Before explaining some details of the TPC, the drift process of the electrons is considered in the next section.

Drift Process

Electron-ion pairs are generated when charged tracks pass through a mixture of 91% argon and 9% methan gas. Two quantities are important to describe the characteristic motion of the drifting electrons (ions will not be considered as their drift velocity is 100–1000 times smaller than the electron drift velocity [41]): The *cross-section* in argon gas and the *cyclotron frequency* $\omega = eB/m_e c$ of the electrons. The first one describes the probability of electrons to interact with the gas atoms: the lower the cross-section the higher the average drift velocities of the electrons. Higher drift velocities are demanded, because they result in shorter drift times, and thus smaller dead times of the detector. A minimal cross-section can be achieved by choosing the electric field in such a way, that the electron energy is close to the *Ramsauer* minimum of the gas. This is the case for roughly 115 V cm^{-1} for the TPC [42]. An additional magnetic field pointing in the same direction as the electrical field reduces the transverse diffusion by a factor $1/\omega\tau$, where τ is the mean time between two interactions of the electrons with the gas. The drift velocity is described by the *Langevin* equation [41]:

$$\vec{v}_D = \frac{\mu}{1 + (\omega\tau)^2} \left\{ \vec{E} + \omega\tau \vec{E} \times \vec{b} + (\omega\tau)^2 (\vec{E} \cdot \vec{b}) \vec{b} \right\}, \quad (3.2)$$

where \vec{b} is the direction of the magnetic field and $\mu = e\tau/m_e$ the mobility of the electrons. For the TPC a value of $\omega\tau = 8.9 \pm 0.3$ has been measured [39]. This means that the direction of the drift velocity is determined by the magnetic field. It is better to have such a situation since the homogeneity of the magnetic field is well-controlled and one is free of space charge effects.

The drift velocity has been measured very precisely [39] with the laser calibration system (see section 3.2.4) to be

$$v_D = 5.238 \pm 0.005 \text{ cm}/\mu\text{s}.$$

As the direction of the drift velocity is determined mainly by the magnetic field, distortions of it are very important. The resulting radial displacements have been measured [43] and parameterized. They result in radial shifts of the order of $\Delta r \approx 0.2 \text{ cm}$.

More important for the momentum resolution is the distortion in $\Delta\phi$. Inhomogeneities of the electric field near the endcaps seem to be responsible for the main contribution to a systematic sagitta error. Using a laser calibration system (see below) those effects can be measured and the momentum can be corrected.

Any non zero angle between the magnetic and electric field causes the second term in equation (3.2) to be different from zero, resulting in finite transverse components of the drift velocity. This clearly distorts the radial and azimuthal coordinates. The average components can be measured using the alignment procedure of ITC and TPC [44]. A detailed description of this procedure can be found in appendix C. The resulting relative transverse components are

$$\frac{v_D^x}{v_D} = (-440 \pm 40) \times 10^{-6}$$

$$\frac{v_D^y}{v_D} = (+340 \pm 90) \times 10^{-6}.$$

If the electric field defines the z direction this corresponds to an angle of 0.03° between the axis of magnetic and electric field in ALEPH.

Design and Operation

The TPC consists of two cylinders (the inner and outer field cage), two endcaps and a high voltage membrane (see figure 3.4). The central membrane is made from $25 \mu\text{m}$ thick Mylar coated on both sides with a conducting graphite paint. The inner field cage has a radius of 60 cm , the outer field cage 360 cm and both are 440 cm long. The electric field is defined by the high voltage membrane at -27 kV , the endcaps with the drift chambers at ground potential and the field cages with potential strips. They ensure a homogenous electric field of the size of roughly 115 V cm^{-1} . The gas in the TPC volume is Argon with 9% Methane at atmospheric pressure. The mixing ratio is kept as constant as possible ($\approx \pm 0.03\%$ Methane per week) by premixing a large volume of 900 m^3 gas into a buffer. The contamination with electronegative impurities such as O_2 and H_2O is kept at the level of $\approx 5 \text{ ppm}$ to ensure a signal loss of less than 1.5% per metre of drift [45].

As the electric field points from the endcaps to the membrane (and thus changes sign crossing the membrane), the electrons from the ionization of a charged track drift to the endcaps. The magnetic field of 1.5 T along the z -axis reduces the transverse diffusion. The electrons are then measured in 36 sectors (18 per endcap). Those sectors have a 'zigzag' geometry ensuring a minimum loss of lever arm for tracks crossing the boundaries of the sectors (see figure 3.5). The electrons cross three layers of wires in the sectors (see figure 3.6): First the gating grid, then the cathode plane and finally the sense-wire plane, in which they are measured via the gas amplification. The gating grid can be in an 'open' state ($V_{gate} = -67 \text{ V}$) not disturbing any electron movement. By putting alternately $\pm 40 \text{ V}$ on adjacent wires the ions from the avalanches at the sense-wires cannot drift into

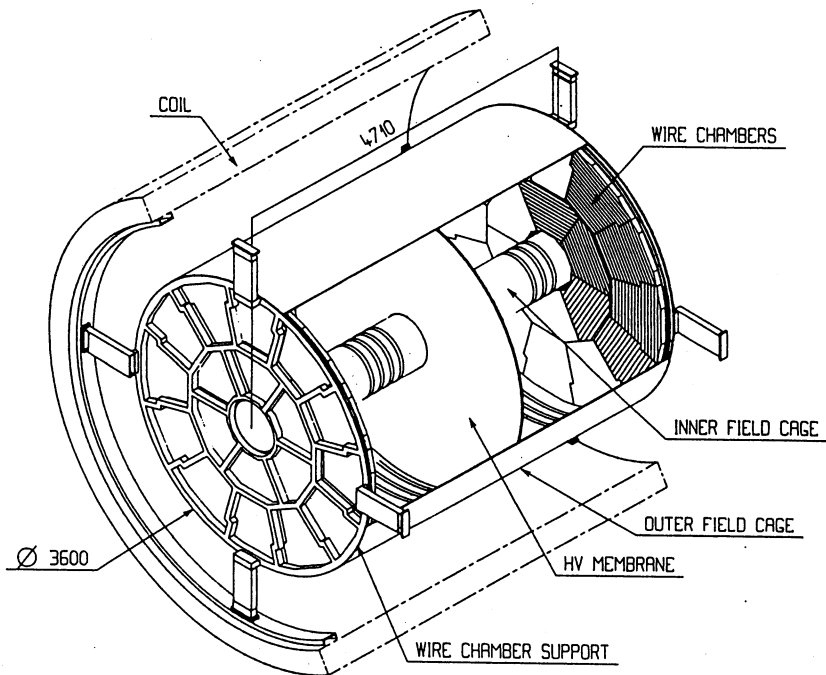


Figure 3.4: *The TPC.*

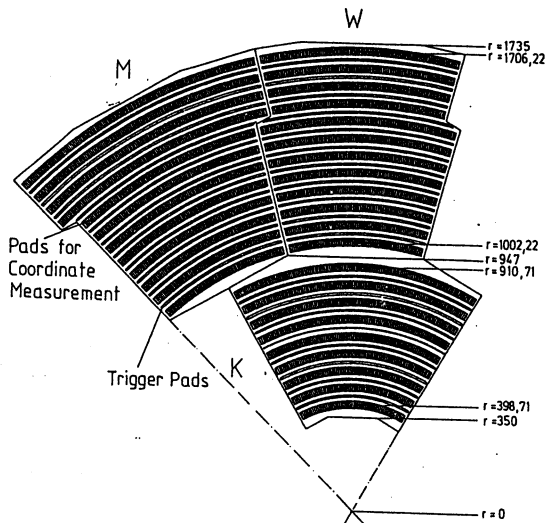


Figure 3.5: *Three different TPC sectors.*

the gas volume ('closed' state). This has to be avoided because any drifting ions in the gas volume can distort the homogenous electric field. Roughly $3\ \mu\text{s}$ before the bunch crossing the gate is opened to allow electrons to drift into the amplification region. A negative decision of the first level trigger closes the gate again. Otherwise the gate is closed after the drift time of $45\ \mu\text{s}$. The cathode-plane defines zero potential for the drift chamber.

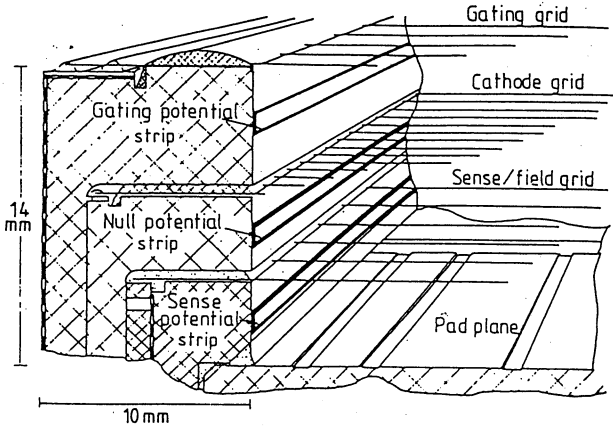


Figure 3.6: *The wire planes in the sectors.*

The sense-wire plane consists of alternately field- and sense-wires. They are strung in the ϕ direction. The mechanical tolerances ensure that individual gas gains do not change by more than 1%. The ionization from the avalanches at the sense-wires induces a signal in the cathode pads, $0.4\ \text{cm}$ apart. Those pads are $0.3\ \text{cm}$ long in radial and $0.62\ \text{cm}$ long in azimuthal direction, so that 7–8 sense-wires lay across one pad. The pads form 21 concentric circles around the z -axis (called the 'pad rows'). Usually 3 pads in a pad row give signals for one charged track coordinate. Using the known response function of the pads, the crossing point with the pad row is reconstructed with a statistical precision of roughly $160\ \mu\text{m}$. This precision clearly depends on the so called "pad crossing angle"—the angle between the track and the radial direction (best for zero pad crossing angle). The time of arrival gives a measurement of the z coordinate. The readout of the time is done in 512 time buckets. This number and the precision of the drift velocity gives a resolution of $1 - 2\ \text{mm}$ in z .

Between the pad rows there are long circular 'trigger' pads which are used for the second-level trigger (fast information about tracks in the TPC). They subtend 15° in azimuthal and $0.63\ \text{cm}$ in radial direction.

One track typically crosses 280 wires. This allows a dE/dx measurement with a resolution of roughly 4.6% for electrons in hadronic events. dE/dx is especially useful for particle identification in the low momentum range. In [46] the electron identification using dE/dx and ECAL (see section 3.2.5) has a hadron misidentification probability of

$\leq 0.25\%$ in the energy range between 2 GeV and 21 GeV . Typically 50 wire hits along a track are required for a dE/dx measurement.

Electronic Readout

Roughly 50 000 channels have to be read out. This is done by a FASTBUS system. For each of the 36 sectors one independent crate cluster is used. The components of one endcap are put together in one system crate. Those two system crates are controlled by the main crate which passes the relevant information to the ALEPH readout. The preamplifiers which are mounted on the sectors pass the signal from pads and wires via twisted pair cable to the Time Projection Digitizers (TPD). They consist of 64 channels of flash ADC (analog-to-digital converter), which digitize the signal with a rate of 11.4 MHz . The correct reference voltages of those FADC's ensure the important intercalibration of different wires/pads. These reference voltages are obtained using 'electronic calibration', which consists of the pulsing of the field wires with subsequent readout of pads and wires.

The Time Projection Processors (TPP) control several FASTBUS crates with TPDs. They do the readout, data formatting, reduction of wire data, monitoring of data and data transfer, error recording and error recovery, calibration and testing of the TPC electronics. Their data flow is transferred to an Event Builder (EB), one for each endcap. A third EB collects data from those two. The tasks of the EBs are similar to the ones of the TPDs; they monitor the data evaluation as well.

Laser System for Field Calibration

To guarantee the desired performance of the TPC one has to be able to monitor it. This is done by a laser calibration system, which provides information about distortions of tracks and allows a precise drift velocity measurement. For this purpose 30 ultraviolet (UV) laser beams are available in the TPC at fixed positions. Each of them points to the interaction point.

Two Nd-yag lasers ($\lambda = 266\text{ nm}$, energy of 4 mJ per 5 ns pulse) sitting at the top of the detector serve pulsed laser beams, which are fed via a 10 m long high precision optical system to the two endcaps (see figure 3.7). A splitter ring is mounted onto each endcap. It splits the beam into three beams of equal intensities. These beams enter the TPC at the three azimuthal positions $\phi = 90^\circ, 210^\circ$ and 330° parallel to the z axis and along the inner field cage. Each of those beams passes through five semitransparent mirrors generating five laser tracks at the polar angles $\theta = 18^\circ, 30^\circ, 39^\circ, 67^\circ$ and 90° in the TPC volume. These laser tracks ionize the gas via a two-photon process. For this process [47] very tiny contaminations in the gas are sufficient. The ionization coming from those laser tracks behaves exactly like the ionization of a charged track of infinite momentum. Hence, the TPC can be read out and the laser track can be reconstructed.

The differences in the different polar angles of the laser tracks are known to 0.02° . This is important, because the drift velocity is measured from the reconstructed polar angles. Any deviation of the reconstructed tracks from straight lines hint to problems with field inhomogeneities. Measurements can be taken for different magnetic field polarizations (and without any magnetic field), so that the deviations can be parametrized as a function of the azimuthal and polar angle. They provide a correction for the field distortions.

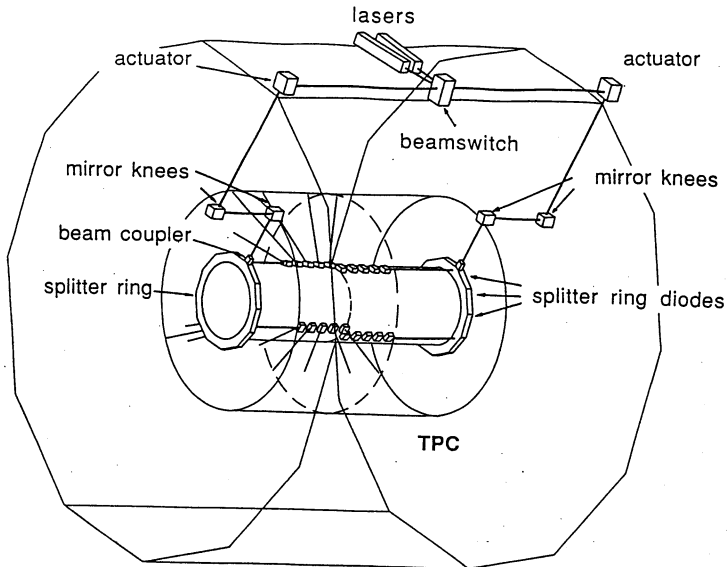


Figure 3.7: *The laser calibration system.*

Performance

The spatial resolution in the (r, ϕ) plane varies from $160 \mu\text{m}$ at 0° pad crossing angle and $400 \mu\text{m}$ for 10° pad crossing angle. The z resolution (measured with the pads) varies from 0.7 mm at $\theta = 0^\circ$ to 2.3 mm at $\theta = 20^\circ$. The mean momentum resolution without ITC is given by

$$\left(\frac{\Delta p}{p} \right)_{\text{TPC only}} = 1.2 \times 10^{-3} (\text{GeV}/c)^{-1}. \quad (3.3)$$

The dE/dx resolution is 4.3% for 280 wires degrading to 9.3% for 50 wires.

3.2.5 Electromagnetic Calorimeter (ECAL)

The TPC is surrounded by the electromagnetic calorimeter (ECAL), a lead/wire-chamber sampling device of about 140 tons and having a thickness of 22 radiation lengths (X_0). It is divided into a barrel and two endcap parts and is operated within the solenoidal magnetic field (see figure 3.8). The barrel and each endcap consists of 12 modules, each covering 30° of the azimuthal range. The endcap modules are rotated by 15° to avoid cracks at the same azimuthal position. The barrel modules sit radially between the TPC (outer

radius of 180 cm) and the superconducting coil (inner radius of 248 cm). Each module is a sandwich of 45 lead/proportional wire-chambers layers. The wire-chambers allow readout of the wires and the cathode pads of the size of approximately $30 \times 30 \text{ mm}^2$. These pads are grouped in projective towers pointing to the vertex. The face covered by a single tower corresponds to an azimuthal range of $\Delta\phi = 0.94^\circ$ and a polar angle range of $\Delta\theta = 0.93^\circ \times \sin\theta$ for the barrel. The towers are divided into three depth-zones (called "stacks"), which are read out separately and have depths of 4, 9 and 9 radiation lengths, respectively. This segmentation in depth gives information about the transverse shower development allowing separation between pions and electrons. Additionally the wires in each of the 45 planes are summed together per module. Therefore the number of electronic channels for pads and wires are quite different: 12 288 pad channels ($3 \times 4 096$ towers) and only 45 wire channels have to be read out in each module. The wire information is especially useful for leptonic events with very low multiplicity, because its energy information is more accurate than that from the pads and the longitudinal granularity is much higher.

Altogether 221 184 stacks (three times 73 728 towers) and 1 620 wire-channels have to be read out. The ECAL provides an energy resolution of

$$\frac{\Delta E}{E} = \frac{18\%}{\sqrt{E/\text{GeV}}}. \quad (3.4)$$

The ECAL is operated with a mixture of 80% Xe and 20% CO_2 . The relative amount of Xe is kept constant within $\pm 1\%$. The pressure is 60 mbar above atmospheric pressure. It is monitored together with the temperature. Furthermore a small single-wire chamber with a ^{55}Fe source is contained in each module. They monitor the gas gain.

For the trigger decision the wire-planes with odd and even numbers are summed up per module.

3.2.6 Magnet and Superconducting Coil

The superconducting coil, which surrounds the whole ECAL, creates a magnetic field of 1.5 T. The steel in the hadronic calorimeter (see section 3.2.7) serves as the flux return yoke. The solenoid has an inner radius of 496 cm and an outer radius of 633 cm. The useful magnetic volume is 123 m^3 , the stored magnetic energy $130 \times 10^6 \text{ J}$. The requirements of the TPC to have a sagitta distortion less than 0.2 mm leads to the condition that the integral over the relative radial component of the magnetic field is below 2 mm:

$$\int_{0 \text{ mm}}^{2200 \text{ mm}} \frac{B_r}{B_z} dz < 2 \text{ mm}. \quad (3.5)$$

Besides the main solenoid, made of a continuous and homogenous winding extending over the whole length of 635 cm, two compensating coils are located at the ends of the main solenoid. Each of them is 40 cm long.

3.2.7 Hadronic Calorimeter (HCAL) and Muon Chambers

A large iron structure with a total weight of roughly 2 600 tons serves as main support for the whole apparatus and as Hadronic Calorimeter (HCAL). It is divided into a barrel

part and two endcaps. The first one is built out of 12 modules, each of the latter consists of 6 petals (see figure 3.8). The overlap region can be seen in figure 3.9.

Each module in the *barrel* is 7.24 m long and is split into two half modules, which are mirror images of each other. These modules are made out of 22 iron slabs, each 5 cm thick, plus an outer slab of 10 cm. Spacers at the edges are used to maintain a gap of 2.2 cm. The total thickness is 1.2 m, corresponding to 7.2 hadronic interaction lengths.

The petals of the *endcaps* have at the narrow end 22 slabs of iron, 5 cm thick, plus a 10 cm slab on the outside. To fit to the barrel part, the number of slabs at the broad end is reduced to 16 slabs. Here altogether four rods per slab, spread over the whole petal, are needed to keep the distance of 2.2 cm per gap considering the large magnetic forces.

The instrumentation of the iron is done with limited streamer tubes. They are operated at slightly higher voltage than proportional chambers. Therefore a charged particle produces a local avalanche on the central wire which is independent of the amount of primary ionization in the chamber. Each gap contains one layer of tubes, plus an additional one in front of the iron. These tubes are made out of extruded plastic (PVC), where eight cells of inner size $0.9 \times 0.9 \text{ cm}^2$ form one tube. In the barrel they have a length of roughly 7 m. The inner surfaces are painted with graphite, while a wire is strung in the middle, held in position by spacers located every 0.5 m. The operating gas is an Ar, CO₂, isobutane mixture in the proportions 13%, 57%, 30%, respectively. The operating voltage is 4250 V. The side of the eight-cell units facing the outside of the apparatus is read out via copper pads outside the tubes (analog readout). They are summed up to form projective towers. On the side facing the inside of the apparatus aluminum strips, one per cell, are positioned parallel to the wires. They are used to derive digital information, which gives a two-dimensional picture of a hadronic shower and is especially useful for π/μ separation (digital readout).

Clearly the geometry of the instrumentation in the barrel and endcaps is quite different: the towers in the *barrel* subtend an azimuthal angle of 3.7°, while the polar angle is kept constant by varying the length of the pads proportional to $1/\{\cos^2(90^\circ - \theta)\}$. Of 3456 towers in the barrel 768 are in the overlap region between barrel and endcap. The eight-cell units are placed in the iron in such a way, that no muon can penetrate the module without being detected in the tubes². The polar angle subtended by the towers in the *endcaps* is sustained throughout the petal. The azimuthal angle covered by one tower increases as one goes to the narrow end of the petal: it doubles from 3.7° to 7.5° at $\theta = 34^\circ$ and from 7.5° to 15° at $\theta = 18^\circ$. At the narrow end 22 layers of tubes can be found while the broad end contains only 15. Together both endcaps have 2100 towers of which 768 are shared with the barrel. The orientation of the tubes is horizontal in those four petals which have one horizontal edge. In the other two the orientation is inclined by 60° w.r.t. the horizontal.

The muon chambers (MUCH) consist of two double layers of streamer tubes following the layout of the HCAL in the barrel and the endcap. Further middle-angle chambers placed over the outer edges of the petals cover the overlap region. The cracks of the MUCH corresponds to the cracks of the HCAL in the barrel.

The gas system supplying HCAL and MUCH exchanges the total gas volume of 54 m³ every two to three days. The relative flow rates are monitored to an accuracy of $\pm 1\%$ full

²This might happen due to the trapezoidal cross-section of the modules.

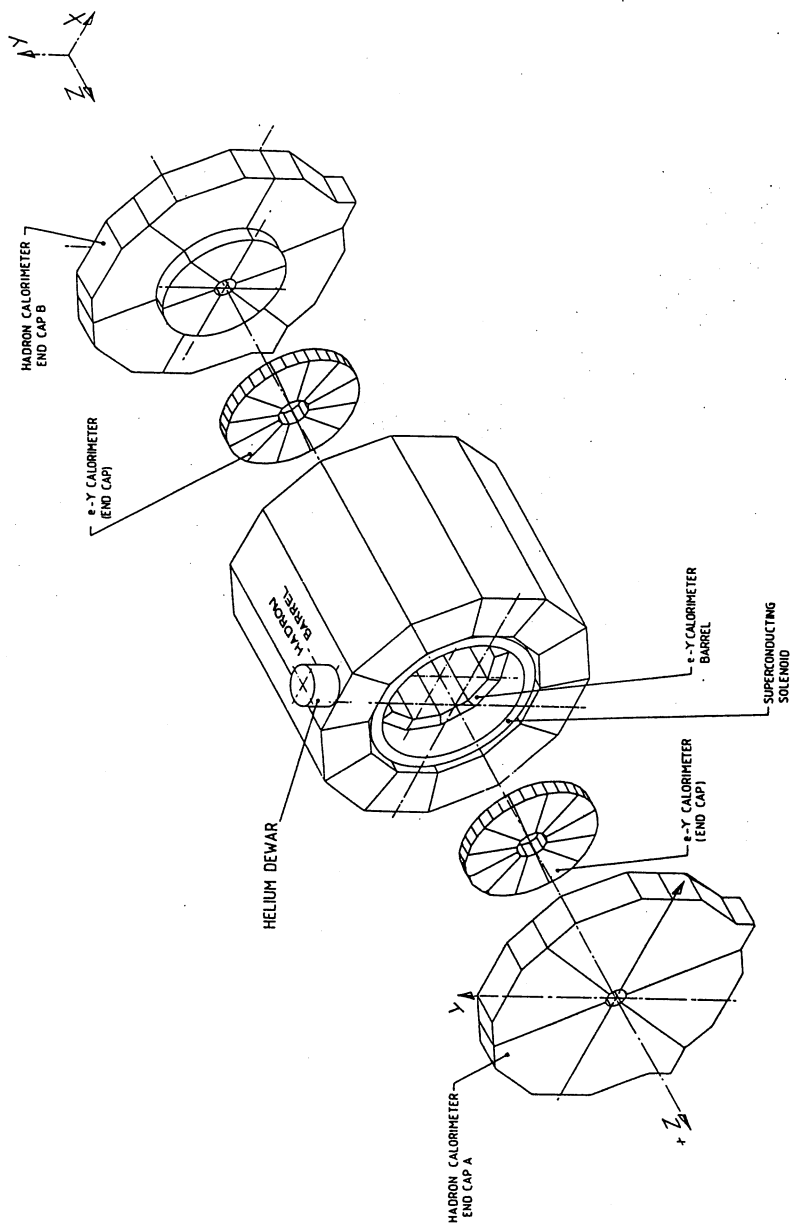


Figure 3.8: The hadronic and the electromagnetic calorimeter.

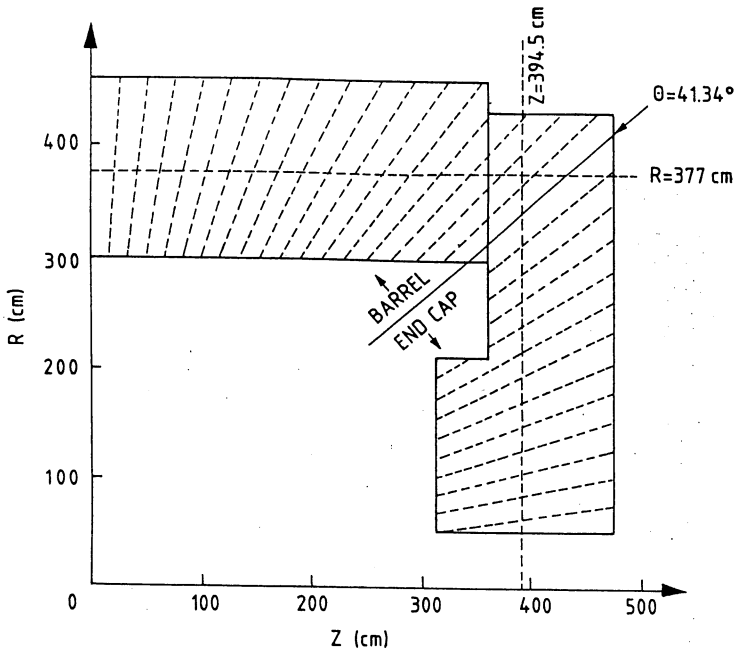


Figure 3.9: The overlap region for the HCAL calorimeter.

scale. The charge per streamer should not fluctuate by more than 4%.

For the trigger the signals from the wires are summed up in double layers.

Concerning the *analog signals*, the ratio of visible energy for electrons to pions has been measured to 1.33 ± 0.04 with test beams. The *digital signals* allow a muon identification efficiency of $(91.5 \pm 0.8)\%$ with a contamination of $(1.1 \pm 0.3)\%$ from pions as shown in section 4.1.7. This number is valid for leptonic events and muons of energies greater than 3 GeV, thus penetrating the HCAL.

3.2.8 Luminosity Monitors

The knowledge of the luminosity is not necessary for this analysis. Therefore the devices for the luminosity measurement shall be described very briefly for completeness. They are used to determine the rate of Bhabha events with a high precision to measure the luminosity via the cross-section, which is given by

$$\frac{d\sigma}{d\Omega} = \frac{4\alpha^2}{E^2} \frac{1}{\theta^4} \quad (3.6)$$

in lowest order of α , where E is the beam energy. The cross-section peaks very strongly in the forward direction. Therefore it is necessary to place the detectors as close as possible and as accurate as possible to the beam pipe. They have to give precise information about the energy and the direction of electrons and positrons. In ALEPH these measurements

are done with the luminosity calorimeter (LCAL) and the Small Angle Tracking Device (SATR). Two combinations of a tracker and a calorimeter are situated at $z = \pm 2.7 m$. The tracking device accepts electrons or positrons with polar angles between 40 and 90 *mr*ad, the calorimeter those between 45 and 155 *mr*ad.

These devices allow the determination of the luminosity with a systematical error of 0.7% [18].

3.2.9 Trigger System

The trigger system of ALEPH is designed to accept all possible e^+e^- interactions, without looking for a specific type of event. Its main purpose is to reduce background and keep the event rate at a frequency small enough to avoid significant dead-times. Background events are mainly beam-related tracks (beam-collimator interactions), beam-gas interactions, cosmic, off-momentum electrons and electronic noise. Special emphasis has been put on the flexibility of the system which is needed for varying background conditions. They depend mainly on the performance of LEP and may change from fill to fill. The whole trigger is split into three levels according to the decision time:

- The *Level-1 Trigger* takes a decision within 5 μs (compared to 22 μs between beam crossings) and starts the event digitization. The rate must be below a few hundred Hertz to keep space-charge effects small in the TPC. The decision is based on signals from ITC, ECAL and HCAL (for the latter information from pads and wires). The signal sources are grouped into 60 logical trigger segments in θ and ϕ for the calorimeters and in ϕ only for the ITC. This segmentation follows closely the structure of the calorimeters. The signals themselves are sent to four discriminators with remotely adjustable thresholds, so that four YES/NO decision are available per segment. Based on these decisions up to 32 specific physics triggers can be defined. Those relevant for this thesis will be discussed later (see section 4.1.9).
- The *Level-2 Trigger* uses fast tracking information from the TPC to take further decisions about the quality of the event within 50 μs . It checks the presence of charged tracks originating from the vertex using hard-wired processors which look for tracks in the (r, z) plane. This procedure is appropriate for tracks above 1 *GeV/c*. If the level-1 decision is not confirmed the readout process is stopped and cleared. The drift time in the TPC and the clearing time of ECAL sum up to 61 μs . As the next available (third) bunch crossing at 67 μs after the level-1 trigger shall not be lost, the decision of the level-2 trigger is broadcast to all parts of the detector within 6 μs after the end of the TPC drift time. The rate of this level should not exceed 10 *Hz*.
- The *Level-3 Trigger* is applied after readout and is performed by an analysis process running within the data acquisition. The purpose is to keep the amount of data to be written to storage media as small as

possible. This is done with several independent computers. The level-3 trigger has not been used for the 1989 data.

Excellent running conditions of LEP have led to level-1 trigger rates of the order of 0.5Hz for luminosities of $10^{30}\text{cm}^{-2}\text{s}^{-1}$ and deadtimes of $1.5 - 2.5\%$.

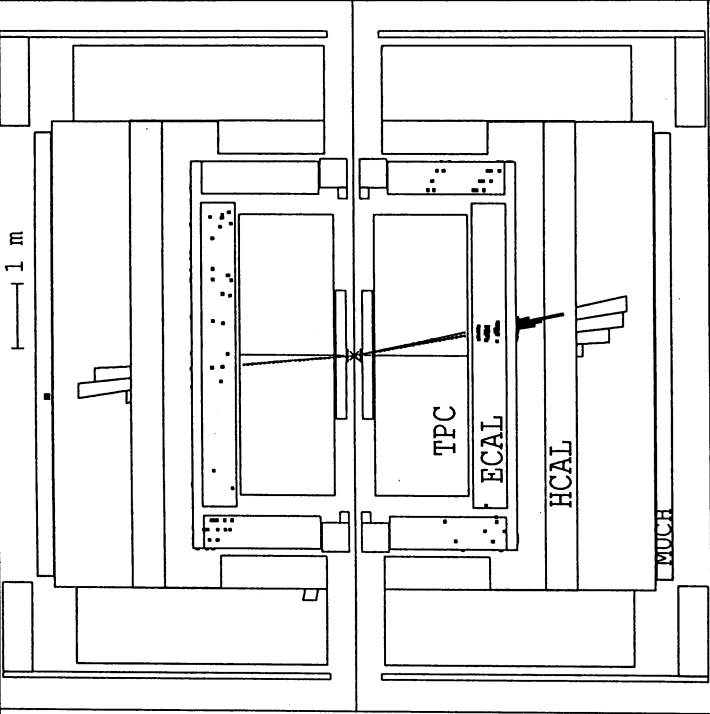
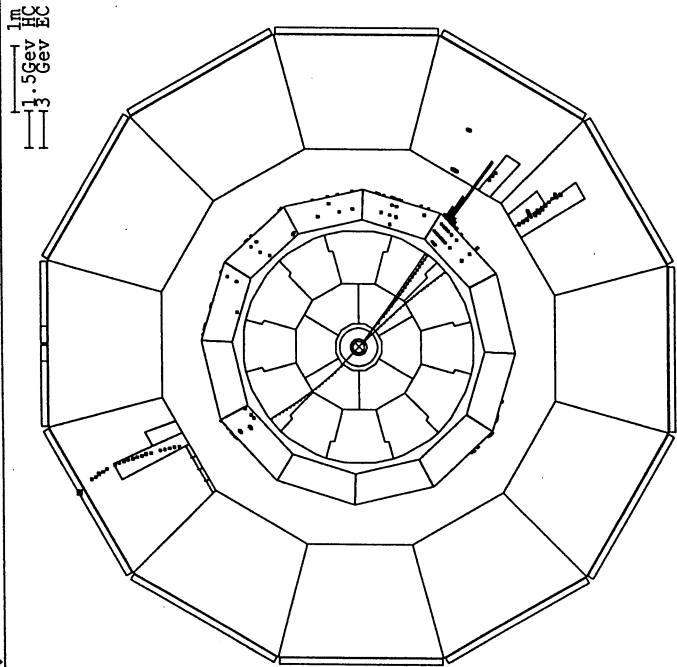
3.2.10 Data Acquisition and Reconstruction

The electronics of the different subdetectors is read out via a flexible tree-like structure with a strong hierarchy. The readout is started by the level-1 trigger, which uses sums of analog information. After a positive decision one has to wait for the drift of the electrons in the TPC to be finished. A positive level-2 decision leads to a transfer of the trigger mask and the event number to the ReadOut Controllers (ROC) by the Main Trigger Supervisor. The Event Builders (EB) build up subevents at the level of each subdetector and do formatting if needed. These subevents are collected and put together to a complete event in the Main Event Builder (MEB). After the transfer to the main computer, the data can be used by several processes for different tasks as monitoring or writing to disk. They are controlled by the Run-Controller. The events are reconstructed 'quasi-online' by a farm of workstations (FALCON) using the reconstruction program JULIA. The raw data are transformed to the Production Output Tapes (POT), which contain physical information like energy, momentum or coordinates. Those POTS are later compressed to the Data Summary Tapes (DST), which are used for the analysis in this thesis.

The structure in time of data taking is given naturally by different fills of LEP. A finer structure is needed for the detector, taking into account problems or varying conditions. Therefore the data are taken in 'runs', which are continuous periods of data taking. Therefore a run number and an event number are sufficient to mark an event unambiguously.

A $\tau^+\tau^-$ event ($\tau \rightarrow \mu\nu\nu$ and $\tau \rightarrow 3\pi$) is shown in figure 3.10 displayed with the ALEPH drawing program DALI ("Display of Aleph Interactions").

Figure 3.10: *Next page: A $\tau^+\tau^-$ event in the ALEPH detector displayed with DALI. One τ decays into a muon (see signal in HCAL) and two neutrinos, the other decays into three charged pions and a neutrino. On the left hand side the x - y projection is shown. To enhance the resolution of the three prong decay in the TPC the detector is shown in a non-linear scale. On the right hand side the same event in the r - z projection in a linear scale is shown.*



4. Data Selection

The aim of the selection is to get the maximum number of $\tau \rightarrow \mu\nu\nu$ decays with a minimum number of background events. Starting on the DST (see section 3.2.10) in this chapter the selection criteria used for this purpose are explained and their effects are studied. As described in detail in section 2.5.2 both the momentum and the angular information of the muon are needed for the measurement of the various production and decay parameters. Therefore effects which affect the slope of the momentum or the angular distribution must be taken into account properly, while the absolute efficiency does not change the result.

To take momentum and angular effects of the detector into account it is divided into different angular regions. This is necessary as the performance of the apparatus is not totally homogeneous what concerns the efficiency, the resolution and the background contamination. Within these angular regions the momentum spectrum is measured, the corrections are determined and the background is subtracted independently from the others. The hadronic calorimeter (HCAL) is used to identify muons; for the particular choice of the detector regions it is therefore reasonable to follow its geometry. As seen in figure 3.9 a track going through the HCAL can pass five different regions: One of the two endcaps, one of the two overlap regions (crossing barrel and endcap) or the barrel. This is taken to be the angular subdivision for this analysis (see table 4.1 for the detailed binning in momentum and angle). A justification is given by the muon identification efficiency determined in section 4.1.7. For control purpose the analysis is performed for the whole detector as well. The resulting measurement of the polarization from the momentum spectrum only can be directly compared to the results of the ALEPH publication [22].

Detector	Angular Range	Number of momentum bins for $0. \leq x \leq 1.$
ENDCAP A	$0.7 < \cos\theta \leq 0.9$	10
OVERLAP A	$0.6 < \cos\theta \leq 0.7$	5
BARREL	$-0.6 \leq \cos\theta \leq 0.6$	20
OVERLAP B	$-0.7 \leq \cos\theta < -0.6$	5
ENDCAP B	$-0.9 \leq \cos\theta < -0.7$	10

Table 4.1: *Angular and momentum bins in the analysis.*

4.1 Selection of $\tau \rightarrow \mu\nu\nu$ Events

The events which have been reconstructed by the program JULIA are classified at the end of this process. This is done to allow different physicists to study different final states without being forced to go through all the data. The main classification is made by looking at the number of charged tracks in the event which provides a good discrimination between hadronic ($q\bar{q}$) and leptonic (e^+e^- , $\mu^+\mu^-$, $\tau^+\tau^-$) final states. Clearly events from the latter class are used as starting point for this analysis. The detailed definition of those so called “CLASS 15 events” can be found in appendix B.1. All cuts made for this classification are reinforced by the cuts explained in this section.

For the selection of $\tau \rightarrow \mu\nu\nu$ events one could in principle select τ events first, before identifying the actual τ decay. Looking at all processes with leptonic final states (e^+e^- , $\mu^+\mu^-$ and $\tau^+\tau^-$) in CLASS 15 this step can be avoided by just identifying single muons excluding a muon in the opposite hemisphere. This has the advantage of smaller systematic uncertainties.

The DST is read by the analysis program ALPHA which allows the processing of all kinds of data (DST, POT, raw data, Monte Carlo, etc.) within ALEPH. It is especially useful for DST and Monte Carlo.

The selection itself is made in a two-step process: First the CLASS 15 events are processed with ALPHA with a first set of cuts. Within this process the remaining events are written in a compressed format keeping only the relevant physical information. In a second step these events are processed and further cuts are imposed.

4.1.1 Monte Carlo Simulation

A crucial check whether a distribution of an observable in the data is understood is the comparison of this distribution with a simulation. This simulation has been done using the $\tau^+\tau^-$ generator KORALZ, version 3. It generates the four-vectors of $\tau^+\tau^-$ events. A description of this generator can be found in [36]; a short summary is in section 2.6.3.

The subsequent simulation of the detector is made by the program GALEPH [48]: The four-vectors describing the particles generated by KORALZ are used by the tracking package GEANT [49] to take into account the interaction with matter and the decay of particles. GALEPH passes all relevant material information to GEANT for this purpose. The interactions with the active parts of the detector are simulated. This includes the simulation of the trigger. Finally the digital information is determined and written in a format which is identical to the one used for data. This Monte Carlo sample is then treated exactly like data: After the reconstruction the same cuts as used for data are applied.

Finally the distributions which have been obtained in this way can be compared to the corresponding distributions in the data. All plots referred to as “Monte Carlo distribution” in this section consist of a simulation of $\tau^+\tau^-$ events. In any other case it is explicitly mentioned which simulated process is shown.

4.1.2 Definition of a Good Track

A track is determined by a set of TPC coordinates which have been clustered by a track finding algorithm (within JULIA). To guarantee a minimum quality this track has to consist of at least 4 hits in the TPC.

Tracks belonging to e^+e^- interactions should point to the vertex of the annihilation. The beam spot has a spatial expansion of $\sigma_x \approx 160 \mu\text{m}$ and $\sigma_y \approx 30 \mu\text{m}$, while the bunch length is about 1.0 cm [50]. The beam position is determined on a run by run basis using all hadronic events in a run.

Every track is described by the following helix parameters:

- the closest distance of approach D_0 of the track to the beam axis in the (r, ϕ) -plane;
- the azimuthal angle ϕ_0 to the x-axis at this point;
- the z coordinate z_0 at this point;
- the cosine of the angle ($\cos\theta$) between the track direction at the closest distance of approach and the beam axis;
- the curvature in the (r, ϕ) -plane or correspondingly the transverse momentum.

For a good track a value of $|D_0| < 2 \text{ cm}$ and $|z_0| < 10 \text{ cm}$ is demanded, while the momentum has to be larger than $0.1 \text{ GeV}/c$. To define a fiducial region, $|\cos\theta|$ must be smaller than 0.95.

So, summarizing the cuts for a good track:

- at least 4 TPC hits;
- momentum greater than $0.1 \text{ GeV}/c$;
- $|z_0| < 10 \text{ cm}$;
- $|D_0| < 2 \text{ cm}$;
- $|\cos\theta| < 0.95$.

4.1.3 Muon Identification

The most important feature to select the decay product of the decay $\tau \rightarrow \mu\nu\nu$ is the ability of the detector to positively identify muons. Due to the hadronic decays of the τ 's the μ/π separation is crucial. A discussion of the identification shall therefore be given before discussing the rest of the cuts. It should be mentioned already here that the muon identification efficiency is measured with data not using any Monte Carlo information. Therefore the Monte Carlo distributions in this section are shown only for illustration. They do not have to agree with the data in detail.

Muons at energies below a few hundred GeV lose energy merely through the ionization process (dE/dx): the weak interaction is too small, while bremsstrahlung is negligible

due to the relatively high mass. This clearly distinguishes muons from other charged particles. The energy loss in lead and iron is $\approx 0.012 \text{ GeV/cm}$. This corresponds to a loss of about 0.14 GeV during the penetration through ECAL and roughly 1.5 GeV after going through the HCAL. Pions on the other hand lose most of their energy due to the strong interaction with matter. This gives a handle to separate muons from pions. For this purpose both ECAL and HCAL can be used in principle. But as the pions usually penetrate the ECAL as well (even though the shower has completely different characteristics), the use of the penetration criteria in the HCAL is more powerful. In addition the shower profile can be used (and again in principle in ECAL and HCAL). But the profile of a minimum ionizing muon in ECAL may be distorted by radiative photons going more or less colinear with the muon. Therefore the muon identification is performed with the HCAL only. This has another advantage: The ECAL as independent detector can be used to positively identify pions. Their behaviour in the HCAL can then be studied.

From the last considerations two calorimetric quantities are outstanding for the identification of muons: The *penetration* and the *shower profile*. Information about the penetration is obtained from the digital signal in the outermost planes of HCAL. The TPC track is extrapolated into HCAL opening a "road" that takes the deflection due to the magnetic field and the multiple scattering into account. To be insensitive to noise in the HCAL the width of the road is taken to be rather narrow:

$$\sigma_{\text{road, Penetration}} = 2 \text{ cm} + 3\sigma_{\text{Multiple Scattering}}. \quad (4.1)$$

The term for the multiple scattering clearly depends on the momentum of the particle. Along this road the digital readout of the HCAL is used to check whether a plane of streamer tubes has fired or not. Dead zones (e.g. cracks between modules) and tubes which are not read out (for geometrical or electronic reasons) are taken into account. This leads to a number of planes expected to fire and a number of planes which have actually fired. As many pions are not fully stopped within ECAL one is more sensitive to the actual penetration of a particle if only the last 10 out of 23 planes are considered. For compactness the number of planes which are expected to fire within the last 10 planes is called $N_{E,10}$ while the number of actually fired planes within the last 10 is called N_{10} from now on.

To study the behaviour of different observables for the μ/π separation samples of clean muons and clean pions are needed. These samples are discussed in detail in section 4.1.7 when determining the efficiency of the muon identification. For the discussion in this section it is enough to say that muons are positively defined by an associated hit in the muon chamber (called "chamber-tag") while the pions are identified by the reconstruction of an associated π^0 in ECAL (this is explained in detail in section 4.2.1).

For a clean muon and pion sample the quantity N_{10} is shown in a logarithmic plot in figure 4.1. Monte Carlo (shaded histogram) does not reproduce the data distribution well. This is due to wrong efficiencies for the single planes in HCAL in the Monte Carlo. As the muon identification is studied only with data not using any Monte Carlo (see section 4.1.7) this discrepancy does not matter at all (the same is true for all other quantities used for the muon identification). A cut value of $N_{10} \geq 4$ is drawn in the picture. Most of the pions are already rejected by this condition. Still, the pion can enter this sample via three different mechanisms: the decay of a pion into a muon and neutrino, the pion sail-

through (a pion loses energy merely by ionization) and the pion punch-through (the hadronic shower of a pion is not completely contained in the calorimeter). The first effect dominates the low momentum region, while sail-through is more or less independent of the momentum and punch-through increases slightly with momentum.

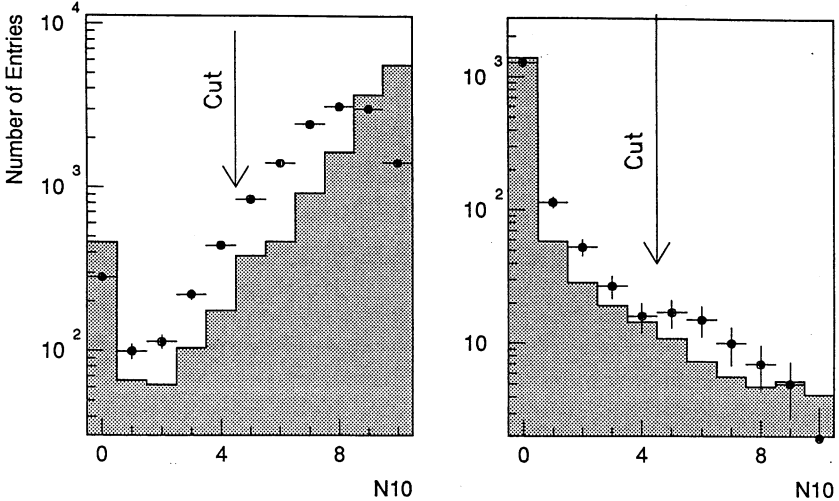


Figure 4.1: Number of fired planes within the last 10 planes for muons (left) and pions (right). The dots with error bars are data, the shaded area is Monte Carlo.

The actual cut on the penetration is slightly different than just $N_{10} \geq 4$. To take regions with restricted acceptance into account ($N_{E,10} < 10$, e.g. cracks), at least 40% of the number of expected planes must have fired. In this case it would be possible to misidentify a large fraction of the pions if they go into a crack (e.g. $N_{E,10} = 1, 2$) and one hit would be enough for the pions to enter the sample. Therefore at least two hits are demanded within the last ten planes not looking at the number of expected planes. Consequently the penetration criteria for a muon is defined by

$$\begin{aligned}
 N_{10} &\geq 2 \quad \text{and} \\
 \frac{N_{10}}{N_{E,10}} &\geq 0.4.
 \end{aligned}
 \tag{4.2}$$

Most of the pions are already rejected by this cut. Further reduction is possible by taking the information about the shower profile into account: Hadronic showers have a much larger transverse width than “showers” of minimum ionizing particles. A quantity which measures the lateral shower width is the mean number of clusters (as given by the HTUB bank) per fired plane in HCAL (called CLPLN). As one is now interested in getting each possible cluster in the HCAL to discriminate against hadrons, the road analysis is repeated with a much wider road of

$$\sigma_{road,CLPPLN} = 50 \text{ cm} + 3\sigma_{Multiple \text{ Scattering}}. \quad (4.3)$$

Furthermore all fired planes (not only the last 10) are taken into account. The corresponding distributions already after the penetration cut for muons and pions are shown in figure 4.2, where the additional discrimination power becomes evident. The resulting cut in CLPPLN is

$$CLPPLN \leq 1.3 \text{ for a track going in the barrel,}$$

$$CLPPLN \leq 1.4 \text{ for a track going in the endcaps } (|\cos\theta| > 0.6). \quad (4.4)$$

It has been chosen different in the barrel and the endcap to minimize the difference in the efficiencies in the barrel and the endcap.

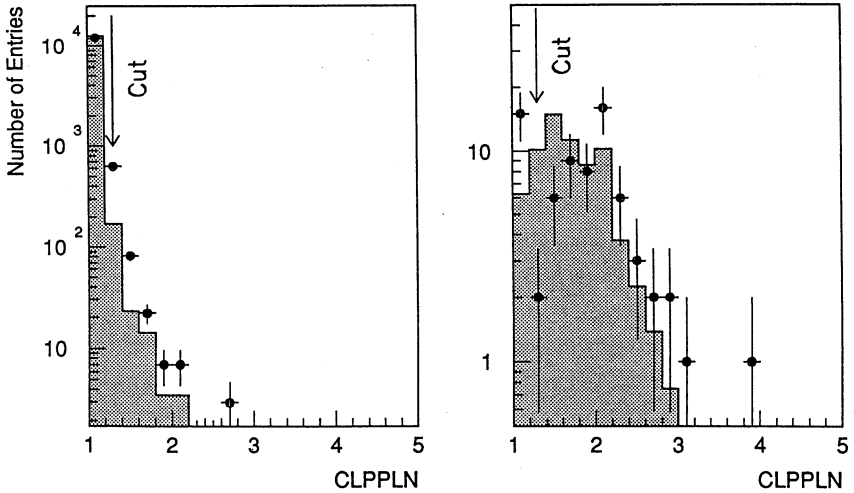


Figure 4.2: Mean number of clusters per fired plane (CLPPLN) for muons (left) and pions (right) after penetration cut. The dots with error bars are data, the shaded area is Monte Carlo.

Already at this stage it is evident that background from $\mu^+\mu^-$ final states can cause problems just due to the large number of this kind of event. It is therefore necessary to ask for the exclusion of a muon on the recoil side of an identified muon. For this purpose a highly efficient muon identification (called μ veto) is defined by demanding

$$\begin{aligned} N_{10} &\geq 1 \text{ for } N_{E,10} = 0 \text{ or} \\ \frac{N_{10}}{N_{E,10}} &\geq 0.2 \text{ for } N_{E,10} > 0. \end{aligned} \quad (4.5)$$

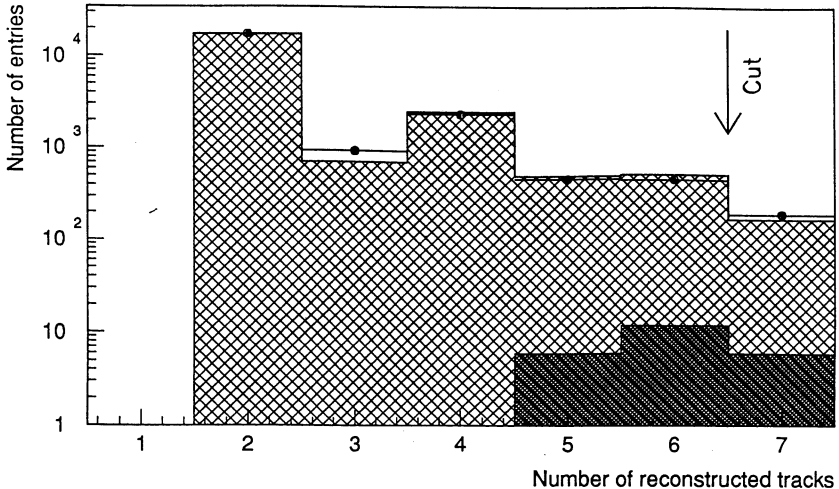


Figure 4.3: Number of good tracks in the TPC after the cuts on the event level. Data are shown as points, the light shaded area is e^+e^- , $\mu^+\mu^-$ and $\tau^+\tau^-$ Monte Carlo. The dark shaded area shows the $q\bar{q}$ Monte Carlo.

4.1.4 Cuts at the Event Level

In this section the different cuts on the basis of a complete $e^+e^- \rightarrow \tau^+\tau^-$ event are explained. The plots shown here are based on the preselected sample (CLASS 15, see appendix B.1). Even though the cuts described here are applied on the whole event, the subdivision into two hemispheres is needed. This is done by calculating the thrust axis and then dividing the event by a plane perpendicular to this axis going through the origin.

- At least two tracks are demanded. To discriminate against the hadronic background not more than six good tracks are allowed in the event. A plot of the number of tracks after all cuts on the event level is shown in figure 4.3. The remaining hadronic background (dark shaded area in figure 4.3) is very small. This plot shows a slight disagreement for the number of tracks equal to 3. Such events are dominated by events like e.g. converted photons where one electron was not seen.
- One background source comes from two-photon events of the type $e^+e^- \rightarrow e^+e^-\mu^+\mu^-$ and $e^+e^- \rightarrow \tau^+\tau^-$. These events can be accepted if the two electrons escape detection because they go into the beam pipe. The typical signature of these events is a rather low total energy. Therefore at least one track with more than 3 GeV is demanded.
- Events with more than four tracks have some probability of being contaminated by $q\bar{q}$ events. Therefore a special cut on the maximum opening angle of a track to the axis of the corresponding jet is applied. The cosine

of this angle has to be larger than 0.85 for events with more than four tracks.

- As the number of electrons passing the muon identification is practically zero, e^+e^- events do not enter the sample. Nevertheless they account for a large fraction of all leptonic events. To suppress them at an early stage, a cut on the total energy deposited in the ECAL is made. Figure 4.4 shows the energy measured by the wires in all planes of all modules in ECAL. At the high end the e^+e^- final states can be found. The low energy region is dominated by the $\mu^+\mu^-$ events. Inbetween the $\tau^+\tau^-$ can be found. The cut is made at 70 GeV reducing the number of Bhabha events substantially. The discrepancy between Monte Carlo and data for electrons shows a problem of the simulation of the energy deposit in ECAL: the saturation is not simulated at all. To minimize the effect of this discrepancy the cut is made far off the peak.
- To further reduce the background from two-photon events a cut on acolinearity is applied. Acolinearity is defined as cosine of the angle between the two jets in the two hemispheres. For Z^0 decays with two leptons/quarks in the final state this quantity is expected to be -1 ("back to back"). This is not the case for two-photon events which are more or less flat in acolinearity. This quantity is shown in figure 4.5 for data and Monte Carlo (for all leptonic final states). The excess in the data are the two-photon events. This plot shows the necessity to take this background into account. The Monte Carlo events above ≈ -0.8 correspond to events with one or more radiated photons in the final state. To reduce the two-photon events with a minimum loss of signal, the acolinearity is demanded to be smaller than -0.95 . It is evident that this cut reduces substantially the background while the signal is affected only very modest.
- An additional cut to suppress the two-photon events is the cut on the electromagnetic energy deposited close to the beam pipe. Figure 4.6 shows the energy which has been deposited in the luminosity calorimeter. Again the two-photon background can be seen as excess of the data over the simulation. The cut is made at 5 GeV .

Figures 4.5 and 4.6 show that the the cuts on acolinearity and the energy deposit in LCAL suppress the two-photon background not loosing much of the signal. However, they are not the main cuts for suppressing this background. Some of the cuts explained in the next section discriminate against this type of background very effectively without being designed for this purpose (e.g. the cut on momentum and muon identification). The remaining number of background events is estimated in section 4.2.3 and is much less than figures 4.5 and 4.6 may suggest.

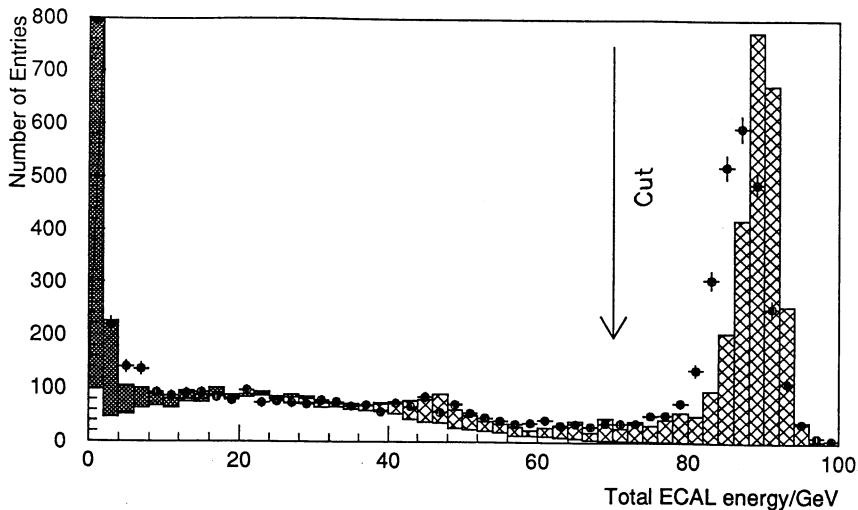


Figure 4.4: Energy deposited in ECAL for leptonic events. The first bin is not drawn to full scale. Data are shown as points with error bars. The simulated $\tau^+\tau^-$ events are displayed as histogram (white), the $\mu^+\mu^-$ events are shown in dark grey at the lower end of the spectrum. The e^+e^- events (higher end of the spectrum) show that the simulation of the ECAL energy is not perfect (saturation is not simulated at all).

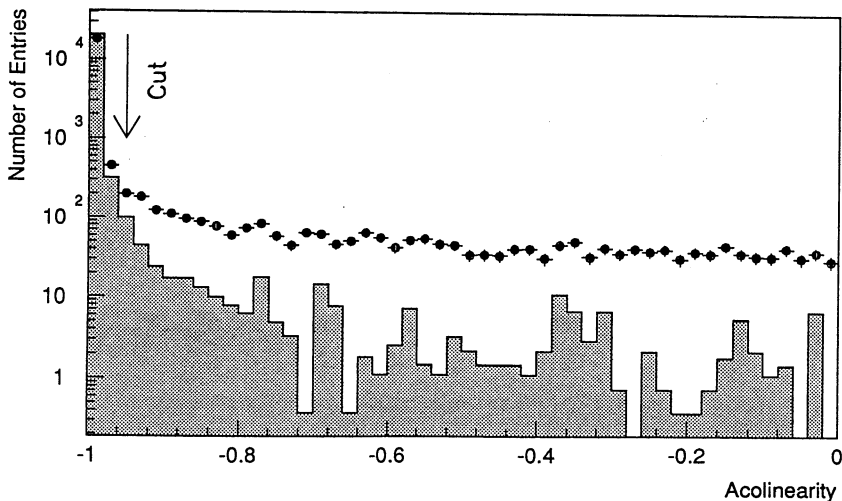


Figure 4.5: Acolinearity for data and Monte Carlo (shaded area; $Z^0 \rightarrow l^+l^- (\gamma)$ decays are simulated).

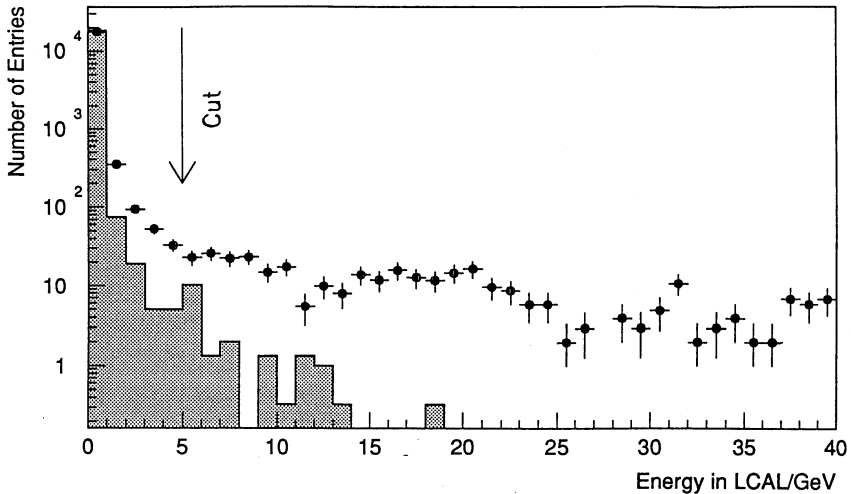


Figure 4.6: Energy deposited in LCAL (after the cut on acolinearity).

4.1.5 Cuts at the Single-Track Level

As already said before, the idea is to positively identify a muon in one hemisphere excluding the possibility of a $\mu^+\mu^-$ event. For this purpose several further cuts have been applied on the basis of the corresponding and opposite hemisphere of that track which is considered as a candidate for a $\tau \rightarrow \mu\nu\nu$ decay. They are described in the following.

- No further good track in the same hemisphere is allowed. This removes the three and five prong decays of the τ . Simultaneously the decays with bremsstrahlung and a subsequent photon conversion are thrown away as well. As they are only a small fraction of all events¹ it is not worth a special effort to save these events for the analysis.
- The normalized momentum $x = \frac{p}{E_{beam}}$ of the track has to be larger than 0.1. The $|\cos\theta|$ has to be smaller than 0.9. This cut is a further restriction of the fiducial volume of the detector (mainly TPC).
- The most important cut is the muon identification. The relevant track is demanded to fulfil the conditions (4.2) and (4.4) explained in section 4.1.3.
- To reduce the background from $\mu^+\mu^-$ events the information from the *opposite hemisphere* is used. The track with the highest momentum on the recoiling side has to have a normalized momentum $x_{recoil} = \frac{p_{recoil}}{E_{beam}}$ less than 0.77. Further reduction is made by demanding that this track

¹Table 4.2 shows that this cut (8) reduces the acceptance only by 0.4%.

is *not* identified as muon. To be highly efficient the μ veto as given by the condition (4.5) is used for this purpose. Clearly especially the latter removes those τ decays in which both τ 's decay into a muon ($\approx 17\%$). But these events cannot be saved as it is impossible to reduce the background from $\mu^+\mu^-$ events to a reasonable amount otherwise.

4.1.6 Acceptance

The acceptance describes the number of events seen in the detector after cuts normalized to the actual number of decays of the relevant process. It consists of the geometrical acceptance of the detector and the efficiency for the applied cuts.

The geometrical acceptance is mainly determined by the cut on the polar angle of the τ . To estimate the effect of the geometrical acceptance the $1 + \cos^2\theta$ dependence of the cross-section on the polar angle (see equation 2.3) can be used. For a cut of $|\cos\theta| < 0.9$ it is $\approx 86\%$.

The Monte Carlo is used to get the total acceptance for the relevant process with the actual cuts. This implies the correct reproduction of the relevant distributions of the data by the Monte Carlo. This is the case for the so called kinematical cuts which consist of all cuts mentioned in section 4.1.4 and 4.1.5 *except for* the muon identification. The discussion of the latter will therefore be postponed to section 4.1.7 and is excluded from the definition of the acceptance in this section.

The acceptance can be defined globally resulting in one single number. This is especially useful for test purposes because the branching ratio can be determined. Furthermore the size of the effect of individual cuts can be seen. Table 4.2 shows the effect of the cuts described in sections 4.1.4 and 4.1.5 for Monte Carlo and the data based on CLASS 15 (leptonic) events. For this purpose 30 000 $\tau^+\tau^-$ Monte Carlo events on the peak have been used. The percentage describes this number of events relative to the number of generated $\tau \rightarrow \mu\nu\nu$ decays. The cut numbers in table 4.2 serve as identifier for the corresponding cut throughout this and the next chapter. The total acceptance excluding the final muon identification is given by

$$\epsilon_{\text{acceptance}} = (52.9 \pm 0.5)\%. \quad (4.6)$$

This absolute height does not influence this analysis. But effects of the cuts on the slope in momentum and angle of the acceptance are essential. This momentum and angle dependent acceptance influences the measurement of the various parameters directly. Therefore the acceptance is determined with a Monte Carlo sample of roughly 110 000 $\tau^+\tau^-$ events at different beam energies as a function of momentum in the various angular detector regions. This is done by dividing the number of accepted events in a momentum/ $\cos\theta$ bin by the number of generated events in the same bin. For the error, fluctuations from one bin to another have been taken into account. This acceptance includes the resolution effects due to momentum and angular mismeasurements. The corresponding average acceptance for each detector region is shown in the first column of table 4.2. One can see a significant drop of the acceptance in the endcaps. This is mainly due to the cut in $|\cos\theta|$ of a track together with demanding at least one track in each

Cut number	Cut	Cumulative acceptance relative to the number of generated events in %	Events surviving cuts on data
1	$2 \leq \text{number of good tracks} \leq 6$	90.5 ± 0.3	
2	$1 \leq \text{number of good tracks/hemisphere} \leq 5$	90.1 ± 0.3	
3	at least one track with more than 3 GeV	89.3 ± 0.3	
4	cut on maximum opening angle in the jet	89.3 ± 0.3	68 708
5	total ECAL energy < 70 GeV	89.2 ± 0.3	42 833
6	acolinearity < -0.95	88.3 ± 0.3	37 466
7	energy in LCAL < 5 GeV	88.3 ± 0.3	36 734
8	only one good track in the same hemisphere	87.9 ± 0.3	32 808
9	normalized momentum > 0.1	75.7 ± 0.4	30 406
10	$ \cos\theta_{\text{track}} < 0.9$	70.9 ± 0.4	26 811
11	normalized momentum of recoil track < 0.77	67.2 ± 0.5	10 172
12	no μ veto for recoil track	52.9 ± 0.5	7 608

Table 4.2: Acceptance for individual cuts. The numbers for data do not start before cut 5 because cuts 1-4 are essentially the cuts for the definition of CLASS 15.

hemisphere: a track is not only cut because of its own $\cos\theta$, but also if the recoiling track is out of the angular range. This happens to a substantial amount only in the endcaps.

The absolute height of the acceptances in the individual detector bins (table 4.3) does not correspond to the number given in equation (4.6). This is due to the fact that the accepted events were related to the events generated in the corresponding $\cos\theta$ region of the detector. Thus, effects of angular cuts which are included in the number given in equation (4.6) do not enter the numbers given in table 4.3.

The acceptance as a function of momentum is shown in figure 4.7 together with a straight line fit. As the bins in the region $[0.9,0.95]$ for the barrel and $[0.9,1.0]$ for the endcaps are off (due to resolution effects), they are excluded from this straight line fit. To be compatible in the overlap, the bin in the region $[0.8,1.0]$ has been excluded there as well. The results are shown in the second column of table 4.3. Clearly, the restriction to $[0.1,0.9]$ or $[0.1,0.8]$ is only made to get the slope of the acceptance properly. The remaining bin is not excluded in the final fit.

To correct for the acceptance effects, the values given in table 4.3 are used to define an efficiency function $\epsilon_{\text{Acceptance}}(x, \cos\theta)$ for the region $[0.1,0.9]$ in the barrel and the endcaps and for $[0.1,0.8]$ in the overlap regions. The correction for the remaining bin is taken as the acceptance in this bin as shown in figure 4.7.

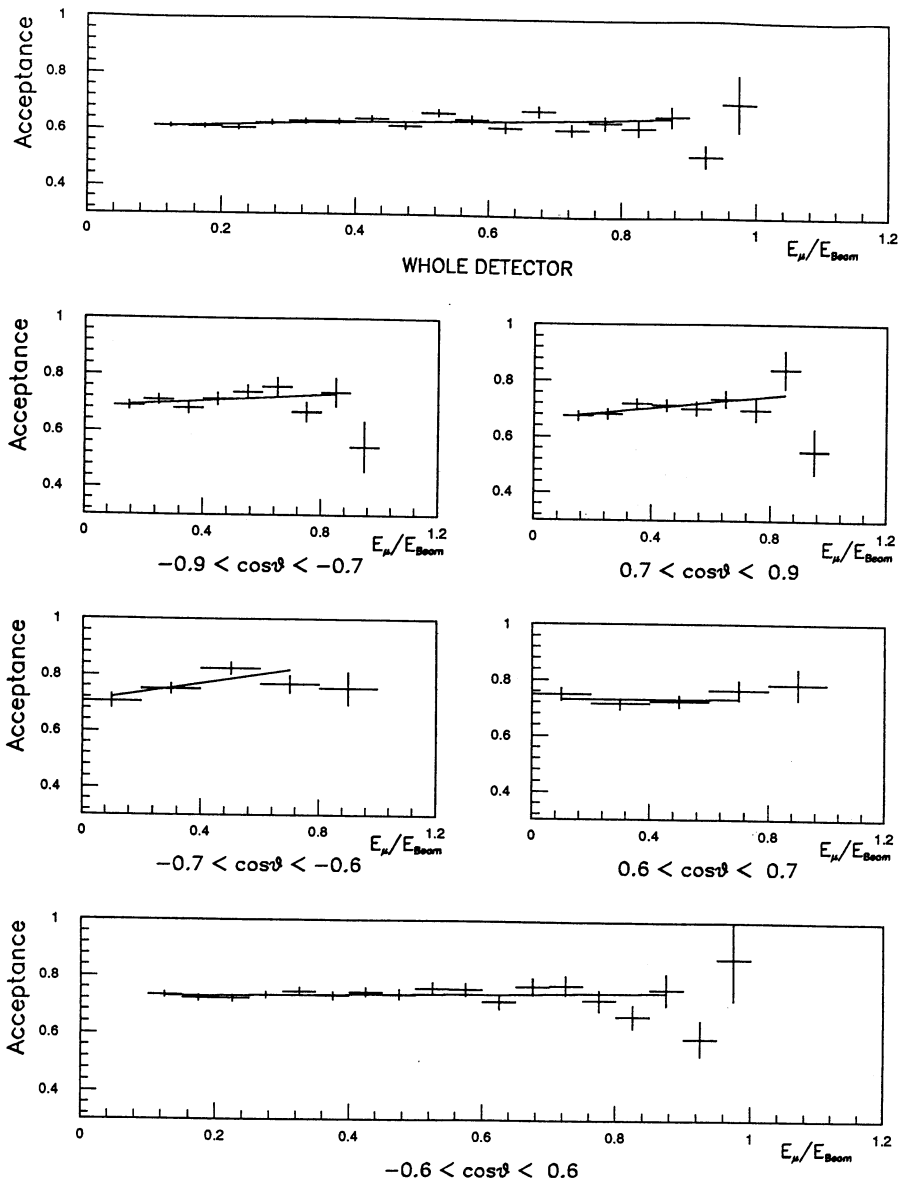


Figure 4.7: Acceptance and resolution for the different detector regions. From top to bottom the whole detector, the endcap regions (B and A), the overlap regions (B and A) and the barrel region are shown.

Detector	average acceptance in %	Slope of momentum dependence in %
OVERALL	62.6 ± 0.3	5.4 ± 1.7
ENDCAP B	70.6 ± 0.7	5.7 ± 4.3
OVERLAP B	76.4 ± 1.0	16.5 ± 6.0
BARREL	73.5 ± 0.3	2.3 ± 2.5
OVERLAP A	73.3 ± 1.1	0.3 ± 6.1
ENDCAP A	70.4 ± 0.7	10.8 ± 4.5

Table 4.3: *Acceptance (height and slope).*

4.1.7 Efficiency of Muon Identification

As already seen in figures 4.1 and 4.2 the distributions in the data are not very well reproduced by the Monte Carlo. It is therefore necessary to study the efficiency looking at data only. The momentum and angular dependence are of special interest. Two basic techniques can be used to study the muon identification. One is based on the kinematic identification of $\mu^+\mu^-$ events, the other uses a detector which is independent of HCAL to identify single muons.

To start with, the pair-tag method is described. Here one looks for well identified $\mu^+\mu^-$ events. The conditions are

- cuts 1–10;
- exactly one good track in each hemisphere;
- both normalized momenta greater than 0.77;
- total energy in ECAL less than 10 GeV.

The distribution of the total energy in ECAL as shown in figure 4.4 includes all channels. After the cuts given above (besides the cut on total energy) the distribution is shown in figure 4.8. The bulk of electron pairs at $E \approx 92 \text{ GeV}$ has already been rejected by the cut $E_{ECAL} < 70 \text{ GeV}$ (cut 5). One can see a small sample of e^+e^- events around 46 GeV. In those events one electron went into a crack. At low energies the clean $\mu^+\mu^-$ sample can be seen. Radiative $\mu^+\mu^-$ events (some energy in ECAL) are dominant above $\approx 5 \text{ GeV}$. This behaviour is very well described by the $\mu^+\mu^-$ Monte Carlo. A cut at 10 GeV leaves only very few e^+e^- events. They are estimated to be $< 0.06\%$ of the signal with 90% confidence level (estimated with e^+e^- Monte Carlo) and do consequently not bias the pair-tag sample. The total sample consists of 13 573 muons out of which 12 412 are accepted by the muon identification as described in section 4.1.3.

The efficiency for the muon identification is now given by the number of identified tracks in the pair-tag sample divided by the total number in the sample. As this sample is based on kinematic cuts only, the cracks and dead zones in the HCAL are taken into account correctly. Therefore the absolute height of the efficiency can be measured with this sample quite accurately. Furthermore the behaviour in different detector regions can

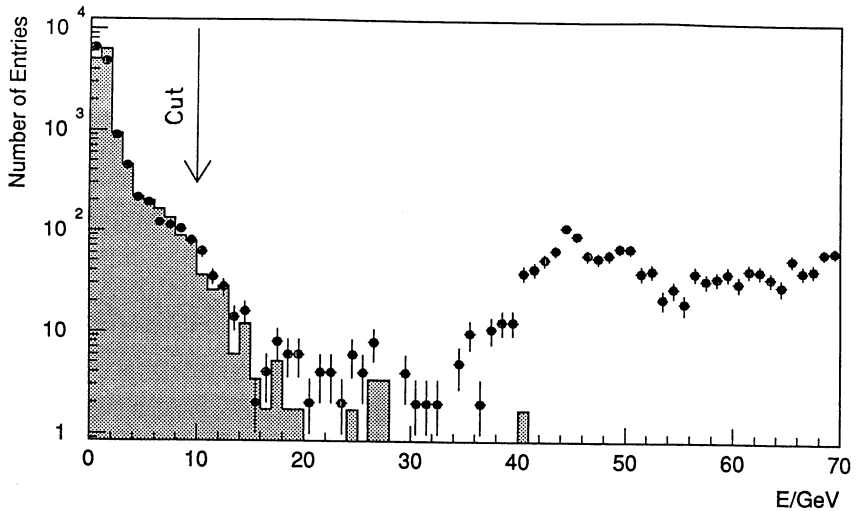


Figure 4.8: Total ECAL wire energy for $x > 0.77$ and $x_{recoil} > 0.77$. The dots with error bars are data, the shaded area is $\mu^+\mu^-$ Monte Carlo.

be studied as well. The efficiency as a function of $\cos\theta$ is shown in figure 4.9, where the different detector regions are drawn as well. It is evident that these regions correspond to different efficiencies justifying the subdivision of the HCAL as given in table 4.1.

The disadvantage of this method is the lack of information about the momentum dependence. As only $\mu^+\mu^-$ events are selected, the energy range of the tracks is restricted to momenta around $x = 1$. But, as already said before, it is essential to know the slope of the efficiency not only in angle but also in momentum. For this purpose a second tagging method is used.

The chamber-tag method (called ch-tag) identifies muons by a corresponding hit in at least one of the two muon chamber layers. The standard MCAD bank is used which assigns a hit in the MUCH to a track if its distance to the extrapolated track is less than 25 cm. The definition is:

- cuts 1-10;
- one associated hit in at least one layer of the MUCH.

As now muons of all kinds of process (and thus τ decays) enter this sample, it is possible to study the momentum dependence of the efficiency. This sample consists of 13 111 muons. The corresponding efficiencies as a function of momentum are shown for the different detector regions in figure 4.10 (muon identification) and figure 4.11 (μ veto) together with a straight line fit. Even though this method is well suited for studying the momentum dependence, some care must be taken when looking at the absolute value of the efficiencies for two reasons: The MUCH were working with a smaller efficiency in 1989. Therefore the data from 1989 are underrepresented in the testsample. The second reason

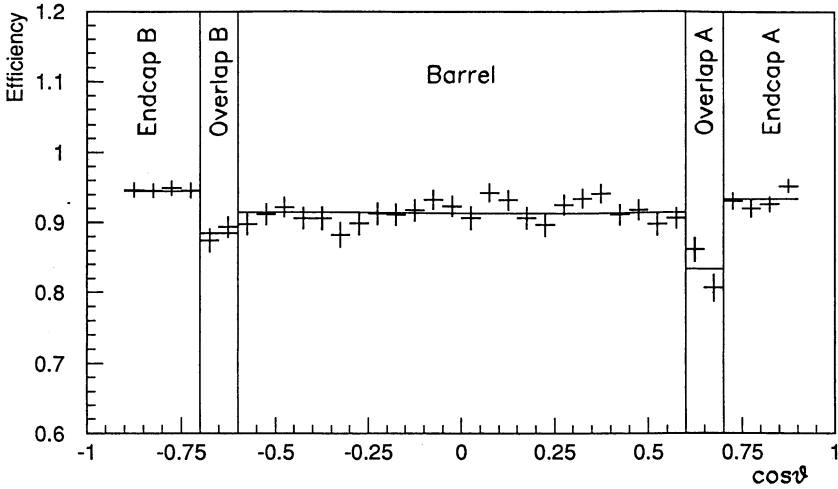


Figure 4.9: *Efficiency for muon identification (pair-tag) versus $\cos\theta$ of the track. The different detector regions are indicated.*

is the hardware situation in the barrel, where the cracks in the HCAL correspond to the cracks in the MUCH. As the efficiency is expected to drop in the cracks, the absolute height of the efficiency is overestimated by this method.

To combine the advantages of both methods (eliminating the disadvantages of both), the slope is taken from the ch-tag sample, while the absolute height in the different detector bins is taken from the pair-tag sample. In addition a check on the absolute height can be performed: following the discussion of the disadvantages of the ch-tag sample, one can eliminate the known differences between the two sample, expecting to get compatible results. Any deviation must be considered as systematic error. For this purpose both methods have been applied to a subsample of the data excluding the 1989 events and the cracks (by demanding the number of expected fired planes to be greater than 4). The deviations are shown for the muon identification and the μ veto in table 4.4. Those deviations are taken as systematic error on the measurement of the efficiencies. The absolute value (taken from the pair-tag; statistical and systematic error added in quadrature) and the slope (taken from the ch-tag; statistical error only) for the different detector regions are shown in table 4.5.

It can be seen that the slopes are more or less consistent with zero. Nevertheless the slope is taken into account for the signal where it directly influences the polarization. The efficiency for the μ veto is used only for the subtraction for the background. Therefore the effect of the slope is only of the order of background/signal after cuts. This means that the slope can be safely neglected for the μ veto.

To correct for the inefficiencies, the values given in table 4.5 are used to define an efficiency function $\epsilon_{\mu-ID}(x, \cos\theta)$.

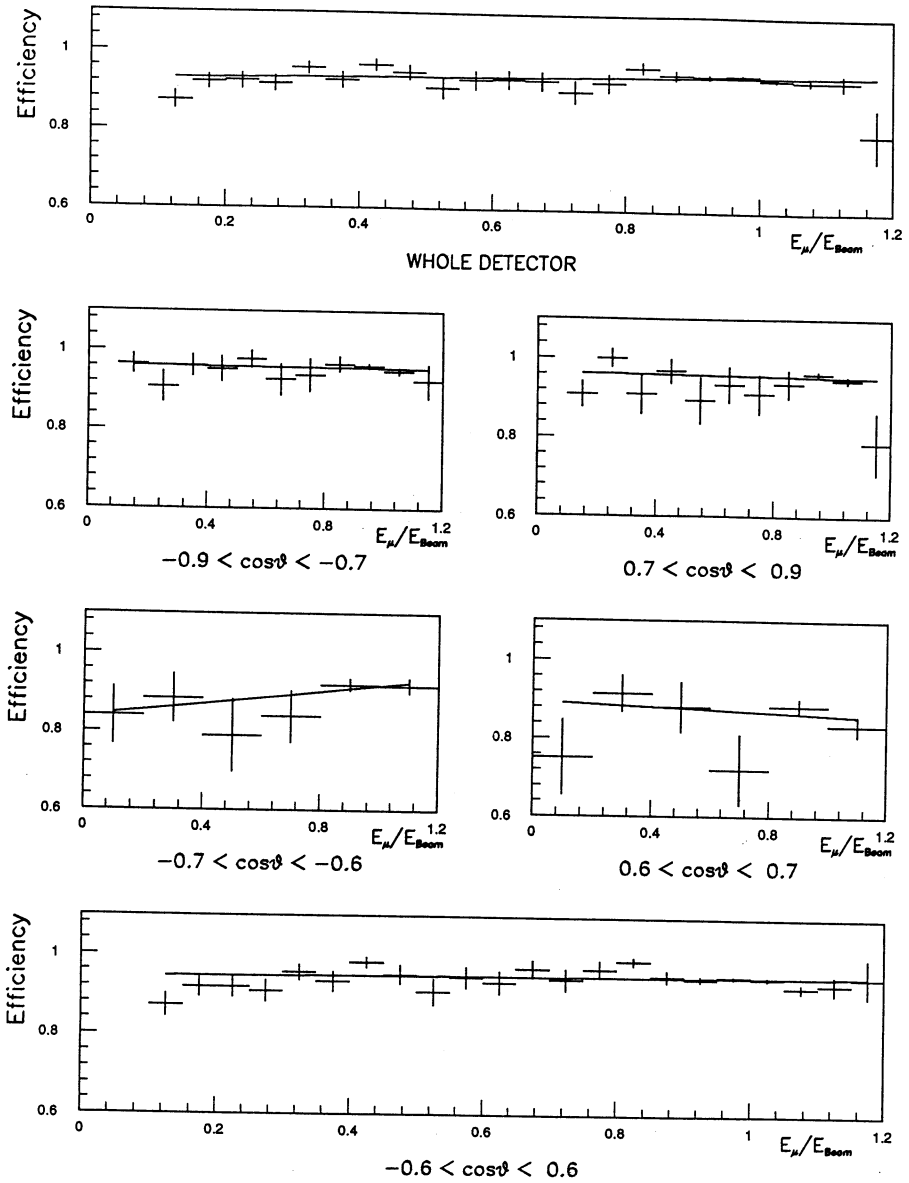


Figure 4.10: Efficiency for muon identification (ch-tag) for the different detector bins. From top to bottom the whole detector, the endcap regions (B and A), the overlap regions (B and A) and the barrel region are shown.

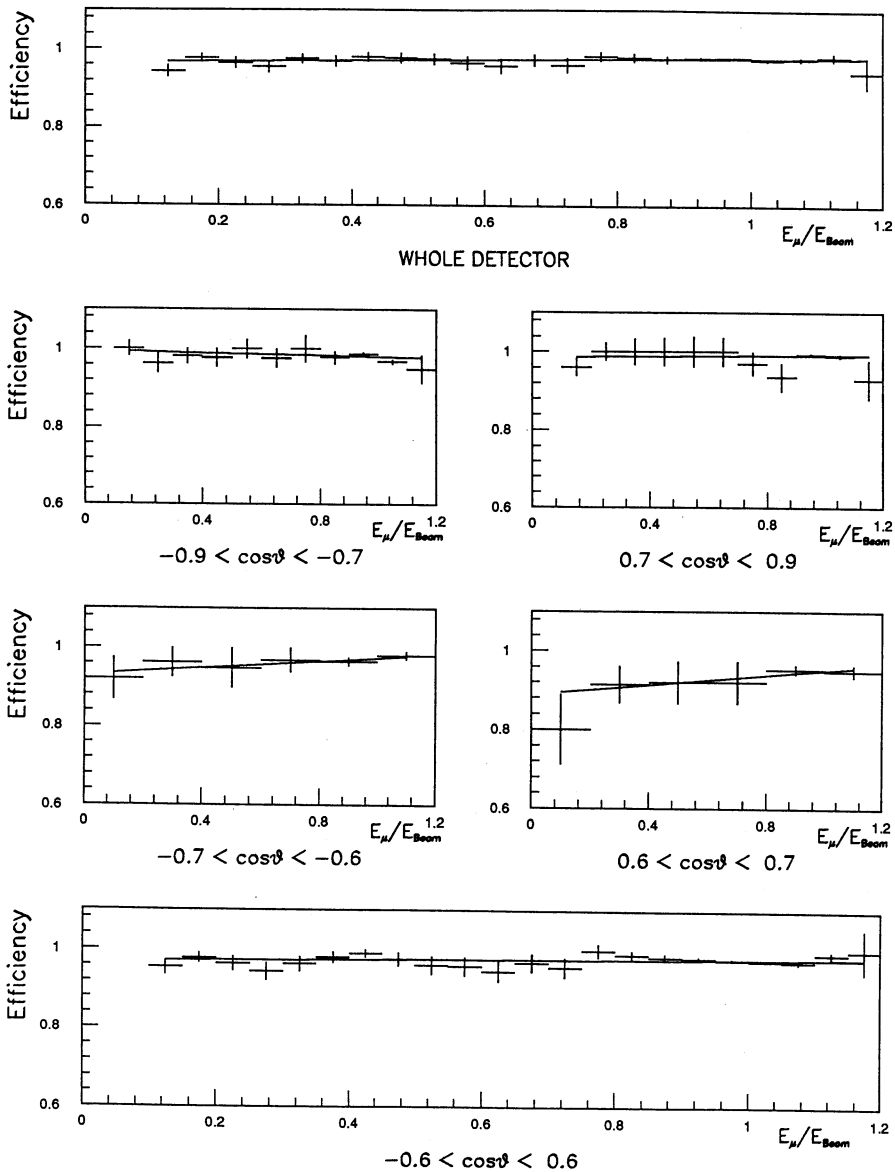


Figure 4.11: Efficiency for μ veto (ch-tag) for the different detector bins. From top to bottom the whole detector, the endcap regions (B and A), the overlap regions (B and A) and the barrel region are shown.

	Method	Overall	Endcap B	Overlap B	Barrel	Overlap A	Endcap A
$\epsilon_{\mu-ID}$	ch-tag	96.7 ± 0.2	97.6 ± 0.4	93.2 ± 1.1	97.3 ± 0.2	88.7 ± 1.3	97.3 ± 0.4
	pair-tag	96.0 ± 0.2	97.5 ± 0.4	92.1 ± 1.0	96.8 ± 0.2	87.9 ± 1.2	96.2 ± 0.5
	difference	0.7	0.1	1.1	0.5	0.8	1.1
$\epsilon_{\mu-veto}$	ch-tag	99.2 ± 0.1	99.1 ± 0.2	98.7 ± 0.5	99.5 ± 0.1	95.8 ± 0.8	99.4 ± 0.2
	pair-tag	98.7 ± 0.1	98.8 ± 0.3	97.8 ± 0.6	99.1 ± 0.1	96.1 ± 0.7	98.4 ± 0.3
	difference	0.6	0.3	1.0	0.4	0.2	1.0

Table 4.4: *Efficiencies for muon identification and μ veto in percent for ch-tag and pair-tag for 1990 data excluding cracks.*

		Overall	Endcap B	Overlap B	Barrel	Overlap A	Endcap A
$\epsilon_{\mu-ID}$	height	91.5 ± 0.8	94.5 ± 0.6	88.4 ± 1.6	91.4 ± 0.6	83.4 ± 1.5	93.3 ± 1.2
	slope	1.7 ± 1.0	-0.7 ± 2.0	8.0 ± 5.4	0.6 ± 1.1	-3.2 ± 5.5	-1.1 ± 2.2
$\epsilon_{\mu-veto}$	height	95.7 ± 0.6	97.3 ± 0.5	95.5 ± 1.2	95.2 ± 0.5	93.3 ± 0.9	97.4 ± 1.1
	slope	1.1 ± 0.6	-1.4 ± 1.5	4.3 ± 3.3	0.8 ± 0.8	6.4 ± 4.6	0.4 ± 1.7

Table 4.5: *Efficiencies for muon identification and μ veto used for the analysis for all data in percent.*

4.1.8 Requirements on Detector Quality

The selection of $\tau \rightarrow \mu\nu\nu$ candidates relies on the functioning of the HCAL. Each period in which part of the HCAL was not working well must be excluded not to bias the spectrum.

The ALEPH wide classification of a run (partly from logbook information) as "PERF", "MAYB" or "DUCK" gives a first indication of the quality. The latter have been excluded for this analysis. Furthermore the readout of the HCAL had to work. This has been checked by demanding the relevant data bank to be present for the corresponding run. Good detector conditions were guaranteed by the XLUMOK flag. This flag classifies an event as appropriate for the standard ALEPH luminosity determination. Specific logbook entries concerning the HCAL were taken into account as well. Furthermore positively identified muons (pair-tag method; HCAL not used) which were missed by the muon identification in the HCAL were plotted in separate time periods according to the HCAL module hit. Any accumulation in time in one module hints to a problem in this module. Consequently this region (and automatically the opposite one) was excluded from the selection for this period of time.

All those conditions form the basic sample which is used for the selection.

4.1.9 Trigger Efficiency

The trigger inefficiency can influence the measurements if it shows a significant momentum or angular dependence.

There have been extensive studies of the trigger efficiency in ALEPH [51, 52]. The triggers relevant for $\tau^+\tau^-$ events are based on two single arm triggers: The single charged electromagnetic trigger is defined as a track candidate in the ITC and a fired ECAL wire module in the same angular region. For this purpose the wire signals from all planes with odd numbers and all planes with even numbers in ECAL are summed up. The single muon trigger is defined as a track in the ITC and a coincidence between at least four double planes in the barrel or the endcaps in the same region. An event was accepted if at least one of these triggers has fired. The resulting trigger efficiency for $\tau^+\tau^-$ events is in all detector regions and in all time periods above 99.825%. The corresponding inefficiency leaves practically no room for a significant momentum dependence of the trigger efficiency.

4.2 Background to the Process $\tau \rightarrow \mu\nu\nu$

There are a couple of background sources. As some of them are rather large they are corrected for. The rest can be estimated and a systematic error is added.

4.2.1 $\tau^\pm \rightarrow \text{Hadron}^\pm$, Neutrino and any Number of Neutral Pions

As seen in section 2.4, roughly 50% of the τ decays contain one charged pion or kaon in the final state (kaons are not treated separately from pions). As this analysis does not take ECAL into account (this could reduce the background from channels with one pion and at least one neutral substantially) all those channels contribute to the background. Compared to the $\approx 18\%$ of the muon this is a source which has to be studied with some care. In particular the probability of the pion to be misidentified as a muon has to be determined. This misidentification is due to pion decay in flight (into a muon), pion punch-through and pion sail-through as described in section 4.1.3. The measurement of this probability using data is explained in the following.

π^0 -tag Method

ECAL is neither used to identify muons nor to cut on information in a single hemisphere. It is therefore an "independent" detector, which can be used to positively identify a pion or kaon. Using the fact that every τ decay into one-prong with at least one π^0 in the final state is accompanied by a charged pion it is sufficient to reconstruct one of these π^0 s to identify the corresponding charged track as a pion. The behaviour of this charged track can then be studied in the HCAL. The π^0 -tag method identifies a π^0 with the following cuts:

- cuts 1-10 and 12;
- Track not identified as electron (see appendix B.2);
- One of the following conditions:
 - o More than two local maxima in all clusters close to the charged track or

- exactly two clusters in ECAL close to the charged track with an invariant mass $m_{\gamma\gamma}$ of $0.10 \text{ GeV} < m_{\gamma\gamma} < 0.18 \text{ GeV}$ or
- a Bulos mass m_B (see below) of $0.07 \text{ GeV} < m_B < 0.19 \text{ GeV}$ for the cluster with a Bulos mass closest to 0.13 GeV .

The definition of a “cluster close to the track” is based on the clusters in ECAL given by the reconstruction program. The following cuts are demanded in addition:

- at least two stacks with energy;
- at least 0.1 GeV in the first stack;
- at least 0.3 GeV for the whole cluster;
- angle to the closest charge track θ_{track} between 1.2° and 20.1° .

A local maximum (within a cluster) is defined in the following way:

- storey energy $> 0.1 \text{ GeV}$ (the “storey” is one stack in a tower);
- all neighbouring storeys have smaller energy.

The distribution for data and Monte Carlo are shown in figure 4.12, where good agreement can be seen.

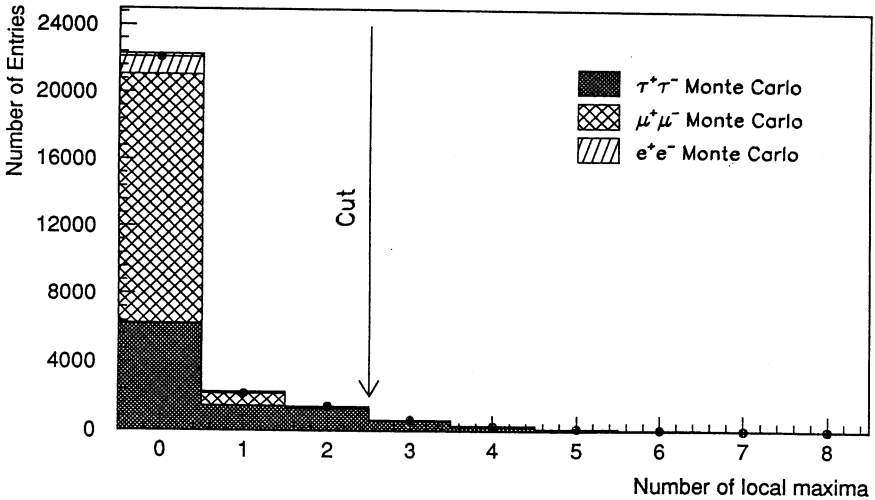


Figure 4.12: Number of local maxima in ECAL clusters. The dots with error bars are data, the shaded areas are Monte Carlo.

The invariant mass of two clusters identified in ECAL is shown in figure 4.13 (left) for illustration together with a Monte Carlo simulation. This figure shows good agreement

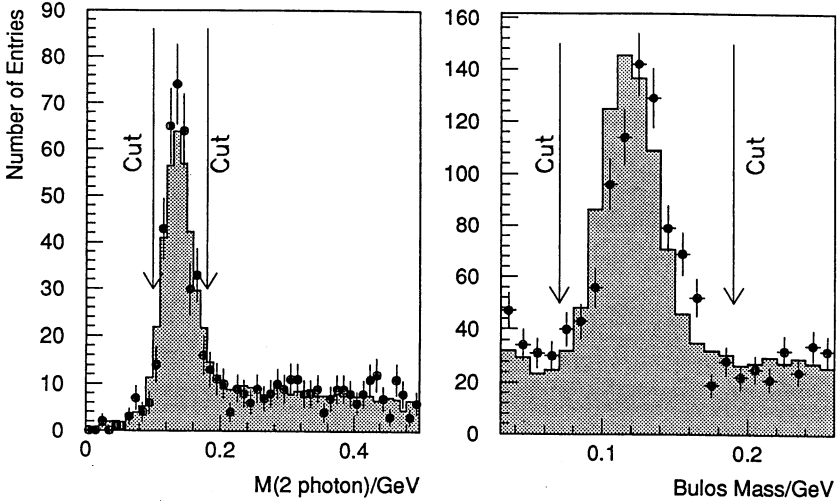


Figure 4.13: *Invariant mass of two ECAL clusters (left) and Bulos mass (right). The dots with error bars are data, the shaded area is Monte Carlo.*

at the range above the π^0 mass-peak. The peak itself is slightly narrower compared to the Monte Carlo.

The *Bulos mass* is an estimate of the invariant mass of two photons merged into one cluster. It is based on the energy and the shape of the cluster leading to a determination of the angle between the two photons. Assuming a balanced energy distribution of those photons the invariant mass can be reconstructed. A detailed description is given in [53]. The Bulos mass is systematically lower than m_{π^0} due to the assumption of equal energies. As seen in figure 4.13 (right), there is a slight shift between Monte Carlo and data. Nevertheless the shape is well reproduced.

In data 1547 events are found with the π^0 -tag method. Out of them 17 have been misidentified as muons, which gives a global pion misidentification probability of

$$\epsilon_{\pi}^0 = (1.1 \pm 0.3)\%. \quad (4.7)$$

The 17 events have been scanned and were found to be compatible with one of the processes pion punch-through, pion sail-through or pion decay. The numbers for the individual detector regions are given in table 4.6.

Events which contribute to the π^0 -tag sample can be checked with Monte Carlo. Table 4.7 shows that the potentially dangerous background from muons (either from τ decay or $\mu^+\mu^-$ events) is very small ($< 1 \mu$ in the whole sample).

Background Distributions

To correct for the remaining background, information about the momentum and angular distribution is needed. Unfortunately the statistics is too low to measure these distribu-

	Endcap B	Overlap B	Barrel	Overlap A	Endcap A
π^0 -tag sample	244	95	899	81	228
identified as μ	1	0	10	2	4
ϵ_π^0 in %	0.4 ± 0.4	0	1.1 ± 0.4	2.5 ± 1.7	1.8 ± 0.9
Events <i>hadron</i> bckgrd.	1.7	0	24.6	7.9	5.8

Table 4.6: *Pion misidentification probability and number of background events for hadronic background.*

Source	Number of events (scaled to data)
$\tau \rightarrow \text{hadron } \pi\pi^0\nu$	1521.6
$\tau \rightarrow \mu\nu\nu$	0.6
$\tau \rightarrow K\nu$ or multi $\pi\nu$	23.0
$\tau \rightarrow e\nu\nu$	1.9
$\mu^+\mu^-$	< 1.0
e^+e^-	< 10.7

Table 4.7: *Individual contributions to the π^0 -tag sample estimated from Monte Carlo and scaled to data.*

tions. Instead, the distributions for hadronic decays with one charged track in the Monte Carlo after the cuts 1-12 are taken. Then they are scaled by

$$\frac{N_{\mu,\text{data,after all cuts}}^i}{\epsilon_{\mu-Id}^i} \times \frac{N_{\pi,MC,\text{after cuts } 1-12}^i}{N_{\mu,MC,\text{after cuts } 1-12}^i}, \quad (4.8)$$

where i refers to the momentum/angular bin and “after all cuts” means cuts 1-12 and muon identification. These spectra still have to be multiplied with the pion misidentification probability, which is measured with data. But this probability is not expected to be flat in momentum (especially due to the pion decay in flight). Looking at the distribution in momentum for the whole detector (see figure 4.14) a linear fit has been performed. The idea is now to use this slope in momentum for the whole detector while the absolute height for the individual detector regions is given by the numbers in table 4.6 (third row). In this case the linear function for the misidentification probability must be written in such a way that height and slope are uncorrelated. This is done in the following way:

$$\epsilon_\pi^i(x) = \epsilon_\pi^0, i + b \left(x - \frac{\sum_j N_{\pi^0,j}^i x_j}{\sum_j N_{\pi^0,j}^i} \right), \quad (4.9)$$

where $N_{\pi^0,j}^i$ is the sample size of the π^0 -tag sample in the relevant momentum (j) and angular (i) bin. This form is obtained taking into account the boundary condition that the number of misidentified pions $N_{\pi^0,\mu}^i$ in the π^0 -tag sample in the angular bin (i) is given by

$$N_{\pi^0, \mu}^i \stackrel{\dagger}{=} \sum_j N_{\pi^0, j}^i \epsilon_{\pi}^i(x_j). \quad (4.10)$$

The slope has been fitted for the whole detector leading to

$$b = (-1.5 \pm 1.7) \%. \quad (4.11)$$

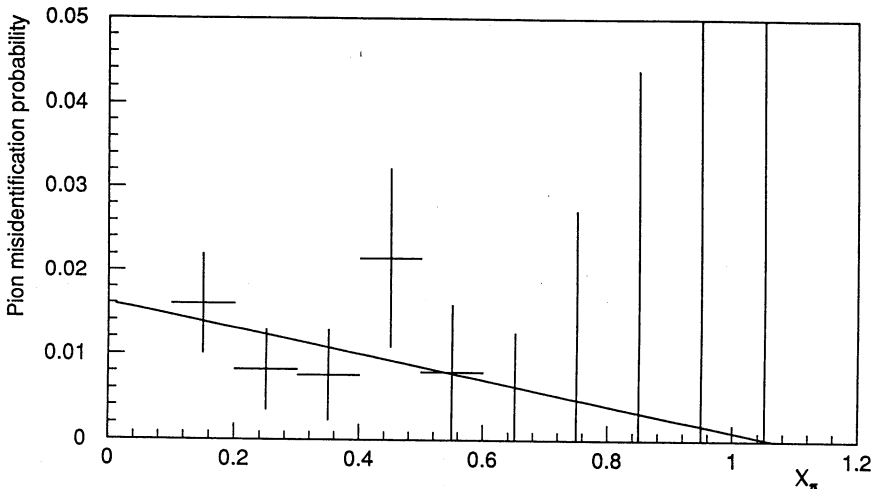


Figure 4.14: *Misidentification probability for charged pions.*

The final background distributions are shown in figure 4.15. From these a correction function $\epsilon_{\pi}(x, \cos\theta)$ is defined by relating these distributions to the signal. The number of background events in the individual detector bins are given in table 4.6 (fourth row). The total number of background events is 40 ± 10 . The error is the statistical error coming from the π^0 -tag which is the dominating one.

4.2.2 Muon Pair Background

The inefficiency of the μ veto and radiative decays (shifting the momentum of one of the muon below 0.77) lead to background from muon pairs. Furthermore the two-photon process $e^+e^- \rightarrow e^+e^-\mu^+\mu^-$ enters the sample due to the inefficiency of the μ veto.

Fortunately the background can be determined rather accurately. This is done by defining a double μ sample of events with muons in both hemispheres, which reproduces exactly the momentum/angle distribution of the background provided the μ veto is independent for the two hemispheres. The latter shall be assumed. The double μ sample

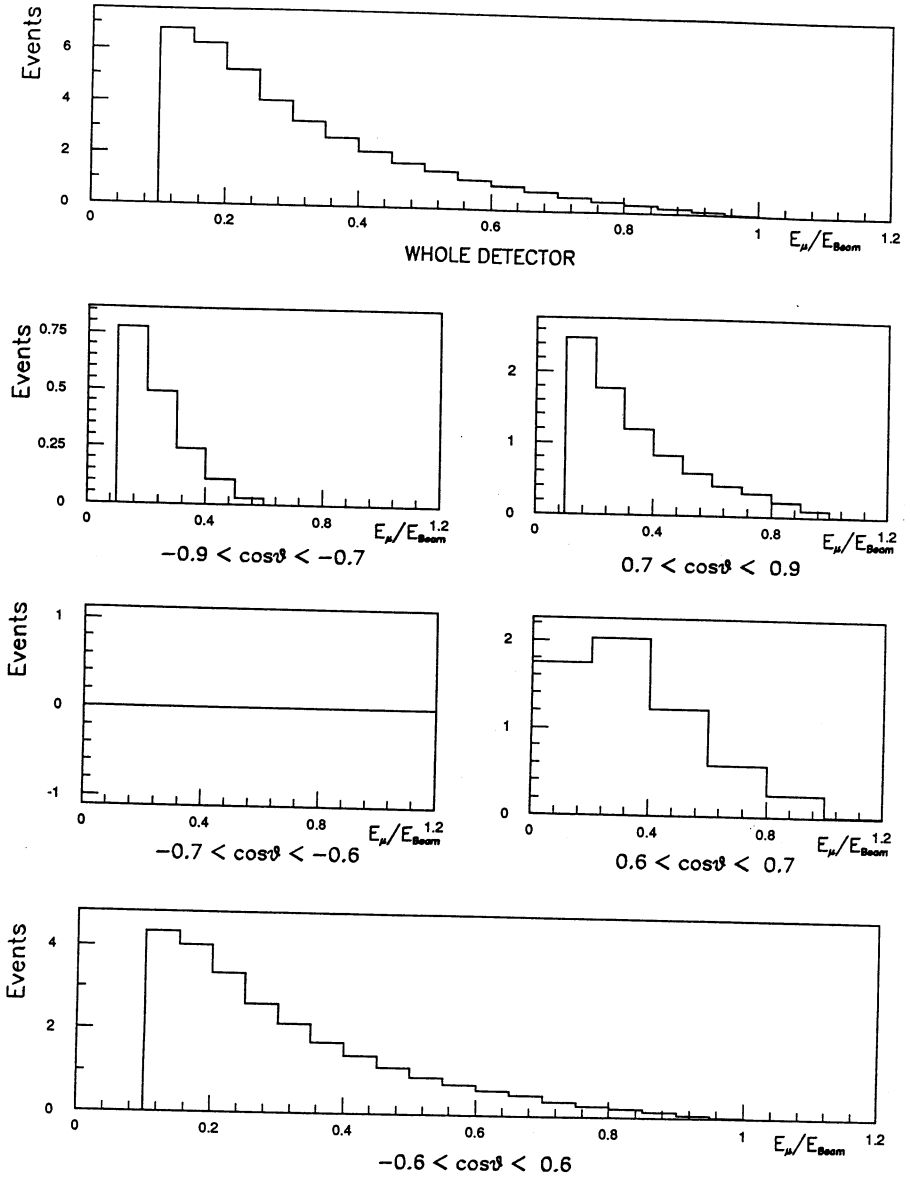


Figure 4.15: Background from $\tau^\pm \rightarrow \text{hadron}^\pm \nu \geq 0$ neutrals for the different detector regions. From top to bottom the whole detector, the endcap regions (B and A), the overlap regions (B and A) and the barrel region are shown.

	Endcap B	Overlap B	Barrel	Overlap A	Endcap A
Events μ -pair bckgrd.	4.4	2.6	29.5	3.2	4.1

Table 4.8: Number of background events for muon-pair background.

is then defined by the following cuts:

- cuts 1-11;
- in both hemispheres exactly one identified muon (using the μ veto, not the muon identification).

With the double μ sample the momentum spectrum of the background in the individual detector bins is obtained. It remains to determine the factor by which these distributions must be scaled: The number of background events $N_{\mu,\mu\text{-pair}}^i$ from muon pairs in the momentum/angle bin i is given by

$$N_{\mu,\mu\text{-pair}}^i = (1 - \epsilon_{\mu\text{-Veto}}) \epsilon_{\mu\text{-ID}} \underbrace{2 N_{\mu\text{-pair, decayed}}^i \epsilon_{\mu\text{-pair, geometrical}}^i \epsilon_{\mu\text{-pair, cuts}}^i}_{N_{\mu\text{-pair seen after cuts}}^i}. \quad (4.12)$$

“Cuts” always refers to cuts 1-11. The first bracket describes the probability of missing a muon on the recoil side. The second term describes the probability of identifying the considered track as a muon. $N_{\mu\text{-pair seen after cuts}}^i$ refers to the number of muon pairs seen in the detector after cuts 1-11. This number is given by

$$N_{\mu\text{-pair seen after cuts}}^i = N_{\mu,\mu\text{-pair from double } \mu\text{-tag}}^i \frac{1}{2} \frac{1}{\epsilon_{\mu\text{-Veto}}^2}. \quad (4.13)$$

Inserting this in equation (4.12) gives the result

$$N_{\mu,\mu\text{-pair}}^i = \frac{1 - \epsilon_{\mu\text{-Veto}}}{\epsilon_{\mu\text{-Veto}}^2} \epsilon_{\mu\text{-ID}} N_{\mu,\mu\text{-pair from double } \mu\text{-tag}}^i. \quad (4.14)$$

The expression in front of $N_{\mu,\mu\text{-pair from double } \mu\text{-tag}}^i$ is consequently the scale factor for the double μ sample. The corresponding background distributions are shown in figure 4.16. Looking at these distributions the three different contributions are the following: The peak around $x = 1$ from $\mu^+\mu^-$ events, the peak at low x corresponding to the two-photon background and the events inbetween coming from double $\tau \rightarrow \mu\nu\nu$ decays. The number of background events per detector region is given in table 4.8. The total number is 44 ± 7 events. The dominant contribution to the error comes from the uncertainty in $\epsilon_{\mu\text{-Veto}}$ as given in table 4.5.

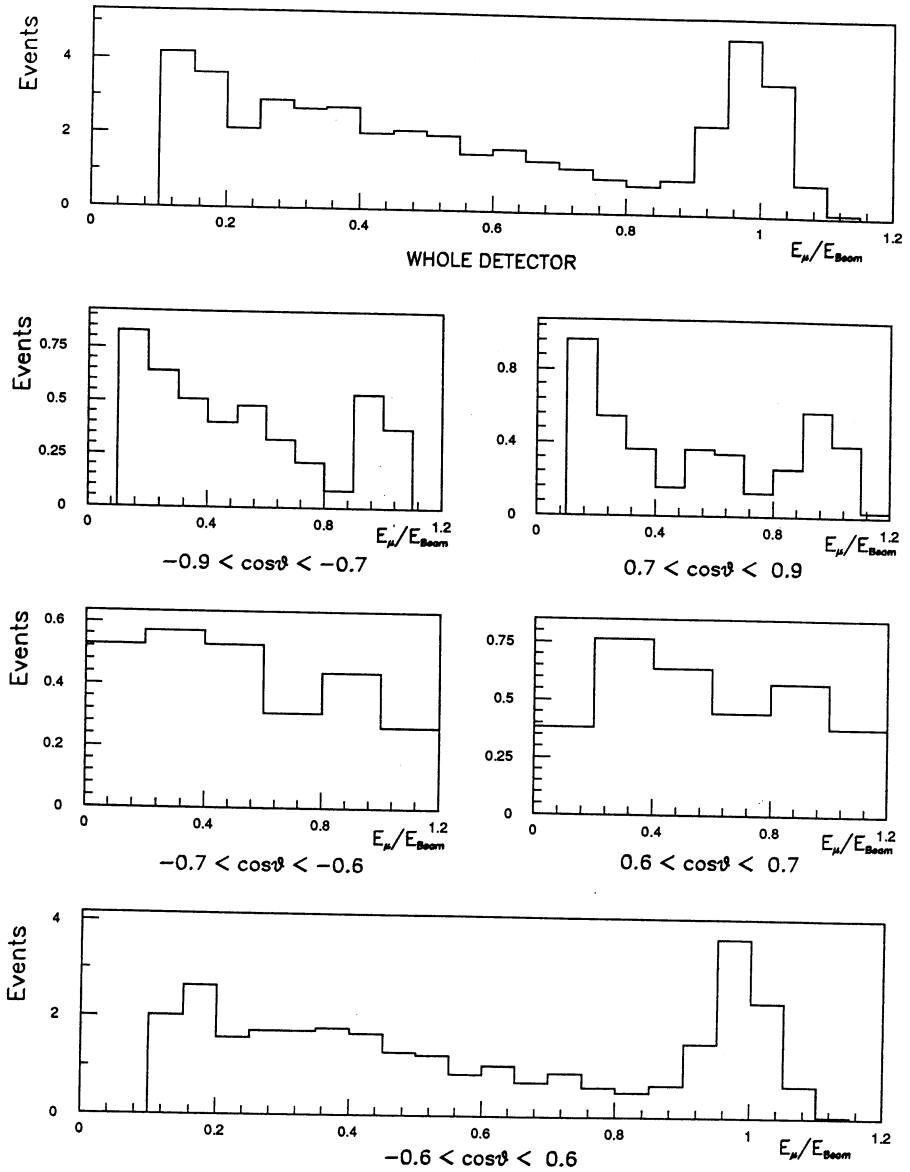


Figure 4.16: Background from muon pairs for the different detector regions. From top to bottom the whole detector, the endcap regions (B and A), the overlap regions (B and A) and the barrel region are shown.

4.2.3 Two-Photon Processes

In principle the events of the type $e^+e^- \rightarrow e^+e^-\mu^+\mu^-$ should be already subtracted as explained in section 4.2.2. This is only partially the case for the process $e^+e^- \rightarrow e^+e^-\tau^+\tau^-$. To give an upper limit of the number of events not taken into account, the acolinearity region from -0.8 to 0. in data is used as a control region to get an estimate of the number of events in the signal region (see e.g. figure 4.5). In this region 32 events in the data are found out of which 4 come from radiative τ decays estimated from Monte Carlo. The remaining 28 events are multiplied with the ratio of events in signal and control region determined by Monte Carlo ($\approx 25\%$) for two-photon events. This leads to 7 background events in the signal region for the whole detector. This is an upper limit on the remaining background, because some of this 7 events are already subtracted with the muon pair correction.

4.2.4 Hadronic Z^0 Decays

Due to the cut 1, 2, 4 and especially 8 and the muon identification the hadronic background is suppressed to a negligible amount. Using 40 000 $q\bar{q}$ Monte Carlo events, none survived the conditions for a good $\tau \rightarrow \mu\nu\nu$. Using the ratio $\Gamma_{ll}/\Gamma_{had} = (4.80 \pm 0.09)\%$ [54], the total number of $\mu^+\mu^-$ events (see section 4.3.3) correspond to $178\,000 \pm 3\,000$ hadronic decays. The upper limit with 90% confidence level for the background from $q\bar{q}$ events is 10. This number is rather large due to the limited Monte Carlo statistic. The actual contribution is assumed to be much smaller and is neglected.

As the possibly remaining background is expected to behave similarly to the two-photon background the systematic studies for the latter (see section 5.2.1) do include to some extent the effect of possible hadronic background.

4.2.5 Cosmic Rays

Clearly cosmic rays are more or less flat in D_0 . Therefore most of them are already cut by the D_0 cut. The rest is subtracted together with the muon pair correction as they enter the double μ sample. To give the order of magnitude, a contribution of $< 10^{-3}$ is found for the $\mu^+\mu^-$ final state selection [54].

4.2.6 Electron in the Final State Misidentified as Muon

The only way for an electron from e^+e^- or $\tau \rightarrow e\nu\nu$ to enter the signal sample is to be misidentified as muon. To check this misidentification probability a sample of e^+e^- events has been defined by (**e pair-tag**):

- cuts 1-4 and 6-10;
- exactly one good track in each hemisphere;
- both normalized momenta greater than 0.77;
- ECAL energy of the recoil track greater than 40 GeV.

For a subsample of the data 2235 e^+e^- events are found. The N_{10} distribution is shown in figure 4.17. Clearly none of these electrons is identified as muon. The corresponding misidentification probability is $< 0.1\%$ with 90% confidence level. Taking into account the cut at 70 GeV in the total ECAL energy (cut 5), the background from electrons is negligible.

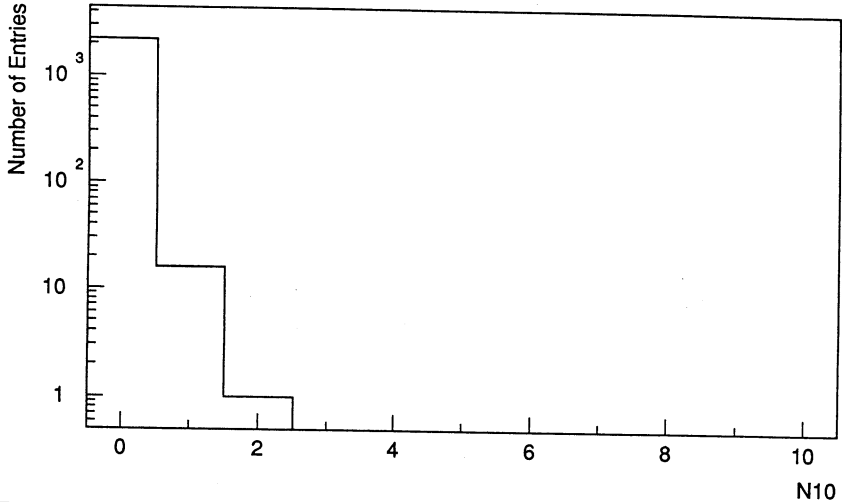


Figure 4.17: Number of fired planes within the last 10 planes for electrons (e pair-tag).

4.3 Final Distributions, Branching Ratio and Luminosity

4.3.1 Final Two-dimensional Distribution in Momentum and Angle

Applying the selection as described in the previous sections 1509 $\tau \rightarrow \mu\nu\nu$ candidates remain. They include 40 ± 10 events from hadronic τ decays, 44 ± 7 events from muon pair background and < 7 events from two-photon background neglecting the $q\bar{q}$ background. The numbers for the individual detector regions are shown in table 4.9. The corresponding distributions without any correction (neither background nor efficiency) are shown in figure 4.18, where the background is plotted as well.

The analysis for the whole detector in momentum only results in the momentum spectrum in figure 4.18 (top).

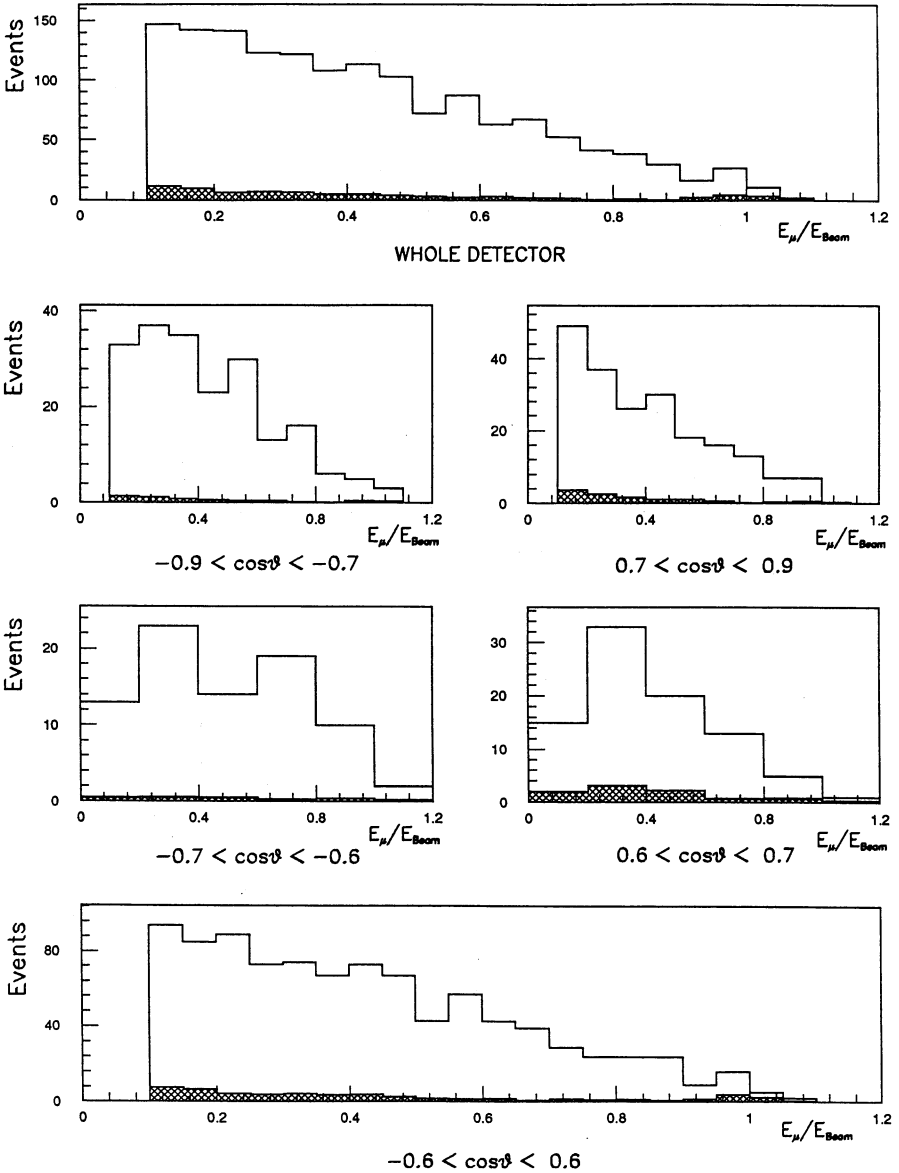


Figure 4.18: Final momentum distributions for $\tau^\pm \rightarrow \mu\nu\nu$ events in the individual detector regions. The background is shown in the shaded histogram. From top to bottom the whole detector, the endcap regions (B and A), the overlap regions (B and A) and the barrel region are shown.

	Overall	Endcap B	Overlap B	Barrel	Overlap A	Endcap A
$\tau \rightarrow \mu\nu\nu$ candidates	1509	201	81	937	87	203
$\tau \rightarrow \text{hadron} + \text{neutrals}$	40.0	1.7	0.0	24.6	7.9	5.8
μ pair	43.8	4.4	2.6	29.5	3.2	4.1
$\tau \rightarrow \mu\nu\nu$ decays	1425	195	78	883	76	193

Table 4.9: Number of $\tau \rightarrow \mu\nu\nu$ candidates and background.

4.3.2 Determination of Branching Ratio as a Cross Check

The determination of the branching ratio $BR(\tau \rightarrow \mu\nu\nu)$ provides a good check of the data selection as explained in the previous sections. It is not the aim of this thesis to determine a branching ratio with all systematic studies. On the other hand, if the branching ratio turns out to be significantly different from the expectation from the world average, this could hint to inconsistencies in the data selection.

For the normalization it is the easiest way to use the $\mu^+\mu^-$ events which are rejected at a rather late stage (cut on p_{recoil} and μ veto; cuts 11 and 12) in the standard selection. This can be done by assuming equal cross-section for $\mu^+\mu^-$ and $\tau^+\tau^-$ events. The $\mu^+\mu^-$ sample is defined exactly in the same way as explained in section 4.1.7 (pair-tag). The advantage is a rather clean sample of events ("background" from double $\tau \rightarrow \mu\nu\nu$ decays is of the order of less than 1%, from e^+e^- less than 0.15% with 90% c.l.).

The branching ratio is then given by

$$BR(\tau \rightarrow \mu\nu\nu) = \frac{1}{2} \frac{N_{\tau \rightarrow \mu\nu\nu, \text{candidates}} - N_{\text{background}}}{\epsilon_{\text{acceptance}, \tau \rightarrow \mu\nu\nu} \epsilon_{\mu-ID}} \times \frac{\epsilon_{\text{acceptance}, \mu^+\mu^-}}{N_{\mu^+\mu^-, \text{accepted}}}. \quad (4.15)$$

The efficiency $\epsilon_{\text{acceptance}, \tau \rightarrow \mu\nu\nu} = (52.9 \pm 0.5)\%$ is given in equation (4.6). To determine the acceptance for $\mu^+\mu^-$ events $\epsilon_{\text{acceptance}, \mu^+\mu^-}$ is measured with 10 000 $\mu^+\mu^-$ Monte Carlo events. Out of these 7934 pairs are accepted by the μ pair-tag method. This gives an acceptance of

$$\epsilon_{\text{acceptance}, \mu^+\mu^-} = (79.3 \pm 0.4)\%. \quad (4.16)$$

The trigger efficiency for $\mu^+\mu^-$ events is always greater than 98.5% in 1989 and greater than 99.7% in 1990 [52]. As the statistics is dominated by the 1990 data, no correction is made for the trigger efficiency.

In data 6787 events are found with the pair-tag. Consequently the branching ratio becomes

$$BR(\tau \rightarrow \mu\nu\nu) = (17.2 \pm 0.6_{\text{stat}})\%. \quad (4.17)$$

This is in very good agreement with the world average $(17.8 \pm 0.4)\%$ [3].

4.3.3 Total Luminosity Used

To give a number for the complete statistics in terms of leptonic (l^+l^-) decays and luminosity for the sample used for this analysis, the number of $\mu^+\mu^-$ events is counted. The procedure is described in section 4.3.2, where the branching ratio is determined. It results in $(8\,559 \pm 113)$ $\mu^+\mu^-$ events. Table 4.10 shows them together with the luminosity (calculated from $\sigma_{\mu\mu}(s)$ in [54]), the number of $\tau \rightarrow \mu\nu\nu$ candidates and the ratio of these candidates and the $\mu^+\mu^-$ events in the different CMS energy bins. The luminosity does not influence the analysis but is given for illustration. As the basic run selection (section 4.1.8) is slightly different from the one used for the ALEPH cross-section measurement (where the luminosity is determined via the luminosity monitors) it is appropriate to extract the luminosity from the $\mu^+\mu^-$ events.

The ratio given in the last column should not depend on the CMS energy. Besides the point at 94.2 GeV all results agree within 2σ . As the Monte Carlo for the acceptance of $\mu^+\mu^-$ events is used at the peak only, some small discrepancies going away from the peak are expected. Table 4.10 is used only as cross check and for the hadronic background so that these discrepancies can be tolerated.

\sqrt{s}/GeV	$N_{\mu\mu, \text{corrected}}$	Luminosity/ pb^{-1}	$N_{\tau \rightarrow \mu\nu\nu, \text{candidates}}$	$N_{\tau \rightarrow \mu\nu\nu \text{ candidates}}/N_{\mu\mu, \text{corrected}}$
88.2	150 ± 14	0.60 ± 0.11	21	0.14 ± 0.03
89.2	261 ± 18	0.60 ± 0.08	38	0.15 ± 0.03
90.2	550 ± 26	0.59 ± 0.06	77	0.14 ± 0.02
91.0	183 ± 15	0.14 ± 0.02	29	0.16 ± 0.03
91.2	5757 ± 85	3.89 ± 0.14	1083	0.19 ± 0.01
91.5	197 ± 16	0.13 ± 0.02	34	0.17 ± 0.03
92.2	747 ± 31	0.71 ± 0.07	119	0.16 ± 0.02
93.2	402 ± 23	0.79 ± 0.10	67	0.17 ± 0.02
94.2	306 ± 20	0.77 ± 0.13	41	0.13 ± 0.02
all	8559 ± 104	8.21 ± 0.27	1509	0.18 ± 0.01

Table 4.10: Number of $\mu^+\mu^-$ events, luminosity and $\tau \rightarrow \mu\nu\nu$ candidates for different CMS energies.

5. Results and Conclusions

The distributions of $\tau \rightarrow \mu\nu\nu$ events selected in chapter 4 are used to fit the theoretical predictions. Several possibilities of different sets of parameters as described in section 2.5.2 and 2.6.6 have been considered: The first measurement uses the one-dimensional momentum distribution to extract $\bar{g}_{\nu_e}/\bar{g}_{\nu_\tau}$ or the τ polarization. The two-dimensional distribution in momentum and angle is used to determine either $\bar{g}_{\nu_e}/\bar{g}_{\nu_\mu}$ and $\bar{g}_{\nu_e}/\bar{g}_{\nu_\tau}$ simultaneously or $\bar{g}_{\nu_e}/\bar{g}_{\nu_\mu}$ assuming lepton universality. The fourth measurement is the simultaneous determination of $\bar{g}_{\nu_e}/\bar{g}_{\nu_\tau}$ and ξ , fixing ρ to its measured value 0.731 ± 0.030 [21], assuming $\delta = 0.75$ (which corresponds to “V-A” or “V+A” at both vertices of the W in the τ decay). Here the constraint from the forward-backward asymmetry is used and an unconstrained fit is performed. All systematic studies are performed in this chapter. Finally conclusions are drawn from the various measurements and a comparison is made with the theoretical expectation within the Standard Model and with other experiments.

5.1 Fit Procedure and Treatment of Efficiency, Resolution and Background

The method applied for obtaining the results in this thesis is described in section 2.5.2 including the radiative corrections as described in section 2.6.5. The two-dimensional distribution in x and $\cos\theta$ of the muons from $\tau \rightarrow \mu\nu\nu$ decays is fit to the data. This method has been used as it is appropriate to measure different sets of observables (production or decay parameters). As a check for this method the polarization is also determined via the Monte Carlo technique as described in section 2.6.4.

For each candidate of a $\tau \rightarrow \mu\nu\nu$ decay the normalized momentum x and the polar angle $\cos\theta$ is used to calculate the likelihood function according to equation (2.44). It is taken into account that μ^+ and μ^- can be treated exactly the same way provided $-Q\cos\theta$ (Q is the charge of the track) is used as angle for the fit. This likelihood function is maximized for all candidates leading to the result. To guarantee that this formalism works on data, the efficiency, the momentum/angular resolution and the background has to be taken into account. This can be done either by correcting the data or by modifying the theoretical prediction. The latter is more appropriate because the statistical error from the selected data is taken into account properly by just using every selected $\tau \rightarrow \mu\nu\nu$ candidate. For this purpose equation (2.44) is multiplied with a global “efficiency-function” $\epsilon(x, \cos\theta)$, which is defined as

$$\epsilon(x, \cos\theta) = \epsilon_{\text{Acceptance}}(x, \cos\theta) \times \epsilon_{\mu-ID}(x, \cos\theta) \times \{1 + \epsilon_\pi(x, \cos\theta) + \epsilon_{\mu\mu}(x, \cos\theta)\}. \quad (5.1)$$

The various ϵ values are explained below:

- (i) $\epsilon_{\text{Acceptance}}$ includes the momentum resolution and the geometrical acceptance with respect to all cuts besides the muon identification. While the absolute value does not enter the final result, the slope is quite important. It is extracted from the full detector Monte Carlo as described in section 4.1.6. $\epsilon_{\text{Acceptance}}$ can be found in figure 4.7.
- (ii) $\epsilon_{\mu-ID}$ is the measured efficiency for the muon identification (see section 4.1.7) and is shown in figure 4.10. Again, the absolute value is not relevant.
- (iii) ϵ_{π} is the amount of hadronic background (see section 4.2.1 and figure 4.15) related to the signal (figure 4.18) in the corresponding x bin.
- (iv) $\epsilon_{\mu\mu}$ is the relative background from muon pair events (see section 4.2.2 and figure 4.16).

To show the quality of the fit, figure 5.1 shows the projection onto $\cos\theta$ and x_{μ} for the data together with the best fit.

5.2 Systematic Studies

Three groups of systematic uncertainties are considered in this section: The experimental uncertainties, the uncertainties due to input parameters taken from independent measurements and the intrinsic uncertainty of the fitting method. Experimental uncertainties refer to the acceptance, resolution and background described in chapter 4. All specific systematic errors for the different sets of parameters are summarized in table 5.1 and are discussed in the sections describing the results.

5.2.1 Experimental Uncertainties

Acceptance and Resolution

The acceptance and the effect of the resolution play an important role as soon as the slope in momentum and angle is nonzero. Uncertainties in these quantities lead to a bias of the measured parameters. As described in section 4.1.6 the combined effect of the acceptance and the resolution is determined with Monte Carlo. The corresponding correction distributions are shown in figure 4.7. To check the influence of the uncertainties in the slopes as given in table 4.3 these slopes are varied according to their error. As the errors in the different detector regions are independent from each other they must not be varied coherently. Instead, the slopes and the heights in the different regions are varied randomly according to a normal distribution. This is done ten times and results in a distribution for the measured parameters. The width of this distribution is given as the systematic error.

A problem which is closely related to the acceptance but should be treated separately is the cut $x_{\text{recoil}} < 0.77$ (cut 11). Due to the spin-spin correlation between the τ 's in the different hemispheres a cut in the spectrum of the recoil particle can bias the spectrum of the measured particle. The second effect is the amount of $\mu^+\mu^-$ background which

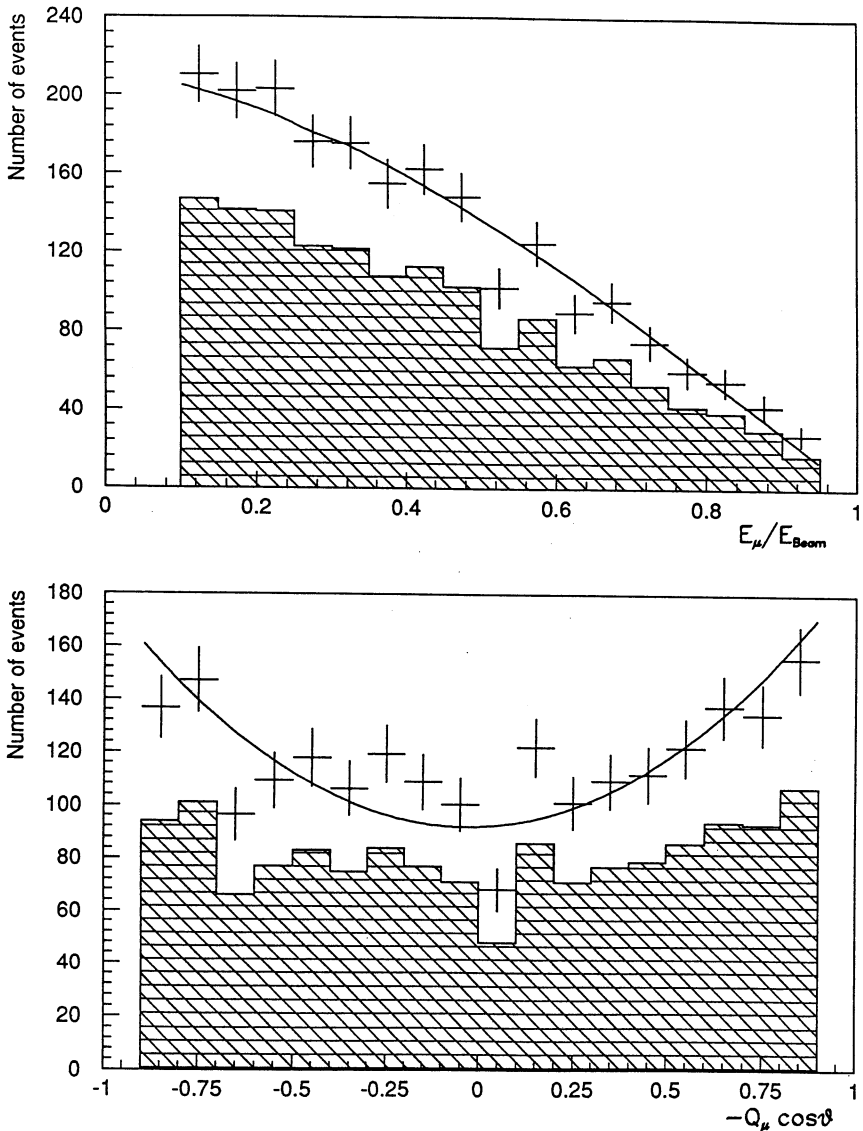


Figure 5.1: Projections onto momentum (top) and angle (bottom) of the two-dimensional momentum /angular distribution for $\tau^{\pm} \rightarrow \mu\nu\nu$ events. The shaded area is the raw data, while the error bars show the data after correction due to acceptance, resolution, efficiency and background. The best fit is shown as line.

is left after this cut. To study both effects, the cut on x_{recoil} has been varied between 0.70 and 0.83. Taking into account the number of noncommon events the corresponding systematic error is given in table 5.1.

Efficiency of Muon Identification

The slope of the muon identification biases directly the parameters. It is quite well measured with the chamber-tag sample. The effect of the variation of the slope of the muon identification within its error is given in table 5.1.

Background from $\tau^\pm \rightarrow \text{Hadron}^\pm$, Neutrino and any Number of Neutral Pions

For systematic studies the absolute height and the slope of the background has to be varied. For the slope this is done for the complete detector, while the height is varied independently in the different detector regions. For the latter the same procedure as for the acceptance is applied. The main problem of the determination of the background from the data is the small statistics of the π^0 -tag sample. For that reason the systematic error due to this background is the largest contribution (see table 5.1). As the statistics of the π^0 -tag sample is nearly equal to the amount of $\tau \rightarrow \mu\nu\nu$ candidates this systematic error decreases as the statistical error of the result decreases.

Background from Muon Pairs

One source of systematic uncertainties in the muon pair background is cut 11 on the recoil momentum. Its effect has been discussed together with the acceptance in section 5.2.1. Furthermore equation (4.14) shows that a variation of $\epsilon_{\mu-Veto}$ has a rather strong effect on the height of the background because it enters as $(1 - \epsilon_{\mu-Veto})$. Compared to this the variation of $\epsilon_{\mu-ID}$ has a negligible effect on the background. The effect of the variation of the height of the μ veto is given in table 5.1.

Background from Two-Photon Events

As already explained in section 4.2.3 the events of the kind $e^+e^- \rightarrow e^+e^-\mu^+\mu^-$ are already subtracted with the muon pair background. An upper limit for the remaining background of seven events has been given in section 4.2.3 as well. As muons from the two-photon process are predominantly at low energies and high $|\cos\theta|$, those seven events are distributed for systematic studies in the lowest momentum bin ($0.1 < x < 0.15$) in the individual detectors. To take the angular dependence into account, 2 are assumed to be in each endcap, 1 in each overlap and 1 in the barrel. Another check of the influence of the two-photon background is made by varying the cut on acolinearity from -0.95 to -0.90 (cut 6).

The resulting systematic error determined from both effects (added in quadrature) is given in table 5.1. The relative contribution of the two effects is roughly 1 : 1.

5.2.2 Variations due to Input Parameters

For the different sets of parameters different combinations of input parameters have been used ($\bar{g}_{\text{alepton}}, \bar{g}_{\text{vlepton}}, \bar{g}_{a\tau}, \bar{g}_{a\sigma}, \bar{g}_{v\sigma}$ and ρ). The measurements of \bar{g}_a are needed because equation (2.44) depends strictly on the ratio \bar{g}_v/\bar{g}_a merely on the peak. Going away from the peak there is a slight dependence on \bar{g}_a . This effect is small but has to be taken into account (see e.g. the discussion in section 2.6.5). All those parameters are taken from independent measurements (mostly within ALEPH). Their influence is checked by varying them within their errors. The corresponding uncertainties are given in table 5.1.

5.2.3 Systematic Uncertainty of Fitting Method

The main uncertainty in the fitting method comes from the treatment of the QED radiative corrections (all other approximations are shown to have a negligible effect in appendix A.2). A conservative estimate is that these corrections are understood at the level of 20%. The corresponding systematic error is given in table 5.1.

5.3 Results

5.3.1 Determination of $\bar{g}_{v\tau}/\bar{g}_{a\tau}$

The τ polarization (or $\bar{g}_{v\tau}/\bar{g}_{a\tau}$) can be determined with the momentum spectrum only, assuming ‘‘V-A’’ in the decay. This assumption is usually made to study the neutral current (essentially Z^0 exchange) only. The value of $\bar{g}_{a\tau} = -0.485 \pm 0.012$ is taken from the ALEPH measurement of $\Gamma_{\tau\tau}$ and A_{FB}^{τ} [23]. The result is (see first column of table 5.1)

$$\frac{\bar{g}_{v\tau}(s = M_Z^2)}{\bar{g}_{a\tau}(s = M_Z^2)} = 0.101_{-0.080, \text{stat}}^{+0.068} \pm 0.031_{\text{sys}}, \text{ or}$$

$$P_{\tau^-} = \left(-20.0_{-13.0, \text{stat}}^{+11.6} \pm 6.2_{\text{sys}} \right) \%. \quad (5.2)$$

The previous analysis carried out for the ALEPH publication of the τ polarization [22] has been performed similarly to the analysis described in this thesis. The muon identification inefficiency in there is worse by a factor of two. The details are described in [55] leading to $P_{\tau^-} = (-19 \pm 13_{\text{stat}} \pm 6_{\text{sys}})\%$. The improved muon identification here leads to ≈ 100 additional events which explains the smaller statistical error. Both results are in agreement taking the additional events into account.

Using the Monte Carlo method as described in section 2.6.4 the polarization is measured to be

$$\frac{\bar{g}_{v\tau}(s = M_Z^2)}{\bar{g}_{a\tau}(s = M_Z^2)} = 0.098 \pm 0.075_{\text{stat}}, \text{ or}$$

$$P_{\tau^-} = \left(-19.5 \pm 14.5_{\text{stat}} \right) \%. \quad (5.3)$$

The statistical error includes the contribution from the $\tau \rightarrow \mu\nu\nu$ candidates and from the Monte Carlo events. The statistical error from the Monte Carlo sample was dominated by 30 000 $\tau^+\tau^-$ events on the peak. Altogether 110 000 Monte Carlo events were used with appropriate weights for the different beam energies.

Both methods are in good agreement. The remaining difference can be safely assigned to the limited Monte Carlo statistics. The semi-analytical fit leads to a smaller statistical error.

5.3.2 Determination of $\bar{g}_{\nu_e}/\bar{g}_{\alpha_e}$ and $\bar{g}_{\nu_\tau}/\bar{g}_{\alpha_\tau}$

For this measurement (second column of table 5.1) the τ decay parameters are set to their Standard Model value (“V-A”) and the two-dimensional momentum/angle distribution is used. The input values $\bar{g}_{\alpha_e} = -0.501 \pm 0.003$ and $\bar{g}_{\alpha_\tau} = -0.485 \pm 0.012$ are taken from the most recent fit to the forward-backward asymmetries and the line-shapes within ALEPH [23]. These values are dominated by the width measurements. The result for the ratio of vector and axialvector couplings is

$$\frac{\bar{g}_{\nu_e}(s = M_Z^2)}{\bar{g}_{\alpha_e}(s = M_Z^2)} = 0.109^{+0.064}_{-0.054_{stat}} \pm 0.018_{sys},$$

$$\frac{\bar{g}_{\nu_\tau}(s = M_Z^2)}{\bar{g}_{\alpha_\tau}(s = M_Z^2)} = 0.119^{+0.060}_{-0.053_{stat}} \pm 0.028_{sys}. \quad (5.4)$$

The correlation coefficient is 0.37. The last number can be translated into a τ polarization of $P_{\tau^-} = (-23.5^{+10.2}_{-11.5_{stat}})\%$, which compares well with the number measured in section 5.3.1 taking into account the differences of the methods. The improvement in the statistical error by $\approx 10\%$ is due to the additional information from the angle. The measurement of the ratio of the electron couplings can be compared to the value obtained from the forward-backward asymmetries [23]: $\bar{g}_{\nu_e}(s = M_Z^2)/\bar{g}_{\alpha_e}(s = M_Z^2) = 0.070 \pm 0.028$. The corresponding result for the couplings of the τ are $\bar{g}_{\nu_\tau}(s = M_Z^2)/\bar{g}_{\alpha_\tau}(s = M_Z^2) = 0.221 \pm 0.105$. They are in good agreement. It should be stressed that the main contribution to the sensitivity with respect to $\bar{g}_{\nu_e}/\bar{g}_{\alpha_e}$ comes from the term $2A_e \cos\theta$ in equation (2.30). Usually this term is called the forward-backward polarization asymmetry $A_{pol}^{FB} = -\frac{3}{4}A_e$, which has been measured implicitly with this determination.

5.3.3 Determination of $\bar{g}_{\nu_{lepton}}/\bar{g}_{\alpha_{lepton}}$

Due to the correlation between the electron and τ couplings one can gain a little bit more than the usual $\sqrt{2}$ for the assumption of lepton universality (see third column of table 5.1). As input $\bar{g}_{\alpha_{lepton}} = -0.498 \pm 0.002$ is used, which has been obtained by the line-shape and forward-backward asymmetry fit assuming lepton universality [23] (again dominated by Γ_H). The result is

$$\frac{\bar{g}_{\nu_{lepton}}(s = M_Z^2)}{\bar{g}_{\alpha_{lepton}}(s = M_Z^2)} = 0.113^{+0.029}_{-0.033_{stat}} \pm 0.016_{sys}. \quad (5.5)$$

This can be compared to the fits to the asymmetries for lepton universality, which lead to $\bar{g}_{\nu_{\text{lepton}}}(s = M_Z^2)/\bar{g}_{\alpha_{\text{lepton}}}(s = M_Z^2) = 0.078 \pm 0.016$ [23]. They are in good agreement.

5.3.4 Determination of $\bar{g}_{\nu_\tau}/\bar{g}_{a_\tau}$ and ξ

From the measurements of the forward-backward asymmetries and the width Γ_{ee} , \bar{g}_{ν_e} and \bar{g}_{a_e} are fixed to $\bar{g}_{\nu_e} = -0.035 \pm 0.014$ and $\bar{g}_{a_e} = -0.501 \pm 0.003$ [23]. The angular information is then used to distinguish between ξ and $\bar{g}_{\nu_\tau}/\bar{g}_{a_\tau}$ (or the τ polarization P_{τ^-} ; see the fourth and fifth columns of table 5.1). This is very interesting because the usual determination of the polarization of the τ is the measurement of the product $\xi \times P_{\tau^-}$. One of the two other decay parameters ρ and δ is fixed by other measurements to $\rho = 0.731 \pm 0.030$ [21]. Unfortunately, the present statistics does not allow to fit the remaining δ and ξ simultaneously. So, the measurement of ξ can only be given under the assumption of $\delta = 3/4$ or some other fixed value.

A restriction to $\delta = 3/4$ makes sense, as it has some power in distinguishing between “V-A” and “V+A” in the charged current. As already said before (see table 2.3), “V-A” at both vertices leads to $\xi = 1$, while “V+A” at both vertices results in $\xi = -1$. For both cases δ is predicted to be $3/4$.

Two procedures are possible: Fitting $\bar{g}_{\nu_\tau}/\bar{g}_{a_\tau}$ and ξ simultaneously disregarding any other measurements in ALEPH or using the measurement of $A_{FB}^{\tau} = 0.044 \pm 0.014$ [23] as a constraint. As the main interest is the measurement of ξ , the constraint is used. This is done by adding an additional term of the form

$$\frac{1}{2} \left(\frac{A_{FB}^{\tau} - 3 \frac{\bar{g}_{\nu_\tau} \bar{g}_{a_\tau}}{\bar{g}_{\nu_\tau}^2 + \bar{g}_{a_\tau}^2} \frac{\bar{g}_{\nu_e} \bar{g}_{a_e}}{\bar{g}_{\nu_e}^2 + \bar{g}_{a_e}^2}}{\sigma_{A_{FB}^{\tau}}} \right)^2 \quad (5.6)$$

to the negative log-likelihood function. This guarantees the correct treatment of the correlation of $\bar{g}_{\nu_\tau}/\bar{g}_{a_\tau}$ and ξ getting the maximum information on ξ . Clearly the measurement of $\bar{g}_{\nu_\tau}/\bar{g}_{a_\tau}$ in this method is dominated by the constraint. The result is (fourth column in table 5.1)

$$\begin{aligned} \xi &= 0.72_{-0.34, \text{stat}}^{+0.52} \pm 0.30_{\text{Uncert. on } g_{\nu_e, \rho}} \pm 0.18_{\text{sys}}, \\ \frac{\bar{g}_{\nu_\tau}(s = M_Z^2)}{\bar{g}_{a_\tau}(s = M_Z^2)} &= 0.202_{-0.068, \text{stat}}^{+0.073} \pm 0.154_{-0.056, \text{Uncert. on } g_{\nu_e, \rho}} \pm 0.013_{\text{sys}}. \end{aligned} \quad (5.7)$$

The correlation coefficient is 0.63 and the corresponding contour plot is shown in figure 5.2 (only statistical error). To demonstrate the significance of this result for ξ , the projection of the momentum/angular distribution onto the momentum is shown in figure 5.3. The theoretical expectation for $\xi = \pm 1$ is drawn as well.

Some comment should be given for the systematic error due to the uncertainty in \bar{g}_{ν_e} : The large systematic error on $\bar{g}_{\nu_\tau}/\bar{g}_{a_\tau}$ for the constrained fit is simply the fact that due to the constraint the product $\bar{g}_{\nu_\tau} \times \bar{g}_{a_\tau} \propto A_{FB}^{\tau}$ is demanded to be more or less constant. Thus, a variation of \bar{g}_{ν_e} to lower values results in a larger value for $\bar{g}_{\nu_\tau}/\bar{g}_{a_\tau}$ and vice versa.

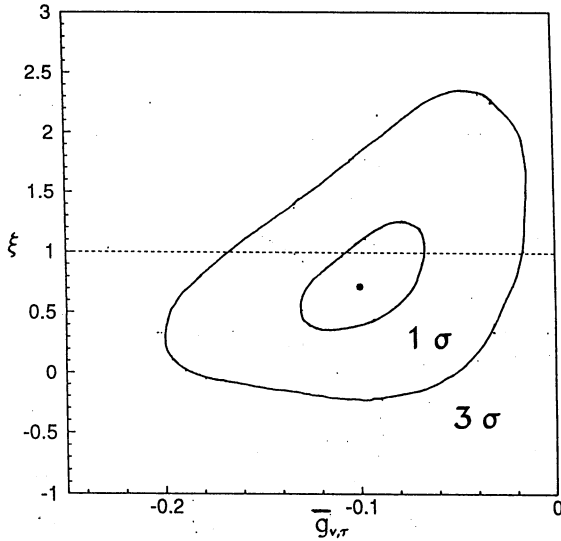


Figure 5.2: Contour plot for 1σ and 3σ change in the log-likelihood function for the fit in $\bar{g}_{\nu,\tau}$ (abscissa) and ξ (ordinate) using the constraint from A_{FB}^0 . Only the statistical error is included.

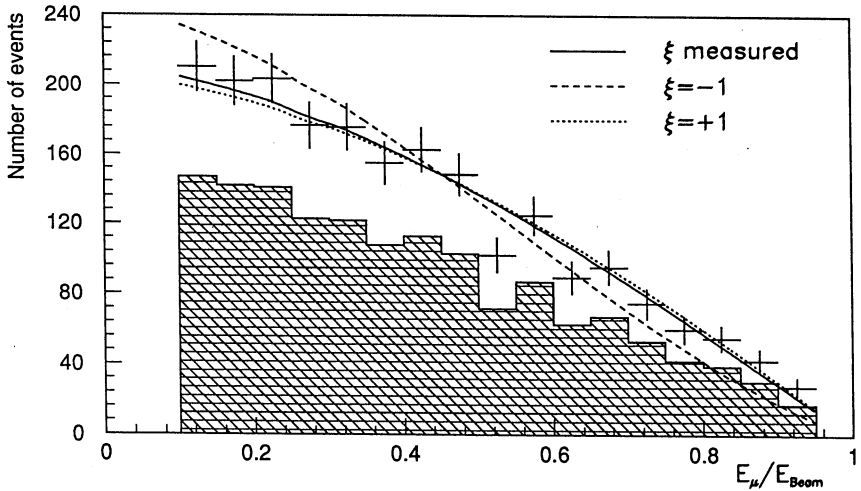


Figure 5.3: Projection onto momentum of the two-dimensional momentum/angular distribution for $\tau^\pm \rightarrow \mu\nu\nu$ events together with best fit. The theoretical expectation for $\xi = \pm 1$ is shown as well.

But most important is the fact that the influence on ξ is substantially smaller compared to the unconstrained fit.

For comparison the result of the unconstrained fit is given as well (fifth column of table 5.1):

$$\begin{aligned}\xi &= 1.22^{+1.39}_{-0.79_{\text{stat}}} \quad ^{+0.81}_{-0.15_{\text{Uncert. on } g_{\nu_e, \rho}}} \pm 0.27_{\text{stat}}, \\ \frac{\bar{g}_{\nu_e}(s = M_Z^2)}{\bar{g}_{\alpha_e}(s = M_Z^2)} &= 0.118^{+0.170}_{-0.071_{\text{stat}}} \quad ^{+0.020}_{-0.062_{\text{Uncert. on } g_{\nu_e, \rho}}} \pm 0.27_{\text{stat}}.\end{aligned}\quad (5.8)$$

The correlation coefficient is -0.17 . The unconstrained fit itself is quite sensitive to \bar{g}_{ν_e} as well. But in this case a large fluctuation of ξ to higher values corresponds to a large fluctuation of $\bar{g}_{\nu_e}/\bar{g}_{\alpha_e}$ to lower values. This can be understood in terms of the high correlation between these two quantities in the unconstrained fit. Especially the fluctuation of \bar{g}_{ν_e} to lower values causes severe problems for the fit due to this high correlation. The value given in the table corresponds therefore to the variation of -0.75σ in \bar{g}_{ν_e} rather than -1σ .

Rather soon the accuracy on \bar{g}_{ν_e} can be improved by higher statistic and/or taking other (LEP) experiments into account leading to a smaller uncertainty of this kind in ξ and $\bar{g}_{\nu_e}/\bar{g}_{\alpha_e}$.

5.4 Comparison with the Theoretical Predictions

The Standard Model of the electroweak interaction described by the gauge group $SU(2) \times U(1)$ has three free parameters (not counting the Higgs mass, the fermion masses and the fermion mixings). These can be chosen to be $\alpha_0 = 1/137.036$ (measured by the magnetic moment anomaly $g - 2$ of the electron), the Fermi coupling constant $G_F = 1.16637 \times 10^{-5} \text{ GeV}^{-2}$ (measured by the muon decay rate) and the $\sin^2\theta_W$. Of special interest within this thesis is clearly the weak mixing angle $\sin^2\theta_W$ describing the mixing between the pure $U(1)$ and pure $SU(2)$ part of the theory. Closely related to $\sin^2\theta_W$ are the weak couplings of the leptons to the Z^0 (neutral current). As already said in section 2.1 the ratio of the weak couplings are predicted to be (including electroweak radiative corrections)

$$\frac{\bar{g}_{\nu_f}(s)}{\bar{g}_{\alpha_f}(s)} = 1 - 4\overline{\sin^2\theta_{W,f}}(s). \quad (5.9)$$

Another very stringent prediction is the universality between the different lepton species. The latter can be tested looking at the results of the simultaneous determination of $\bar{g}_{\nu_e}/\bar{g}_{\alpha_e}$ and $\bar{g}_{\nu_\tau}/\bar{g}_{\alpha_\tau}$ (section 5.3.2). Another check of universality is done by the comparison of the determination of $\bar{g}_{\nu_e}/\bar{g}_{\alpha_e}$ from the momentum spectrum only (section 5.3.1) and $\bar{g}_{\nu_e}(s = M_Z^2)/\bar{g}_{\alpha_e}(s = M_Z^2) = 0.070 \pm 0.028$ from the forward-backward asymmetry measurement in ALEPH [23]. Both comparisons show *no deviation from lepton universality*.

Source	Systematic Error on					
	$\frac{g_{\tau\tau}}{g_{Ar}}$	$\frac{g_{\tau\tau}}{g_{Ar}}$	$\frac{g_{\tau\tau}}{g_{Ae}}$	$\frac{g_{\tau\tau}}{g_{A\tau\mu}}$	ξ unconstrained	ξ constrained
Acceptance	0.009	0.010	0.007	0.007	0.13 0.010	0.08 0.007
x_{recoil} cut	0.012	0.013	0.007	0.006	0.12 0.011	0.05 0.007
μ Id (slope)	0.005	0.007	$\approx 0.$	0.004	0.07 0.005	0.06 0.001
$\tau \rightarrow hadron$ bckgrd	0.020	0.015	0.006	0.007	0.16 0.009	0.11 0.007
μ veto (height)	0.002	0.001	0.003	0.002	0.06 0.008	$\approx 0.$ 0.001
2γ bckgrd	0.013	0.010	0.008	0.006	0.04 0.013	0.06 0.004
Experimental syst. error (1)	0.029	0.025	0.014	0.014	0.26 0.024	0.17 0.013
Uncertainty in $g_{A\tau\mu}$	—	—	—	0.001	—	—
Uncertainty in g_{ν_e}	—	—	—	—	$\begin{smallmatrix} +0.80 \\ -0.05 \end{smallmatrix}$ $\begin{smallmatrix} +0.005 \\ -0.048 \end{smallmatrix}$	0.28 $\begin{smallmatrix} +0.154 \\ -0.058 \end{smallmatrix}$
Uncertainty in g_{Ae}	—	0.001	0.001	—	0.08 0.009	$\approx 0.$ 0.001
Uncertainty in g_{Ar}	0.001	0.002	0.001	—	0.04 0.005	$\approx 0.$ $\approx 0.$
Uncertainty in ρ	—	—	—	—	0.11 0.016	0.10 0.001
Uncertainties of parameters (2)	0.001	0.002	0.001	0.001	$\begin{smallmatrix} +0.81 \\ -0.15 \end{smallmatrix}$ $\begin{smallmatrix} +0.020 \\ -0.052 \end{smallmatrix}$	0.30 $\begin{smallmatrix} +0.154 \\ -0.058 \end{smallmatrix}$
Theoretical Uncertainties (QED radiative corr.) (3)	0.012	0.012	0.012	0.007	0.06 0.012	0.06 0.002
Total systematic error (1) \oplus (2) \oplus (3)	0.031	0.028	0.018	0.016	$\begin{smallmatrix} +0.85 \\ -0.31 \end{smallmatrix}$ $\begin{smallmatrix} +0.033 \\ -0.059 \end{smallmatrix}$	0.35 $\begin{smallmatrix} +0.155 \\ -0.058 \end{smallmatrix}$

Table 5.1: Systematic errors for the different measurements. All couplings should read with bars (effective couplings).

This confirmation of lepton universality allows one to use this prediction of the theory to perform a determination of $\bar{g}_{\nu_{\text{lepton}}}/\bar{g}_{a_{\text{lepton}}}$. The aim is clearly to get the maximum information about $\overline{\sin^2\theta_W}$ according to equation (5.9). The result given in section 5.3.3 leads to the measurement of the running “effective” $\overline{\sin^2\theta_W}(s = M_Z^2)$ of

$$\overline{\sin^2\theta_W}(s = M_Z^2) = \frac{1}{4} \left(1 - \frac{\bar{g}_{\nu_{\text{lepton}}}(s = M_Z^2)}{\bar{g}_{a_{\text{lepton}}}(s = M_Z^2)} \right) - 0.0007 = 0.2211 \pm 0.0087. \quad (5.10)$$

The term 0.0007 [35] corresponds to the flavour dependent correction as described in section 2.6.1.

The Standard Model describes the charged current by the exchange of the charged W^\pm bosons. The main characteristic is (besides the lepton universality) the “V-A” structure as described in section 2.5.1. For the muon decay no deviation from “V-A” structure has been found so far [3]. For the τ there are only a couple of measurements for the ρ parameter for the decay in electron or muon (dominated by the ARGUS measurement [21]). This measurement is used as input for the measurement of the ξ parameter in this thesis. The finite polarization of the τ allows for the first time a measurement of ξ and δ . As the statistics is not yet large enough to fit ξ and δ simultaneously, only the two special cases of “V-A” or “V+A” at both vertices are considered (c.f. table 2.3). These two alternatives have the corresponding values $\xi = +1$ and $\xi = -1$, respectively, while δ and ρ are $3/4$ for both cases. The measurement presented in section 5.3.4 allows the exclusion of the “V+A” alternative by 3.5 σ .

5.5 Comparison with Other Measurements

The determination of the ξ parameter for the τ as performed in this thesis is the first measurement of this parameter [3]. Hence, only the production parameter of the τ can be compared to results of other experiments in this section.

A first comparison with independent ALEPH measurements has been made already in the sections 5.3.1-5.3.3 together with the presentation of the corresponding measurements. The measurements of the forward-backward asymmetries A_{FB} and the widths Γ_{ll} lead to the values for $\bar{g}_{a_l}(s = M_Z^2)$ and $\bar{g}_{\nu_l}(s = M_Z^2)$ as given in table 5.2. In this table the results as given in section 5.3.2 are shown as well. All measurements are in good agreement. The small correlation due to the fact that the $\tau \rightarrow \mu\nu\nu$ events are already included in the measurement of A_{FB}^τ and $\Gamma_{\tau\tau}$ is neglected.

As already said in section 5.4 no evidence for lepton universality breaking is found. Hence, the measurement of A_{FB} and Γ_{ll} for all leptonic final states can be combined to get a measurement of $\bar{g}_\nu(s = M_Z^2)$ and $\bar{g}_a(s = M_Z^2)$. This is shown in the last row of table 5.2 and in figure 5.4, where \bar{g}_ν versus \bar{g}_a is plotted. The result for $\bar{g}_\nu(s = M_Z^2)/\bar{g}_a(s = M_Z^2)$ from this thesis as given in section 5.3.3 is shown as straight line (one and three sigma region). While the measurements of the asymmetries give no handle on the relative sign of \bar{g}_ν and \bar{g}_a the result of this thesis is sensitive to the relative sign and allows to solve the ambiguity. The measurements are in good agreement; the sensitivity of only one decay channel of the τ with respect to \bar{g}_ν/\bar{g}_a is remarkable.

Couplings of Z^0 to	Measurements from A_{FB} and Γ_{ll}		This thesis ($e^+e^- \rightarrow \tau^+\tau^-$; $\tau \rightarrow \mu\nu\nu$)
	$\bar{g}_{\alpha_l}(M_Z^2)$	$\bar{g}_{\nu_l}(M_Z^2)$	$\bar{g}_{\nu_l}(M_Z^2)$ (using $\bar{g}_{\alpha_l}(M_Z^2)$ from column 2)
e^+e^-	-0.5005 ± 0.0028	-0.035 ± 0.014	-0.055 ± 0.031
$\mu^+\mu^-$	-0.4938 ± 0.0044	-0.027 ± 0.024	—
$\tau^+\tau^-$	-0.4852 ± 0.0122	-0.107 ± 0.051	-0.058 ± 0.031
l^+l^-	-0.4980 ± 0.0021	-0.039 ± 0.008	-0.056 ± 0.017

Table 5.2: Comparison of \bar{g}_ν and \bar{g}_α measurements within ALEPH [29] and this thesis.

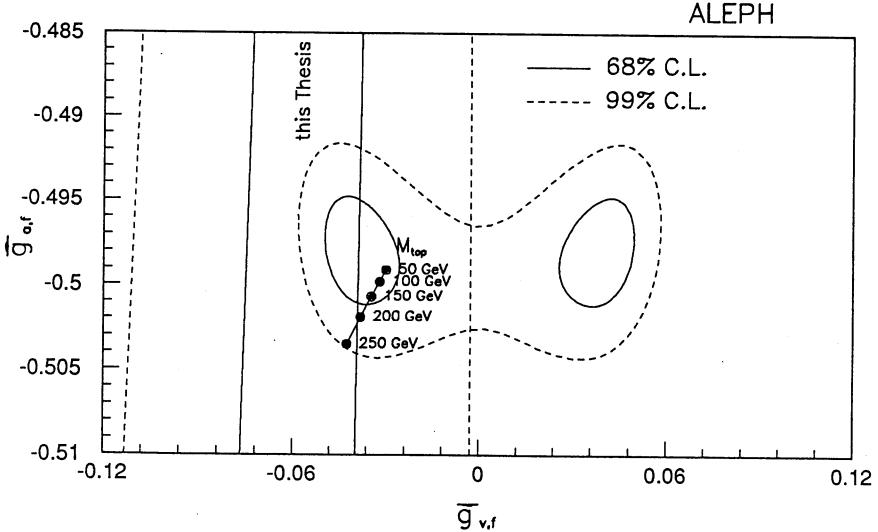


Figure 5.4: $\bar{g}_\nu(s = M_Z^2)$ versus $\bar{g}_\alpha(s = M_Z^2)$ for the overall ALEPH fit to the forward-backward asymmetries [29] and the widths and the result for this thesis. The prediction of the Standard Model for different M_{top} values is shown as well. For this calculation M_{top} , M_Z , α_s and M_{Higgs} are used. The mean value for $M_{Higgs} = 50 \text{ GeV}$ and $M_{Higgs} = 1000 \text{ GeV}$ is plotted.

Channel	$e\nu\nu$	$\mu\nu\nu$	$\pi\nu$	$\rho\nu$	$a_{1\nu}$
Result for P_{τ^-}	-0.360	-0.203	-0.130	-0.124	-0.150
Error on P_{τ^-}	0.180	0.139	0.078	0.069	0.166
Theoretical weight (section 2.4.4)	0.07	0.07	0.32	0.50	0.03
Final weight in ALEPH measurements [22])	0.06	0.10	0.33	0.43	0.07

Table 5.3: *Results and weights for the τ polarization with different channels. All values can be found in [22] except for the muon channel which is the result of this thesis.*

The measurement of the polarization from the momentum spectrum only (as described in section 5.3.1) can be compared with the polarization measurements in ALEPH with other decay channels. They are shown in table 5.3 where good agreement between the results is found. In section 2.4.4 the sensitivity on the polarization for the different decay channels has been given for an ideal detector. Table 5.3 shows as well the relative weights of the polarization measurements of the single channels compared to the ones expected for ideal detector conditions. It can be seen that due to excellent detector and background conditions the muon channel could contribute substantially more than expected.

It is now interesting to compare the measurements with results of other experiments. Of special interest are here the e^+e^- experiments at lower energies at PEP, PETRA and TRISTAN, combined in [24]. There a fit of A_{FB}^{τ} and $R_{\tau\tau} = \sigma(e^+e^- \rightarrow \tau^+\tau^-) / \frac{4\pi\alpha^2}{3s}$ to all data available leads to the measurement $g_{\nu\tau} = -0.09^{+0.25}_{-0.28}$ and $g_{a\tau} = -0.484 \pm 0.034$. The corresponding ratio $g_{\nu\tau}/g_{a\tau} = 0.19^{+0.58}_{-0.52}$ is in agreement with the result obtained in this thesis, while the accuracy is improved here by nearly an order of magnitude.

In the same reference a brief discussion of the τ polarization measurement at $\sqrt{s} < M_Z$ is given as well. CELLO [56] at PETRA has measured $g_{\nu\tau}/g_{a\tau} = -0.1 \pm 2.8$, while MAC [57] at PEP obtained $g_{\nu\tau}/g_{a\tau} = -0.05 \pm 0.21 \pm 0.34$ and $g_{a\tau}g_{\nu\tau} = (0.26 \pm 0.31)(1 \pm 0.011)$. A recent measurement of AMY [58] at TRISTAN has lead to $g_{\nu\tau}/g_{a\tau} = 0.95 \pm 0.71$. All measurements agree with the result given in this thesis, the improvement in the precision is one order of magnitude.

The world average of $\sin^2\theta_W$ (including LEP experiments) as given in equation (2.34) for a top mass of 100 GeV and a Higgs mass of 100 GeV is 0.2305 ± 0.0005 [3]. Applying the appropriate universal corrections ($\Delta\kappa \approx 10^{-2}$ [35]) to result (5.10) one gets $\sin^2\theta_W = 0.2189 \pm 0.0087$ as result for this thesis. Both values are in agreement within 1.3σ .

5.6 Conclusions

The two-dimensional momentum/angle distribution of muon from τ decays has been used to extract several combinations of parameters. The $\tau^+\tau^-$ production parameters $\bar{g}_{\nu_e}/\bar{g}_{a_e}$ and $\bar{g}_{\nu_\tau}/\bar{g}_{a_\tau}$ at $\sqrt{s} = M_Z$ show no deviation from the Standard Model. The measurement of the couplings of the τ improves former results by nearly an order of magnitude in the error.

The simultaneous determination of electron and τ couplings as described in result (5.4) corresponds to the simultaneous measurement of the polarization *and* of the forward-backward asymmetry of the polarization. Comparing the error on $\bar{g}_{\nu_\tau}/\bar{g}_{a_\tau}$ with the measurement from momentum only one gains roughly 10% in the statistical error. In addition one gets a new determination of $\bar{g}_{\nu_e}/\bar{g}_{a_e}$. As this measurement is linear in $\bar{g}_{\nu_e}/\bar{g}_{a_e}$, the sensitivity is only $\approx 30\%$ worse compared to the sensitivity for the determination from the forward-backward asymmetry for the e^+e^- final state. Consequently, doing this analysis in a similar manner with the other τ decay channels can increase the sensitivity on $\bar{g}_{\nu_e}/\bar{g}_{a_e}$ substantially.

A determination of $\sin^2\theta_W$ from $\bar{g}_{\nu_{lepton}}/\bar{g}_{a_{lepton}}$ assuming lepton universality is in agreement with other measurements.

The determination of ξ and $\bar{g}_{\nu_\tau}/\bar{g}_{a_\tau}$ with the constraint from the forward-backward asymmetry is the first measurement of ξ . Although the result still depends on the value for δ , the sensitivity is remarkable. Even with the restriction $\delta = 3/4$ the value of ξ still allows one to distinguish between "V-A" and "V+A" at both vertices of the W . Result (5.7) excludes the "V+A" ($\xi = -1$) combination by more than 3.5σ .

A. Further Equations, Formulas and Checks

A.1 Lorentz Transformation

Looking at the decay of a particle with mass m_p , energy E_p and momentum \vec{p}_p into n particles with masses m_i , their momenta and energies in the laboratory system are given by

$$\begin{aligned}\vec{p}_{i,LAB} &= \vec{p}_{i,CMS} + \frac{\vec{p}_p}{m_p} \left\{ E_{i,CMS} + \frac{\vec{p}_{i,CMS} \cdot \vec{p}_p}{E_p + m_p} \right\} \\ E_{i,LAB} &= \frac{1}{m_p} \{ E_{i,CMS} E_p + \vec{p}_{i,CMS} \cdot \vec{p}_p \}.\end{aligned}\tag{A.1}$$

Now the specific case of a τ decaying into $\mu\nu\nu$ is considered, where only the muon is visible as mentioned in section 2.5.1. Defining the "reduced" CMS energy x^* and the reduced LAB energy x of the muon and the angle θ^* between the spin of the muon and the momentum of the τ (using the helicity p of the τ) in the τ rest frame:

$$\begin{aligned}x^* &= \frac{E_{\mu,CMS}}{\frac{m_\tau}{2} \left(1 + \frac{m_\mu^2}{m_\tau^2} \right)} \\ &\approx \frac{2E_{\mu,CMS}}{m_\tau},\end{aligned}\tag{A.2}$$

$$\begin{aligned}x &= \frac{E_{\mu,LAB}}{E_\tau}, \\ \cos\theta^* &= p \frac{\vec{p}_{\mu,CMS} \cdot \vec{p}_\tau}{p_{\mu,CMS} p_\tau}.\end{aligned}\tag{A.3}$$

Taking these variables and equation (A.1) into account, x becomes

$$\begin{aligned}
x &= \frac{E_{\mu,LAB}}{E_{\tau}} = \frac{1}{m_{\tau}} \left\{ E_{\mu,CMS} + \frac{\vec{p}_{\mu,CMS}}{E_{\tau}} \cdot \vec{p}_{\tau} \right\} \\
&= \frac{1}{m_{\tau}} \left\{ E_{\mu,CMS} + p \cos\theta^* \frac{p_{\tau}}{E_{\tau}} p_{\mu,CMS} \right\} \\
&\stackrel{(p_{\tau}=E_{\tau})}{=} \frac{1}{2} x^* + p \cos\theta^* \frac{p_{\mu,CMS}}{m_{\tau}} \\
&\stackrel{(p_{\mu,CMS}=E_{\mu,CMS})}{=} \frac{x^*}{2} \{1 + p \cos\theta^*\}, \text{ or} \\
x^* &= \frac{2x}{1 + p \cos\theta^*} \tag{A.4}
\end{aligned}$$

The validity of the approximations made for this calculation has been checked in section A.2.

Taking the decay rate in the CMS system of the τ (equation 2.26), we get the decay rate in the LAB system by boosting via equation (A.4) and integrating over $\cos\theta^*$:

$$\frac{d\Gamma(x)}{dx} = \int \frac{d^2\Gamma}{x^* d\cos\theta^*}(x^*, \cos\theta^*) \frac{dx^*}{dx} d(\cos\theta^*). \tag{A.5}$$

As the reduced energy x^* has to be smaller than one, the range for $\cos\theta^*$ is limited to

$$\cos\theta^* \geq p(2x - 1). \tag{A.6}$$

To take into account the different range for different polarizations, the integration can be performed over $d(p \cos\theta^*)$ rather than $d(\cos\theta^*)$ using the same integration interval:

$$\frac{d\Gamma}{dx}(x; \rho, \delta, \xi, p) = \int_{2x-1}^1 \left(\frac{d^2\Gamma}{x^* d\cos\theta^*}(x^*, \cos\theta^*; \rho, \delta, \xi, p) \frac{dx^*}{dx} \right)_{x^* = \frac{2x}{1+p \cos\theta^*}} d(p \cos\theta^*). \tag{A.7}$$

The result is equation (2.28).

A.2 Validity of Approximations for the Analytical Calculations

Several approximations have been used up to now to yield equation (2.29). The first step in the direction of using this analytical equation for the data, is to check how the approximations

- (i) $\frac{m_{\mu}}{m_{\tau}} \ll 1$,
- (ii) $\frac{m_{\mu}}{E_{\mu}^{CMS}} \ll 1$,
- (iii) $\theta_{\mu} \approx \theta_{\tau}$

influence the result. The effect of the approximations (i) and (ii) can be seen by looking at the ratio of equation (2.18) and the correct spectrum from a Monte Carlo simulation. As it is important to check whether there is any bias on the measurement of the polarization or ξ , this ratio is determined for $p = +1$ and $p = -1$ separately. The Monte Carlo simulation takes all effects mentioned above into account. Figure A.1 shows this ratio for $p = +1$ (top left) and $p = -1$ (top right).

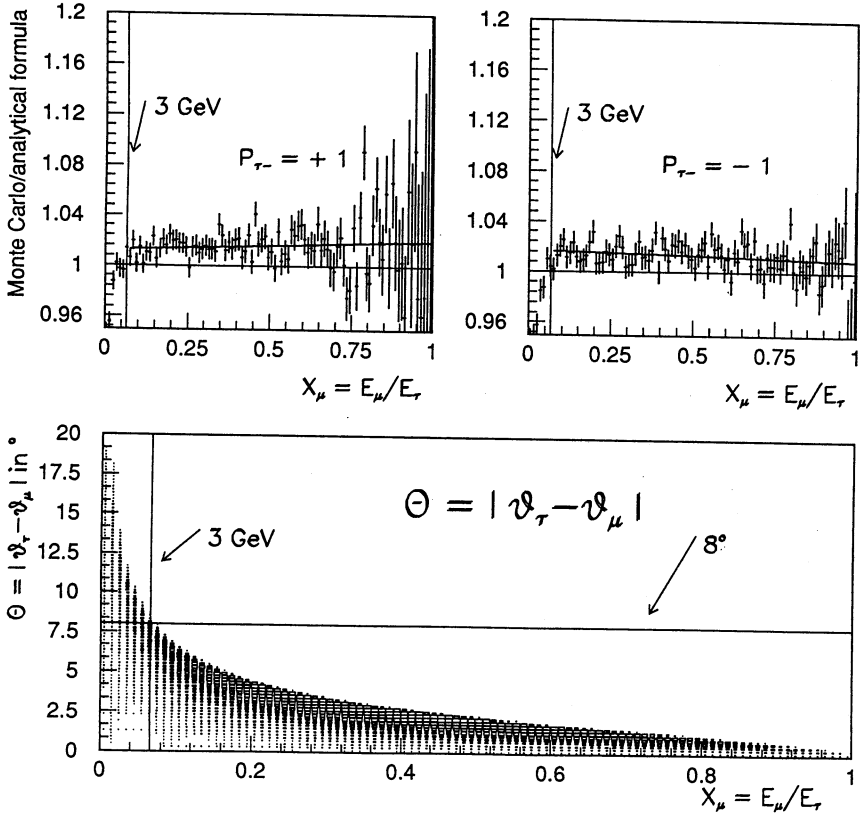


Figure A.1: Ratio Monte Carlo distribution over analytical formula for $p = +1$ (top left) and $p = -1$ (top right) together with a straight line fit and maximum deviation of the polar angle of the muon from the polar angle of the τ (bottom).

The approximations do not describe the Monte Carlo distribution below $x = 0.067$ very well. However, applying a straight line fit above 0.067 the slopes are zero within

<i>fit to</i> $a + bx$	$p = +1$	$p = -1$
a	1.013 ± 0.002	1.017 ± 0.002
b	0.007 ± 0.006	-0.008 ± 0.005

Table A.1: *Constants for straight line fit to ratio of Monte Carlo distribution and analytical formula (compare with figure A.1).*

less than two standard deviations. Still there may be a bias if the constant is different for $p = +1$ and $p = -1$. But they are in agreement within two standard deviations as well (all values see table A.1). Therefore the approximations (i) and (ii) do not introduce a bias as long as only energies above 0.067 (which corresponds to roughly 3 GeV) are considered.

To check whether approximation (iii) can be justified, the Θ distribution is shown in figure A.1 (bottom), where $\Theta = \theta_\mu - \theta_\tau$. For $x > 0.067$ the maximum deviation of the two angles is 8° —decreasing rapidly with higher x . That this can be safely neglected is shown by the results in section 2.6.6.

A.3 Formulas for Radiative Corrections

The equations for the description of the radiative corrections as a fragmentation process as shown in figure 2.12 are given in [25]. The initial-state bremsstrahlung distribution $\rho(v)$ is given by the second order sub-leading approximation with the proper resummation of soft photons:

$$\begin{aligned}
 \rho(v) &= \frac{e^{-C\gamma}}{\Gamma(1+\gamma)} e^{\Delta_{YFS}\gamma} v^{\gamma-1} (1 + \Delta_S + \Delta_H(v)), \\
 \Delta_{YFS} &= \frac{\alpha}{\pi} \left(\frac{1}{2}L - 1 + \frac{\pi^2}{3} \right), \quad \Delta_S = \frac{\alpha}{\pi} (L - 1) + \frac{1}{2} \left(\frac{\alpha}{\pi} \right)^2 L^2, \\
 \Delta_H(v) &= v \left(-1 + \frac{1}{2}v \right) + \frac{\alpha}{\pi} L \left\{ -\frac{1}{4}(4 - 6v + 3v^2) \ln(1 - v) - v \right\}, \\
 L &= \ln \frac{s}{m_e^2}, \quad \gamma = 2 \frac{\alpha}{\pi} (L - 1), \quad C = 0.57721566.
 \end{aligned} \tag{A.8}$$

The fragmentation functions D are given by

$$\begin{aligned}
D_\tau\left(\frac{m_\tau^2}{s(1-v)}, x\right) &= \delta(1-z) + \gamma_\tau d_\tau(z), \quad \gamma_\tau = \frac{\alpha}{\pi} \left(\ln \frac{s(1-v)}{m_\tau^2} - 1 \right), \\
d_\tau(z) &= \left(\frac{1}{1-z} \right)_+ + \frac{3}{4} \delta(1-z) - \frac{1}{2}(1+z), \quad \int_0^1 d_\tau(z) dz = 0, \\
D_\mu\left(\frac{m_\mu^2}{m_\tau^2}, z\right) &= \delta(1-z) + \gamma_\mu d_\mu(z), \quad d_\mu(z) = d_\tau(z), \\
\gamma_\mu &= \frac{\alpha}{\pi} \left(\ln \frac{m_\tau^2}{m_\mu^2} - 1 \right). \tag{A.9}
\end{aligned}$$

These fragmentation functions have to be used now for equation (2.43), from which the last three integrals are considered by defining general decay functions $H_i(x)$:

$$\begin{aligned}
H_i(x) &= \int_0^1 \frac{dz}{z} D_\tau\left(\frac{m_\tau^2}{s(1-v)}, x\right) \int_0^1 \frac{dt}{t} D_\mu\left(\frac{m_\mu^2}{m_\tau^2}, t\right) h_i\left(\frac{x}{zt}\right) \theta\left(1 - \frac{x}{zt}\right) \\
&= h_i(x) + \gamma_\tau \int_x^1 \frac{dz}{z} d_\tau(z) h_i\left(\frac{x}{z}\right) + \gamma_\mu \int_x^1 \frac{dz}{z} d_\mu(z) h_i\left(\frac{x}{z}\right), \tag{A.10}
\end{aligned}$$

where $h_i(x)$ are the non radiative decay functions as given in equation (2.28). This result is obtained by neglecting the term of order $\gamma_\tau \gamma_\mu$, which corresponds to the simultaneous photon emission from the τ and it's decay product. The final result, which is used for equation (2.44) is then:

$$\begin{aligned}
H_0^\mu(x) = & 2 - 6x^2 + 4x^3 + \frac{4}{9}\rho(-1 + 9x^2 - 8x^3) \\
& + (\gamma_\tau + \gamma_\mu) \left\{ (2 - 6x^2 + 4x^3) \ln(1 - x) \right. \\
& + \frac{4}{9}\rho(-1 + 9x^2 - 8x^3) \ln(1 - x) \\
& - (1 - 6x^2 + 4x^3) \ln x - \frac{4}{9}\rho\left(-\frac{1}{2} + 9x^2 - 8x^3\right) \ln x \\
& - \frac{1}{3} - x + 4x^2 - \frac{8}{3}x^3 \\
& \left. + \frac{4}{9}\rho\left(\frac{2}{3} + 2x - 8x^2 + \frac{16}{3}x^3\right) \right\}, \tag{A.11}
\end{aligned}$$

$$\begin{aligned}
H_1^\mu(x) = & -\frac{2}{3} + 4x - 6x^2 + \frac{8}{3}x^3 \\
& + \frac{4}{9}\delta(1 - 12x + 27x^2 - 16x^3) \\
& + (\gamma_\tau + \gamma_\mu) \left\{ \left(-\frac{2}{3} + 4x - 6x^2 + \frac{8}{3}x^3\right) \ln(1 - x) \right. \\
& + \frac{4}{9}\delta(1 - 12x + 27x^2 - 16x^3) \ln(1 - x) \\
& - \left(-\frac{1}{3} + 2x - 6x^2 + \frac{8}{3}x^3\right) \ln x \\
& - \frac{4}{9}\delta\left(\frac{1}{2} - 6x + 27x^2 - 16x^3\right) \ln x \\
& + \frac{7}{9} - \frac{5}{3}x + \frac{8}{3}x^2 - \frac{16}{3}x^3 \\
& \left. + \frac{4}{9}\delta\left(-\frac{5}{3} + 7x - 16x^2 + \frac{32}{3}x^3\right) \right\}. \tag{A.12}
\end{aligned}$$

B. Miscellaneous

B.1 Definition of CLASS 15

The analysis presented in this thesis is based on a preselection called the “CLASS 15” made by the ALEPH collaboration. This preselection allows one to look only at leptonic final states (e^+e^- , $\mu^+\mu^-$ or $\tau^+\tau^-$). The definition of events of this type in 1989 and 1990 is:

- look only at tracks which fulfill
 - o at least 4 TPC hits,
 - o $|Z_0| < 10\text{ cm}$ and
 - o $p > 0.1\text{ GeV}$.

Count the number of tracks separately for $|D_0| < 5\text{ cm}$ (including $|D_0| < 2\text{ cm}$) and for $|D_0| < 2\text{ cm}$.

- a) For *exactly* 2 of these tracks with $|D_0| < 5\text{ cm}$, those are declared as good tracks and the selection continues.
- b) If the number of these tracks with $|D_0| < 2\text{ cm}$ is between 2 and 8, those are declared as good tracks and the selection continues. Any track with $2\text{ cm} \leq |D_0| \leq 5\text{ cm}$ is declared as bad track.
- The event is divided into two hemispheres by the thrust axis calculated with a JETSET routine [59]. At least one good track per hemisphere is demanded.
- At least one track with $|D_0| < 2\text{ cm}$ is demanded to have $p > 3\text{ GeV}$.
- If there are more than 4 good tracks in the event, each of them is required to have an opening angle η with respect to the axis of the corresponding jet with $\cos \eta > 0.85$.

B.2 Electron Identification

The electron identification in ECAL is based on two observables, which are used to discriminate electrons against hadrons (pions)¹. The first, R_2 , relates the energy deposit E_0 in the four towers closest to the extrapolated track to the momentum p determined in the TPC. The quantity $X = E_0/p$ has been measured with test-beam data and is found to be distributed gaussian for electrons with a mean $\langle X \rangle = 0.83$ for $p > 2\text{ GeV}$ independent of angle and momentum. The variance σ_X is parametrized as function of momentum using the test-beam data. The quantity R_2 is defined by

¹Muons need not to be considered as they interact only via the ionization process. Therefore the misidentification probability for muons is negligible.

$$R_2 \equiv \frac{X - \langle X \rangle}{\sigma_X}, \quad (\text{B.1})$$

which is normally distributed with zero mean and unit variance for electrons.

The second observable, R_3 , uses the longitudinal shower profile which is different for electrons and hadrons. It is defined by

$$R_3 \equiv \frac{A - \langle A \rangle}{\sigma_A}. \quad (\text{B.2})$$

The quantity A is the inverse of the mean position of the longitudinal energy deposit:

$$A \equiv \frac{E_0}{\sum_{i=1}^3 E_i S_i}, \quad (\text{B.3})$$

where E_i is the energy deposit in stack i of the four towers closest to the track². S_i is the mean longitudinal position of the shower in stack i . A parametrization of $\langle A \rangle$ and σ_A is obtained from the test beam data.

An electron is defined by the following conditions:

$$\begin{aligned} -3.0 &< R_2 \\ -2.4 &< R_3 < 3.0. \end{aligned}$$

For an explanation of the electron identification in greater detail and the corresponding plots, see [46]. The efficiency of the electron identification is $\approx 80\%$.

²Consequently $E_0 = \sum_{i=1}^3 E_i$.

C. Alignment of ITC and TPC

The ITC gives a very accurate measurement of the coordinates in the x-y plane (error on one coordinate about $100 - 180 \mu m$) and thus can help to improve the accuracy of the determination of the momentum by the TPC. Furthermore it helps to extrapolate hits into the MVD. Therefore a good relative alignment of TPC/ITC is necessary. The coordinate error due to misalignment clearly should be smaller than the measurement error. A geometrical alignment at the level of $200 \mu m$ is ensured by mechanical means [60, 61]. A higher precision is reached by using cosmic rays crossing TPC and ITC. Furthermore this kind of alignment ensures that some effects which distort a pure mechanical alignment (see e.g. section C.2) are taken into account properly. Alignment has been studied with the assumption of a perfect TPC earlier [62]. Aim of this new investigation is to modify the former procedure to study the effect of an imperfect TPC on alignment. Furthermore some of these imperfections can be measured with the help of the ITC.

C.1 Parameters and Basic Equations

Essentially the alignment is measured by comparing track parameters fitted independently in ITC and TPC. In this paper the TASSO convention is used (for the mathematical convention see [63]):

- D_0 closest distance of track to beam axis in x-y plane. Positive if origin is encircled, negative if not;
- Φ_0 angle of track with respect to the x-axis in the x-y plane at D_0 ; range 0 to 2π (for cosmic rays coming from above only π to 2π);
- Z_0 Z of track at D_0 ;
- λ dip angle with respect to the vertical at D_0 ; range $-\pi/2$ to $\pi/2$.

The relative position of two rigid bodies can be described by six parameters. These could be chosen to be three offsets along an orthogonal coordinate system and a rotation matrix parametrized by three Euler angles (most general assumption). For alignment purposes only very small deviations from two perfectly aligned bodies are expected (this is ensured by the mechanical alignment). So three rotational angles around fixed axis together with three offsets along these axis are chosen to describe misalignment. The definitions are given in figure C.1.

To determine the misalignment the track parameters are measured independently in ITC and TPC. Figure C.2 shows the effect of misalignment on D_0 .

$$\begin{aligned} \Delta D_0 &= [Q D_0]^{ITC} - [Q D_0]^{TPC} \\ &= \Delta X \sin \Phi_0 - \Delta Y \cos \Phi_0, \end{aligned} \tag{C.1}$$

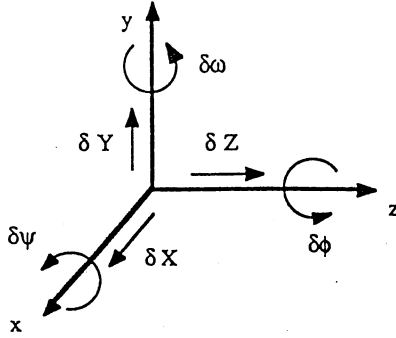


Figure C.1: Definition of alignment constants.

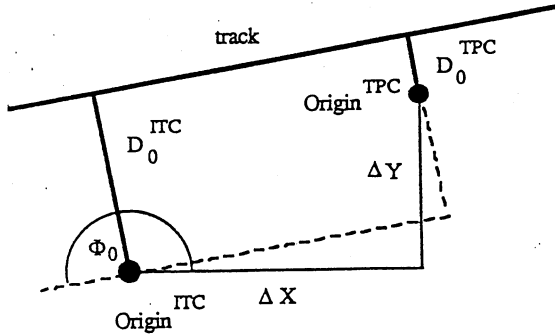


Figure C.2: Effect of misalignment on D_0 .

where Q is positive if the track bends clockwise negative if it bends anticlockwise and ΔX , ΔY are given by

$$\begin{aligned}\Delta X &= \delta X + Z_0 \delta \omega \\ \Delta Y &= \delta Y - Z_0 \delta \psi.\end{aligned}\tag{C.2}$$

As the resolution in Z_0 of the ITC is very poor (around 3 cm), Z_0 is taken from the TPC. An alignment in Z_0 is furthermore not carried out as Z_0 will not be measured for cosmics in the ITC. Φ_0 is measured by the TPC as well because of the longer lever-arm. Combining equations (C.1) and (C.2) leads to

$$\Delta D_0 = (\delta X + Z_0 \delta \omega) \sin \Phi_0 - (\delta Y - Z_0 \delta \psi) \cos \Phi_0,\tag{C.3}$$

which is considered as the basic equation for this procedure. To determine the fifth parameter the Φ_0 information of both detectors with a small dip angle λ dependent

correction (see figure C.3, there only the effect of one angle— $\delta\omega$ —is taken into account) is used:

So, $\delta\Phi_0$ is completely decoupled from D_0 .

$$\delta\Phi = \Phi_0^{TPC} - \Phi_0^{ITC} + \tan\lambda(\delta\omega \sin\Phi_0 - \delta\psi \cos\Phi_0). \quad (C.4)$$

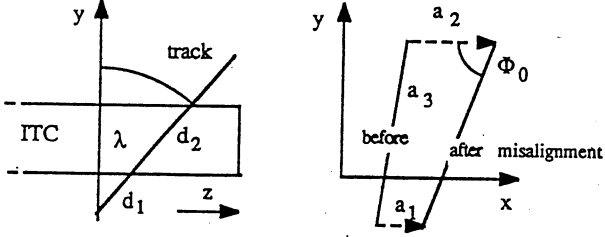


Figure C.3: Correction in Φ_0 due to a nonzero dip angle λ , where

$$\begin{aligned} a_1 &= \delta\omega d_1 \sin\lambda, \\ a_2 &= \delta\omega (d_1 + d_2) \sin\lambda, \\ a_3 &= d_2 \cos\lambda \quad \text{and therefore} \\ \Delta\Phi_0 &= (a_2 - a_1) \sin\Phi_0 / a_3 = \delta\omega d_2 \sin\lambda \sin\Phi_0 / d_2 \cos\lambda = \delta\omega \tan\lambda \sin\Phi_0. \end{aligned}$$

C.2 Imperfections of the TPC

Here the major known imperfections of the TPC are considered which are linearly dependent on z and may be different in the two halves of the TPC. Examples for these imperfections are (only these are used for the simulation):

- a nonzero angle between the E- and B-field (both are assumed to be homogenous), in called BnpE (B not parallel E),
- a nonzero twist angle between the two TPC-halves.

To understand the effect of these imperfections the coordinate transformation induced by misalignment of the ITC is considered in equation (C.5).

$$\vec{r}_{true} \rightarrow \vec{r}_{true} + \begin{pmatrix} \delta X \\ \delta Y \\ \delta Z \end{pmatrix} + \begin{pmatrix} 0 & -\delta\Phi & \delta\omega \\ \delta\Phi & 0 & -\delta\psi \\ 0 & 0 & 0 \end{pmatrix} \vec{r}_{true}. \quad (C.5)$$

An angle between E- and B-field introduces nonzero x- and y-components of the drift velocity which are given by (see equation 3.2)

$$\Psi_x \equiv \frac{v_{drift}^x}{v_{drift}^z} = \frac{\omega\tau}{1 + (\omega\tau)^2} \{(\omega\tau)\cos\Phi - \sin\Phi\} \Psi,$$

$$\Psi_y \equiv \frac{v_{drift}^y}{v_{drift}^z} = \frac{\omega\tau}{1 + (\omega\tau)^2} \{(\omega\tau)\sin\Phi + \cos\Phi\} \Psi, \quad (C.6)$$

where Ψ and Φ are the azimuthal and polar angle of B relative to E. Ψ is expected to be in the order of mrad. The components Ψ_x and Ψ_y affect the drift in both halves of the TPC in a different way because E changes sign going from one half to the other. Therefore x and y of a hit are shifted by

$$x/y_{true} \rightarrow x/y_{true} - \left(\frac{Z - s_Z Z_{end}}{v_Z^{drift}} \right) v_{x/y_{true}}^{drift}, \quad (C.7)$$

where s_Z is the sign of Z.

At last the twist angle Φ^T of the two TPC halves has to be taken into account. It changes the coordinates according to

$$x/y_{true} \rightarrow x/y_{true} \pm \Phi^T a_Z y/x_{true}, \quad (C.8)$$

where $a_Z = (1 - s_Z)/2$. These imperfections lead to the following transformation in the TPC:

$$\vec{r}_{true} \rightarrow \vec{r}_{true} + \begin{pmatrix} \delta X \\ \delta Y \\ 0 \end{pmatrix} s_Z Z_{end} + \begin{pmatrix} 0 & \Phi^T a_Z & -\Psi_x \\ -\Phi^T a_Z & 0 & -\Psi_y \\ 0 & 0 & 0 \end{pmatrix} \vec{r}_{true}. \quad (C.9)$$

Comparing equation (C.5) and (C.9) it is clear that both transformations have exactly the same structure looking at one TPC half only. So in half A ($Z_0 > 0$)

$$\begin{aligned} \delta X_A &= \delta X + \Psi_x Z_{end} \\ \delta Y_A &= \delta Y + \Psi_y Z_{end} \\ \delta \omega_A &= \delta \omega - \Psi_x \\ \delta \psi_A &= \delta \psi + \Psi_y \\ \delta \Phi_A &= \delta \Phi \end{aligned}$$

$$\begin{aligned} \text{and in half B} \quad \delta X_B &= \delta X - \Psi_x Z_{end} \\ \delta Y_B &= \delta Y - \Psi_y Z_{end} \\ \delta \omega_B &= \delta \omega - \Psi_x \\ \delta \psi_B &= \delta \psi + \Psi_y \\ \delta \Phi_B &= \delta \Phi - \Phi^T \end{aligned} \quad (C.10)$$

would be measured. So, by dividing the TPC into two parts during aligning the ITC it is possible to measure any transformation linearly dependent on z and differing in both TPC halves induced by any effect whatsoever.

C.3 Strategy

As shown in section C.2 linear z-dependent imperfections in the TPC which may be different in the two halves have to be taken into account. Although some of them will be measured independently and the coordinates will be corrected for before alignment, the accuracy of these corrections may either not be sufficient or unknown imperfections of the above kind will distort alignment. Therefore it is essential for alignment to consider the TPC as two independent detectors. This means $2 * 5$ alignment constants are measured. These are the coefficients of two linear transformations which have to be applied in each half. Clearly these $2 * 5$ constants are most probably not the same as the geometrical alignment constants but are dominated by distortion effects. So, "alignment" in this thesis means: Find a set of "alignment" constants which gives you a linear transformation to correct the coordinates so that the relative alignment of TPC/ITC as seen by electronics/reconstruction program is correct. It is shown in section C.2 that any linear z-dependent distortion is taken into account if the TPC is divided into two halves.

Three possible schemes to incorporate alignment corrections into the offline analysis are: (1) Fix TPC A (B), correct ITC, correct TPC B (A). This alternative means that TPC A (B) defines the ALPEH coordinate system. Coordinates of both detectors have to be corrected. (2) Fix TPC, divide ITC into two halves and correct ITC A and ITC B. Here the TPC is forced to be a unit - the coordinate system of ALEPH would therefore be some kind of 'mean' of the two systems TPC A & TPC B. (3) Fix ITC, correct TPC A, correct TPC B. The ALPEH coordinate system would then be defined by the ITC. A mixture of alternative (1) and (3) has been chosen: correct for the BnpE effect with Ψ_x and Ψ_y , then continue with scheme (1).

C.4 Simulation

Cosmics have been generated with a simple μ -generator [64] flat in energy between 2 and 20 GeV. The starting point of the track is distributed flat between $-200\text{ cm} < z < 200\text{ cm}$ at the upper edge of the TPC. The Φ_0 range stretches (flat) from $-\pi/4$ to $\pi/4$ against the vertical. A second point of the track is then chosen at $y = 0$, flat between $-100\text{ cm} < z < 100\text{ cm}$ (ITC) and flat between $-R_{ITC} < x < R_{ITC}$. Samples of 10000 events have been generated with GALEPH V 2.01 with different sets of alignment constants. The track elements in the ITC were modified according to these constants before digitizing. Then TPCSIM V 2.04 was used to allow a more reliable study of TPC effects. TPC imperfections were introduced at the reconstruction level.

C.5 Reconstruction

In this section the reconstruction chain except for the determination of the alignment constants is described.

C.5.1 ITC Reconstruction

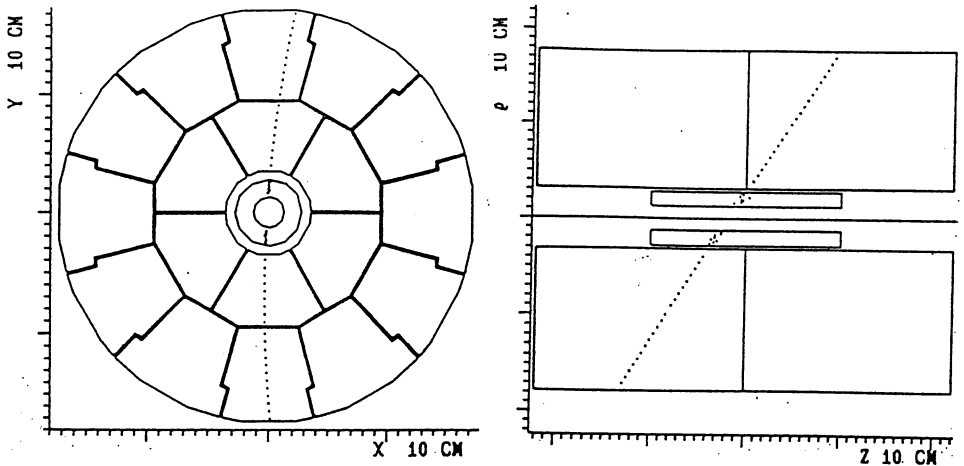


Figure C.4: *Typical cosmic event.*

In [62] merely the influence of ITC digitization on straight tracks is studied. But approaching reality the reconstruction of curved tracks has to be allowed, as tracks with momentum well below 10 GeV are used. It is also not possible to use the standard JULIA reconstruction, because the ITC gives only drift-time measurement, i.e. the distance from a sense wire which defines a circle in the (x, y) plane. For e^+e^- this does not really matter because the knowledge that the tracks are coming from the vertex reduces the circle to two points—a simple ambiguity, easily to be resolved. For alignment with cosmic most of the tracks do not cross the beamline (see figure C.4). So a similar procedure as described in [62] has to be applied, allowing the reconstruction of curved tracks:

- take position of wires and fit circle giving large weights to short drift times ($w = 1/(d^2 + d_0^2)$) to find the position on the drift circles for longer drifts correctly.
- take these position and fit now giving large weights to long drift times ($w = d^2$) to find the positions on the drift circles for shorter drifts.

With these positions the standard fit (UFITMS in JULIA, [63]) is performed.

Due to the curvature of tracks some constellations are causing problems, e.g.: Only long drifts in the upper half of the ITC, only short drifts in the lower half sometimes leads to a wrong fit result which is clearly visible by looking at the maximum residual. So a cut at $500 \mu\text{m}$ for the largest residual is applied which cures the problem and kills only 1% of all good events. The probability distribution for the track fit is shown in C.5. The spike at low probabilities is due to effects like bremsstrahlung or multiple scattering and is cut away with a $\chi^2/d.o.f.$ cut at 2.

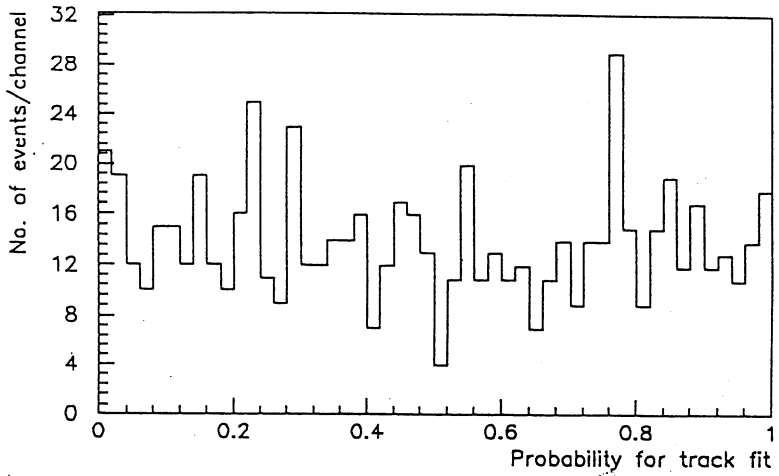


Figure C.5: *Probability distribution for ITC track fit.*

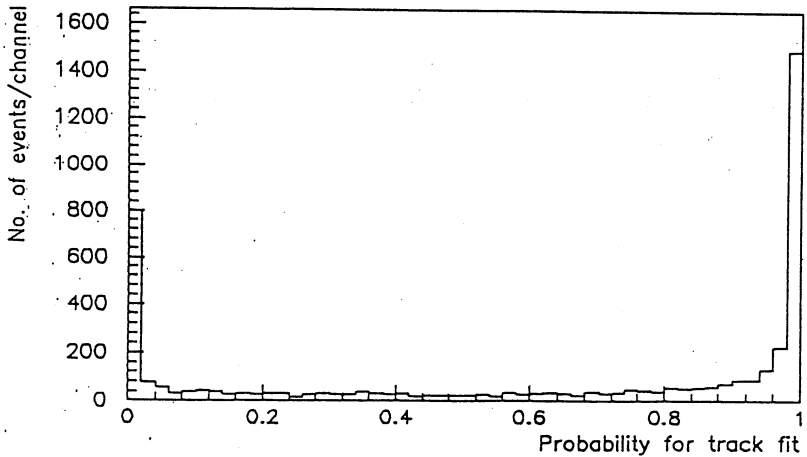


Figure C.6: *Probability distribution for TPC track fit.*

C.5.2 TPC Reconstruction

For reasons mentioned in section C.2 it is necessary to use information coming from one TPC half only. One way would be to use only tracks which cross only one half at all. But clearly this reduces statistics too much. So the hits of one track on each side are counted and the half in which more hits are found is chosen whereas the other hits are thrown away. Then the standard fit (UFITMS) without multiple scattering is performed. For TPCSIM the probability distribution for the track fit shows a peak at 1 which gives a hint to a problem concerning coordinate errors in JULIA (see figure C.6).

C.5.3 Cuts

Cuts are listed here for completeness although some of them will be explained later.

- $22 \leq \text{no. of hits in TPC} \leq 42$ (explanation in section C.6.1),
- no. of hits in ITC = 16 for best quality of tracks,
- maximum residual in ITC $< 500 \mu\text{m}$ (see above),
- $\chi^2/d.o.f.$ for TPC fit ≤ 2 track quality, excluding e.g. bremsstrahlung,
- $\chi^2/d.o.f.$ for ITC fit ≤ 2
- $|D_0| < 5 \text{ cm}$ see section C.6.1,
- $p > 6 \text{ GeV}$ see section C.6.1.

C.6 Results on Monte Carlo

In this section the studies made with simulated cosmic rays are presented.

C.6.1 Determination of Alignment Constants

As shown in section C.1, $\delta\Phi_0$ is decoupled from the other four parameters. So it is sufficient to determine four parameters (δX , δY , $\delta\omega$, $\delta\psi$) independently per half. But it was not possible to use the old alignment procedure [62] for this purpose. This was because the $\langle z \rangle$ (mean over z for one half) does not vanish as it is the case for the whole TPC. This fact introduces strong correlations between each offset and the corresponding tilt angle. The former procedure could not handle these correlations and lead to wrong results with respect to the errors. To get things right a χ^2 -fit (using MINUIT) for the four parameters has to be performed. For the fifth parameter the term on the right hand side of equation (C.4) is calculated for each track. This value is filled into a histogram to measure mean and the error. As $\delta\Phi_0$ is (nearly) decoupled from any other parameter this leads to the right result. The basic equation for the χ^2 -fit is equation (C.3) which leads to

$$\chi_{fit}^2 = \sum_{i=1}^n \frac{f^2(\Delta D_{0,i}, \Phi_{0,i}, z_{0,i})}{\sigma^2(D_{0,i}, \Phi_{0,i}, z_{0,i})}, \quad \text{with}$$

$$f(\Delta D_{0,i}, \Phi_{0,i}, z_{0,i}) = \Delta D_0 - \{(\delta X \sin \Phi_0 - \delta Y \cos \Phi_0) + Z_0(\delta \omega \sin \Phi_0 + \delta \psi \cos \Phi_0)\}, \quad \text{and}$$

$$\sigma^2(D_0, \Phi_0, Z_0) = \sum_{k,l=1}^4 \frac{\partial f}{\partial x_k} C_{k,l} \frac{\partial f}{\partial x_l} + \sigma_{D_0}^2, \quad (\text{C.11})$$

where n is the number of tracks, $\mathbf{x} = (\delta X, \delta Y, \delta \omega, \delta \psi)$ and $C_{k,l}$ is the covariance matrix coming from the track fit.

This fit is performed independently in each half and a comparison with the true values is made. Results for two different sets of alignment constants are shown in table C.1 which gives an impression how well the procedure works.

Now some problems and cuts which have to be applied are discussed:

Multiple Scattering

The multiple scattering angle is not fitted as it is rather difficult to use this information for alignment. This clearly causes a rise in χ^2 for the fit. To reduce the influence a momentum cut is applied (see table C.2) for the influence of multiple scattering and this cut). For all results given in this note a cut at 6 GeV is applied which is a compromise between loss in statistics and gain in quality. Furthermore there is one fact which helps to suppress the effect of multiple scattering: If the track fit in the TPC includes hits before and after traversing the ITC it measures some kind of 'mean' for the track parameters. But the ITC is measuring as well some kind of 'mean' with respect to multiple scattering as it lies inbetween the TPC. Therefore it is essential to demand at least one hit in the TPC after traversing the ITC for the track fit. This means the number of hits in the TPC must be at least 22 and not more than 42. But even after switching off multiple scattering some distortions are left which can be seen from table C.3. While $\chi_{deviation}^2$ decreases substantially χ_{fit}^2 does not change very much. This hints to an additional different problem, which is discussed next.

Coordinate Reconstruction Problems

After switching from simple coordinate smearing as done in GALEPH to (fast) TPCSIM the quality of the fit became very poor. Looking at figure C.7 it can be seen that for large $|D_0|$ the distribution of $D_0^{GALEPH} - D_0^{TPCSIM}$ becomes broader (see figure C.7) and has longer tails. This is most probably due to the fact that the coordinate finding algorithm(s) in JULIA is built to handle tracks coming from the vertex. But tracks with large $|D_0|$ for example do not look like coming from the vertex as they cross the padrow not under 90° which is assumed by the coordinate finding algorithms. Therefore tracks with $|D_0| > 5 \text{ cm}$ are excluded from the analysis. Examples for data reduction due to cuts are shown in table C.4.

Parameter	TPC ($Z_0 < 0$) measured	true	TPC ($Z_0 > 0$) measured	true
Set I				
$\delta X_{B/A}$ [μm]	-432 ± 22	-445	71 ± 20	45
$\delta Y_{B/A}$ [μm]	-4231 ± 49	-4280	5125 ± 43	5080
$\delta\omega_{B/A}$ [μrad]	231 ± 38	198	139 ± 35	198
$\delta\psi_{B/A}$ [μrad]	1680 ± 83	1750	1868 ± 75	1750
$\delta\Phi_{B/A}$ [μrad]	-812 ± 39	-800	-617 ± 42	-600
χ^2_{fit}	$437/313 = 1.40$		$555/332 = 1.67$	
$\chi^2_{\text{deviation}}$	$2.31/5$		$6.78/5$	
Set II				
$\delta X_{B/A}$ [μm]	1425 ± 22	1443	-2215 ± 19	-2243
$\delta Y_{B/A}$ [μm]	2437 ± 43	2493	-3552 ± 39	-3493
$\delta\omega_{B/A}$ [μrad]	340 ± 38	368	341 ± 33	368
$\delta\psi_{B/A}$ [μrad]	-1025 ± 74	-1147	-1245 ± 65	-1147
$\delta\Phi_{B/A}$ [μrad]	1446 ± 24	1400	974 ± 26	1000
χ^2_{fit}	$462/340 = 1.35$		$547/353 = 1.55$	
$\chi^2_{\text{deviation}}$	$7.62/5$		$6.65/5$	

Table C.1: Fit of alignment constants to Monte Carlo simulation (χ^2_{fit} gives the $\chi^2/\text{d.o.f}$ for the fit over all tracks, $\chi^2_{\text{deviation}}$ the deviation from the input parameters including correlations). The input values were:

Set I ITC misalignment: $\delta X = -200 \mu\text{m}$, $\delta Y = 400 \mu\text{m}$,
 $\delta\omega = 300 \mu\text{rad}$, $\delta\psi = -200 \mu\text{rad}$,
 $\delta\Phi_0 = -600 \mu\text{rad}$,

TPC imperfections: $\Phi^T = 200 \mu\text{rad}$, $\delta\psi = 2000 \mu\text{rad}$,
 $\Phi = 1300 \mu\text{rad}$.

Set II ITC misalignment: $\delta X = -400 \mu\text{m}$, $\delta Y = -500 \mu\text{m}$,
 $\delta\omega = -400 \mu\text{rad}$, $\delta\psi = 100 \mu\text{rad}$,
 $\delta\Phi_0 = 1000 \mu\text{rad}$,

TPC imperfections: $\Phi^T = -400 \mu\text{rad}$, $\delta\psi = 1500 \mu\text{rad}$,
 $\Phi = 800 \mu\text{rad}$.

Cut value (GeV)	χ^2_{fit} half A and B		$\chi^2_{\text{deviation}}$ half A and B	
2	$718/439 = 1.64$	$802/439 = 1.83$	$10.08/5$	$5.55/5$
6	$462/340 = 1.35$	$547/353 = 1.55$	$7.62/5$	$6.65/5$
10	$270/220 = 1.23$	$365/237 = 1.54$	$6.81/5$	$5.37/5$

Table C.2: Influence of multiple scattering and momentum cut.

	χ^2_{fit} half A and B		$\chi^2_{deviation}$ half A and B	
multiple scattering	437/313 = 1.40	555/332 = 1.67	2.31/5	6.78/5
no multiple scattering	454/333 = 1.36	507/352 = 1.44	1.63/5	4.03/5
doubled statistic	1733/636 = 2.72	1858/656 = 2.83	10.90/5	11.99/5

Table C.3: Comparison multiple scattering, no multiple scattering and higher statistics.

Cut	Number of events lost	
	Set I (all: 6927)	Set II (all: 6961)
TPC reconstruction failure	91	80
$22 \leq \text{number of TPC hits} \leq 42$	2451	2415
$2\chi^2/d.o.f. < 2$ for trackfit in TPC	527	469
$p \geq 6 \text{ GeV}$	805	845
$D_0 < 5 \text{ cm}$	2294	2368
number of ITC hits = 16	103	79
ITC residual cut	7	8
$2\chi^2/d.o.f. < 2$ for trackfit in ITC	527	469

Table C.4: Data reduction for Monte Carlo samples.

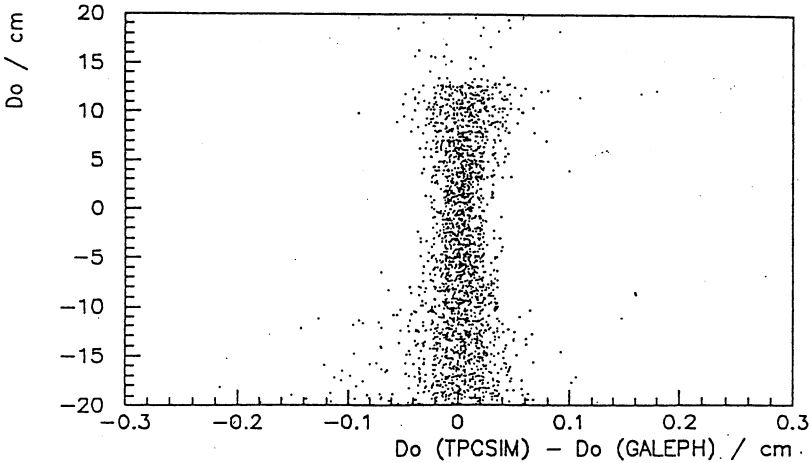


Figure C.7: $D_0^{GALEPH} - D_0^{TPCSIM}$ versus D_0 .

Parameter	measured value—SET I	true	measured value—SET II	true
δX [μm]	-181 ± 15	-200	-395 ± 15	-400
δY [μm]	447 ± 32	400	-557 ± 29	-500
$\delta\omega$ [μrad]	290 ± 27	300	-418 ± 26	-400
$\delta\psi$ [μrad]	-176 ± 57	-200	113 ± 51	100
$\delta\Phi$ [μrad]	-617 ± 42	-600	974 ± 26	1000
Φ^T [μrad]	195 ± 58	200	-472 ± 36	-400
Ψ_x [10^{-6}]	105 ± 6	102	-758 ± 6	768
Ψ_y [10^{-6}]	1949 ± 14	1950	-1248 ± 12	-1247
$\chi^2_{\text{deviation}}$	4.5/8		12.2/8	

Table C.5: *Interpretation of alignment constants in terms of imperfections and geometrical alignment.*

	TPCSIM	no TPCSIM
mult. scattering	$\langle x \rangle = +0.47 \pm 0.06$ $\sigma = 1.8$	$\langle x \rangle = +0.17 \pm 0.06$ $\sigma = 2.4$
no mult. scattering	$\langle x \rangle = +0.44 \pm 0.04$ $\sigma = 1.1$	$\langle x \rangle = -0.06 \pm 0.03$ $\sigma = 1.0$

Table C.6: *Mean value and width of $x = (D_0 - D_0^{\text{true}})/\sigma_{D_0}$ ($|D_0| < 5 \text{ cm}$, $p > 6 \text{ GeV}$).*

C.6.2 Measuring Imperfections

The procedure outlined above results in $2 * 5$ constants for a linear transformation. If it is guaranteed (e.g. by independent measurements) that no distortions but the one described in section C.2 are present in the TPC, equation (C.10) can be inverted to get the geometrical alignment constants and the parameters describing the distortions. For the two samples given in table C.1 this has been done and the results can be found in table C.5. It should be stressed that under the assumptions given in this paragraph these imperfections are measurable to a remarkably high degree of accuracy ($v_x^{\text{drift}}/v_y^{\text{drift}}$ to about 10^{-5}) compared e.g. to the measurements of the laser calibration system. But clearly it will be very difficult to show that no other distortions are present which is essential to interpret these constants in this way.

C.6.3 Systematic Effects

To check the error given by UFITMS the expectation value of mean and rms-width of the distribution $(D_0 - D_0^{\text{true}})/\sigma_{D_0}$ have been calculated with and without multiple scattering (MS & NMS) and with and without TPCSIM. Numbers are given in table C.6. For 'perfect' errors a gaussian distribution with mean 0 and width 1 is expected. There exists a bias using TPCSIM - the origin of this bias may be related to the coordinate reconstruction problem. Using NMS the width becomes more realistic and thus gives some confidence in these alignment measurements (MS only broadens but does not bias distributions). On the other hand the width of about 2 shows that the systematic error due to MS and coordinate reconstruction problems (and other possible distortions) is not

Parameter	Results 1989	Results 1991
δX [μm]	1230 ± 100	520 ± 30
δY [μm]	-340 ± 190	-10 ± 70
$\delta\omega$ [μrad]	40 ± 180	340 ± 60
$\delta\psi$ [μrad]	220 ± 360	-180 ± 70
$\delta\Phi$ [μrad]	-400 ± 150	-320 ± 60
Φ^T [μrad]	-30 ± 180	-70 ± 160
Ψ_x [10^{-6}]	-440 ± 40	-407 ± 12
Ψ_y [10^{-6}]	340 ± 90	390 ± 30
$\chi^2_{fit}/d.o.f$	238/110	1810/1131

Table C.7: Measured alignment constants for 1989 and 1991 [66].

negligible. To check its influence a sample of 20000 events has been generated. The χ^2 values are shown in table C.3. It is clear that the error is more and more dominated by systematics not taken into account for the fit and thus the χ^2 increases. Therefore the errors given for this special sample may give an estimate of 50% for the systematic error. For the moment this leads to an estimate of 25% systematic error relative to the error given by the sets with the usual amount of data (about 700 useful events). This as well reduces the χ^2 of the MINUIT fit to roughly 1 for these samples.

C.7 Results on Data

If a very pessimistic acceptance of 10% for the cosmics is assumed and the number $0.35 m^{-2} s^{-1}$ for the muon flux/horizontal area for $p_\mu > 10 GeV$ [65] is taken, about 2 days of running is needed to collect about 1000 useful events assuming a D_0 range of [-5 cm, 5 cm].

C.7.1 Alignment 1989

The running conditions for the cosmic run in 1989 were not perfect. This was related to problems concerning trigger, readout and performance of the subdetectors. In total 110 cosmic rays were used for the alignment procedure. The results are given in table C.7.

As it can be seen from table C.7 the accuracy of the method and the quality of the actual fit has suffered from the rather poor running conditions. Nevertheless the procedure was used to correct for two important and rather large effects: The *offset in x* was determined to be over 1 mm. This is an effect which has not been seen surveying the ITC after insertion of the TPC. In [61] an offset δX of roughly 100 μm was seen. During the running of ALEPH the alignment constants δX , δY and $\delta\Phi$ were determined with e^+e^- and $\mu^+\mu^-$ leptonic final states. These measurements verified the large value for δX . The second important effect was the *angle between electric and magnetic field*. Even with the rather low statistic quite accurate results have been obtained. The values Ψ_x and Ψ_y were used throughout the whole running period 1989 and 1990 because it was not possible

to measure them by other means with the same accuracy. In principle the laser system can be used to get these components, but the accuracy is poorer by roughly a factor of ten. Interpreting these relative transverse drift components as manifestation of an angle between the magnetic and electric field (the latter pointing in the direction of the z -axis) yields an angle of 0.03° [39].

C.7.2 Alignment 1991

The alignment in 1991 became necessary as the ITC has been removed to allow the insertion of the mikrovertex detector. The quality and the statistics of the cosmic muons taken for the alignment were much better than in 1989. The results [66] from 1131 tracks from cosmic muons are shown in table C.7. The transverse drift velocity components agree with those in 1989. This is expected as neither the TPC nor the magnetic field have been changed. The alignment constants were expected to be different to those in 1989.

C.8 Conclusions

A procedure used to align ITC, TPC A and TPC B relative to each other has been set up. A twist angle between half A and B and every linear z -dependent distortion (which may be different in the two halves) are taken into account and are measured. The general scheme consists of measuring the five coefficients of two linear transformations to be applied for $z > 0$ and $z < 0$. The accuracy to which each of this coefficient is measured with about 1000 useful events ensures a relative alignment of TPC A / ITC / TPC B to better than $100 \mu\text{m}$. The systematic error due to multiple scattering and coordinate reconstruction problems in the TPC is estimated to be about 25% of the statistical error for this amount of data.

The actual alignment in 1989 and 1991 was determined with this procedure. The corresponding relative drift velocity components and the alignment twist angles are used throughout the whole running period. The actual alignment offsets are remeasured with low multiplicity events (e.g. $\mu^+\mu^-$ events) later in the running period. In 1991 the improvement in quantity and quality was remarkable.

Bibliography

- [1] H. Becquerel, *C.R. Acad. Sci. (Paris)* **122** (1896) 501.
- [2] E. Fermi, *Ricerca Scient.* **2**, Heft 12 (1933);
E. Fermi, *Z. Phys.* **88** (1934) 161.
- [3] Particle Data Group, *Phys. Lett.* **B239** (1990).
- [4] C.S. Wu et al., *Phys. Rev.* **105** (1957) 1413.
- [5] S. Glashow, *Nucl. Phys.* **22** (1961) 579;
A. Salam, in *Elementary Particle Theory*, ed. H. Svartholm
(Almquist, Stockholm, 1968) 367;
S. Weinberg, *Phys. Rev. Lett.* **19** (1967) 1264.
- [6] F.J. Hasert et al., *Phys. Lett.* **B46** (1973) 138;
F.J. Hasert et al., *Nucl. Phys.* **B73** (1974) 1.
- [7] P.W. Higgs, *Phys. Lett.* **12** (1964) 132;
P.W. Higgs, *Phys. Rev. Lett.* **13** (1964) 508;
P.W. Higgs, *Phys. Rev.* **145** (1966) 1156.
- [8] T.W. Kibble, *Phys. Rev.* **155** (1967) 1554.
- [9] G. t'Hooft, *Phys. Lett.* **B37** (1971) 195.
- [10] G. Arnison et al. (UA1 Collaboration), *Phys. Lett.* **B126** (1983) 398.
- [11] P. Bagnaia et al. (UA2 Collaboration), *Phys. Lett.* **B129** (1983) 130.
- [12] P. Shalbach et al. (CDF Collaboration), proceedings of the APS conference, Washington DC, April 1990.
- [13] J. Alitti et al. (UA2 Collaboration), *Phys. Lett.* **B241** (1990) 150.
- [14] G.S. Abrams et al. (MARK II Collaboration), *Phys. Rev. Lett.* **63** (1989) 724.
- [15] F. Dydak, "Results from LEP and the SLC", **CERN-PPE 91-14**, Preprint (1991).
- [16] D. Decamp et al. (ALEPH Collaboration), **CERN-PPE 91-19**, Preprint (1991).
- [17] K. Sliwa (CDF Collaboration), in *Proceedings of the Twenty-Fifth Recontres de Moriond, March, 1990*, edited by J. Tran Thanh Van (Editions Frontieres, Gif-sur-Yvette, 1990).
- [18] "Improved Measurements of Electroweak Parameters from Z Decays into Fermion Pairs" ALEPH Collaboration, to be published in 1991, first draft available.

- [19] M.Perl et al., *Phys. Rev. Lett.* **35** (1975) 1489.
- [20] M.Perl, *Ann. Rev. Nucl. Part. Sci.* **30** (1980) 299.
- [21] H. Albrecht et al. (ARGUS Collaboration), *Phys. Lett.* **B246** (1990) 278; Number averaged with [3].
- [22] "Measurement of the Polarization of τ Leptons Produced in Z Decays", D. Decamp et al. (ALEPH Collaboration), **CERN-PPE 91-94**, Preprint (1991).
- [23] E. Locci, M. Martinez and R. Tanaka, "Lepton Forward-Backward Charge Asymmetry Fit Result", internal ALEPH-note, 22.4.1991; the results used from this reference are identical to the ones in [18] except for not using the τ polarisation constraint from [22]; (the numbers of the most recent revised version of this note, 91-76, differ only slightly from the ones used in this thesis).
- [24] S. Odaka, Talk given at the Orsay τ workshop, Sept. 1990; see also **KEK 90-164**, Preprint (1990).
- [25] G. Altarelli et al. (editors), Z Physics at LEP, **CERN 89-08 Volume 1** (1989) 235-265; and *Erratum* from 8 March 1990; (The sign for p given in equation 2.1 and 2.6 is wrong).
- [26] G. Altarelli et al. (editors), Z Physics at LEP, **CERN 89-08 Volume 1** (1989) 7-54.
- [27] K. Abe et al., *Phys. Rev. Lett.* **62** (1989) 1709.
- [28] J. Dorenbusch et al. (CHARM Collaboration), *Z. Phys. C — Particles and Fields* **41** (1989) 567.
- [29] R.C. Allen et al., *Phys. Rev. Lett.* **64** (1990) 1330.
- [30] F. Scheck, *Phys. Rep.* **44** (1978) 187-248.
- [31] A. Rougé, *Z. Phys. C — Particles and Fields* **48**, (1990) 75.
- [32] A. Rougé, "Tau Polarization Measurement in the $\tau \rightarrow \rho\nu$ Decay Mode", ALEPH-note 88-15, 1988.
- [33] A. Rougé, Talk given at the Orsay τ workshop, Sept. 1990.
- [34] C.A.Nelson, *Phys. Rev.* **D40** (1989) 123.
- [35] M. Martinez, ALEPH Collaboration, private communication.
- [36] G. Altarelli et al. (editors), Z Physics at LEP, **CERN 89-08 Volume 3** (1989) 69-77.
- [37] S. Jadach, Z. Was, "First and Higher Order Noninterference QED Radiative Corrections to the Charge Asymmetry at the Z Resonance" **MPI-PAE/PTh 33/89**, Preprint MPI München (1989).

- [38] D. Decamp et al. (ALEPH Collaboration), *Nucl. Instr. Meth.* **A294** (1990) 121-178.
- [39] W. Atwood et al. (ALEPH TPC group), **CERN-PPE 91-24**, Preprint (1991).
- [40] G.J. Barber et al., *Nucl. Instrum. Meth.* **A279** (1989) 212.
- [41] K. Kleinknecht, "Detektoren für Teilchenstrahlung", Teubner Verlag, Stuttgart 1984.
- [42] J. Richstein, Doktorarbeit Universität Dortmund, 1986.
- [43] L.A.T. Bauerdick, Doktorarbeit Universität Mainz, 1990.
- [44] St. Roehn, "Alignment of ITC/TPC", ALEPH-note 88-20 (1988).
- [45] T. Barczewski et al. (ALEPH TPC group), *Nucl. Instr. Meth.* **A289** (1990) 176.
- [46] D. Decamp et al. (ALEPH Collaboration), *Phys. Lett.* **B244** (1990) 551-565.
- [47] G. Hubricht et al., *Nucl. Instr. Meth.* **228** (1985) 327 and **A243** (1986) 495;
C. Raine et al., *Nucl. Instr. Meth.* **217** (1983) 305.
- [48] F. Ranjard et al., "ALEPH Monte-Carlo-Program Version 2.37", ALEPH-note 88-119 (1988).
- [49] F. Bruyant et al. 1987; GEANT3, CERN program library, CERN DD/EE/84-1.
- [50] S. Wasserbaech, "Size of the Luminous Region at LEP Interaction Point 4", ALEPH 91-57 (1991).
- [51] G. Bagliesi and L. Silvestris, "Tau Trigger: Comparison between 1989, 1990 Data and Monte Carlo", ALEPH-note 91-2 (1991).
- [52] G. Bagliesi and L. Silvestris, "Muon Trigger: Comparison between 1989, 1990 Data and Monte Carlo", ALEPH-note 90-81 (1990).
- [53] N.R. Keemer, "Single Cluster π^0 s in ECAL", internal ALEPH writeup (1990).
- [54] D. Decamp et al. (ALEPH Collaboration), *Z. Phys. C — Particles and Fields* **48** (1990) 365.
- [55] St. Roehn, A. Stahl, "Measurement of τ Polarisation in $\tau \rightarrow \mu\nu_\tau\nu_\mu$ Decays", ALEPH-note 90-26 (PHYSIC 91-25), the statistical error on P_{τ^-} is 12.9% rather than 11.8%.
- [56] H.J. Behrend et al., (CELLO Collaboration), *Phys. Lett.* **B127** (1983) 270.
- [57] W.T. Ford et al., (MAC Collaboration), *Phys. Rev.* **D36** (1987) 1971.
- [58] M.H. Lee et al. (AMY Collaboration), **KEK 90-70**, Preprint (1990).
- [59] "The Lund Monte Carlo Programs", long writeup, CERN Pool programs W5035/W5045-W5048, 1.11.1989.
- [60] R.W. Forty, "Survey of the ITC", ALEPH-note, 28.06.1988.

- [61] R.W.Forty, "Assembly of the ITC and TPC", internal ALEPH publication, ALEPH 89-21.
- [62] R.W.Forty, "Alignment of the ITC", ALEPH-note 87-15.
- [63] L.Garrido, "Track Fitting with Multiple Scattering", ALEPH-note 88-11.
- [64] Subroutine written by R. Beuelinck.
- [65] H.Wachsmuth, "An Estimate of the Cosmic Muon Intensity at ALEPH", ALEPH-note 87-12.
- [66] D. Colling and B. Wolf, "First Result of the ITC/TPC Alignment from the 1991 Cosmic Run", ALEPH-note 91-65 (TPCGEN 91-2).

List of Figures

2.1	Vertex of Z^0 going into fermion-antifermion	7
2.2	Total Born cross-section versus s	10
2.3	A_{pol} as a function of $\cos\theta$ and A_{pol} , A_{FB} and A_{pol}^{FB} as function of the center-of-mass energy	12
2.4	$\tau^- \rightarrow \pi^- \nu$ in center-of-mass system	15
2.5	$\tau^- \rightarrow \mu^- \nu \nu$ in the τ rest frame	16
2.6	Momentum spectrum of muons from τ decays for polarizations $0, \pm 1$	17
2.7	Sensitivity S for the different decay channels	18
2.8	QED corrections to $e^+e^- \rightarrow \tau^+\tau^-$	24
2.9	Propagator corrections to $e^+e^- \rightarrow \tau^+\tau^-$	24
2.10	Vertex corrections and box contributions to $e^+e^- \rightarrow \tau^+\tau^-$	24
2.11	Size of electroweak radiative corrections	26
2.12	Radiative corrections as a chain of fragmentation processes	31
2.13	A_{pol} , A_{FB} and A_{pol}^{FB}	32
2.14	Comparison of the functions $W_i(s, x)$	34
2.15	Momentum spectrum for muon for the Standard Model value of P_{τ^-}	35
3.1	Integrated luminosity versus time	40
3.2	The ALEPH Detector	42
3.3	An ITC drift cell	44
3.4	The TPC	47
3.5	Three different TPC sectors	47
3.6	The wire planes in the sectors	48
3.7	The laser calibration system	50
3.8	The hadronic and the electromagnetic calorimeter	53
3.9	The overlap region for the HCAL calorimeter	54
3.10	A $\tau^+\tau^-$ event in the ALEPH detector	56
4.1	Number of fired planes within the last 10 planes for muons and pions	62
4.2	Mean number of clusters per fired plane (CLPLN) for muons and pions after penetration cut	63
4.3	Number of good tracks in the TPC	64
4.4	Energy deposited in ECAL for leptonic events	66
4.5	Acolinearity	66
4.6	Energy deposited in LCAL	67
4.7	Acceptance and resolution for the different detector regions.	70
4.8	Total ECAL wire energy for $x > 0.77$ and $x_{recoil} > 0.77$	72
4.9	Efficiency for muon identification (pair-tag) versus $\cos\theta$ of the track	73
4.10	Efficiency for muon identification (ch-tag) for the different detector bins.	74
4.11	Efficiency for μ veto (ch-tag) for the different detector bins.	75

4.12	Number of local maxima in ECAL clusters	78
4.13	Invariant mass of two ECAL clusters and Bulos mass.	79
4.14	Misidentification probability for charged pions.	81
4.15	Background from $\tau^\pm \rightarrow \text{hadron}^\pm \nu \geq 0 \text{ neutrals}$ for the different detector regions.	82
4.16	Background from muon pairs for the different detector regions.	84
4.17	Number of fired planes within the last 10 planes for electrons	86
4.18	Final momentum distributions for $\tau^\pm \rightarrow \mu\nu\nu$ events in the individual detector regions	87
5.1	Projections onto momentum and angle of the two-dimensional momentum /angular distribution for $\tau^\pm \rightarrow \mu\nu\nu$ events together with best fit	92
5.2	Contour plot for 1σ and 3σ change in the log-likelihood function for the fit in \bar{g}_ν (abscissa) and ξ (ordinate)	97
5.3	Projection onto momentum of the two-dimensional momentum/angular distribution for $\tau^\pm \rightarrow \mu\nu\nu$ events together with best fit and $\xi = \pm 1$	97
5.4	$\bar{g}_\nu(s = M_Z^2)$ versus $\bar{g}_a(s = M_Z^2)$ for the overall ALEPH fit to the forward-backward asymmetries and the widths and the result for this thesis	101
A.1	Ratio Monte Carlo distribution over analytical formula and maximum deviation of the polar angle of the muon from the polar angle of the τ	106
C.1	Definition of alignment constants	113
C.2	Effect of misalignment on D_0	113
C.3	Correction in Φ_0 due to a nonzero dip angle λ	114
C.4	Typical cosmic event	117
C.5	Probability distribution for ITC track fit	118
C.6	Probability distribution for TPC track fit	118
C.7	$D_0^{\text{ALEPH}} - D_0^{\text{TPCSIM}}$ versus D_0	122

List of Tables

2.1	τ^- decay channels (topological and exclusive)	14
2.2	Sensitivities and weights for different decay channels	19
2.3	Predictions and measurements of τ decay parameters	20
2.4	Change in polarization varying g_{a_s} , g_u , and g_a , within reasonable range	35
2.5	Results for check with Monte Carlo (semi-analytical approach), part 1	36
2.6	Results for check with Monte Carlo (semi-analytical approach), part 2	37
2.7	Results for check with Monte Carlo (MC approach)	39
4.1	Angular and momentum bins in the analysis	58
4.2	Acceptance for individual cuts	69
4.3	Acceptance (height and slope)	71
4.4	Efficiencies for muon identification and μ veto in percent for ch-tag and pair-tag for 1990 data excluding cracks	76
4.5	Efficiencies for muon identification and μ veto used for the analysis for all data in percent	76
4.6	Pion misidentification probability and number of background events for hadronic background	80
4.7	Individual contributions to the π^0 -tag sample estimated from Monte Carlo and scaled to data	80
4.8	Number of background events for muon-pair background	83
4.9	Number of $\tau \rightarrow \mu\nu\nu$ candidates and background	88
4.10	Number of $\mu^+\mu^-$ events, luminosity and $\tau \rightarrow \mu\nu\nu$ candidates for different CMS energies	89
5.1	Systematic errors for the different measurements	99
5.2	Comparison of \bar{g}_v and \bar{g}_a measurements within ALEPH	101
5.3	Results and weights for the τ polarization with different channels	102
A.1	Constants for straight line fit to ratio of Monte Carlo distribution and analytical formula	107
C.1	Fit of alignment constants to Monte Carlo simulation	121
C.2	Influence of multiple scattering and momentum cut	121
C.3	Comparison multiple scattering, no multiple scattering and higher statistics	122
C.4	Data reduction for Monte Carlo samples	122
C.5	Interpretation of alignment constants in terms of imperfections and geometrical alignment.	123
C.6	Mean value and width of $x = (D_0 - D_0^{true})/\sigma_{D_0}$	123
C.7	Measured alignment constants for 1989 and 1991	124

Danksagung

Herrn Prof. Dr. K. Kleinknecht danke ich dafür, daß er mir die Teilnahme am ALEPH-Experiment und die damit verbundenen Aufenthalte am CERN und am Imperial College, London, ermöglicht hat. Die physikalische Aufgabenstellung war sehr interessant und führte u.a. zu einer Messung eines bisher unbekanntem Parameters des Standard Modells.

Allen Mitgliedern der Mainzer Arbeitsgruppe danke ich für die gute Arbeitsatmosphäre. Besonders hervorheben möchte ich Herrn Prof. Dr. H. G. Sander und Dr. M. Schmelling, mit denen ich viele fruchtbare Diskussionen geführt habe. Herr Dr. B. Renk war immer ein hilfsbereiter Ansprechpartner bei Problemen mit den Rechnern der Arbeitsgruppe.

Herr Dr. P. Dornan und Herr Dr. R.W. Forty vom Imperial College in London haben mir wertvolle Unterstützung bei dem Projekt der Ausrichtung der ITC und der TPC bei der Rekonstruktion zuteil werden lassen. Ich habe am Imperial College ein sehr angenehme Zeit verbracht.

Die TPC-Gruppe am CERN hat mich bei den Arbeiten für das Laserkalibrationssystem nach besten Kräften unterstützt. Von der Tau-Lepton Arbeitsgruppe der ALEPH-Kollaboration bekam ich viele Anregungen und Hilfe bei aktuellen Problemen. Ganz besonderen Dank möchte ich Herrn Dr. L. Rolandi, Triest, aussprechen, der mich bei dieser Arbeit mit sehr hilfreichen Diskussionen und großem Ideenreichtum unterstützt hat.

Bei Herrn dipl.-phys. A. Stahl, Heidelberg, bedanke ich mich für die gute und fruchtbare Zusammenarbeit während der letzten eineinhalb Jahre.

Herr Dr. R. St.Denis hat die große Mühe auf sich genommen, diese Arbeit auf Fehler in der englischen Sprache sehr sorgfältig durchzusehen. Dafür möchte ich ihm an dieser Stelle danken.

Mein Freund und Mitstreiter, Herr dipl.-phys. F. Steeg, hat maßgeblich dazu beigetragen, daß die Promotion eine rundum schöne Zeit war.

Meiner Frau Claudia danke ich für ihre Geduld und ihre Unterstützung, die mir beim Erstellen dieser Arbeit eine große Hilfe waren. Auch meine Eltern standen mir jederzeit zur Seite.

Diese Arbeit entstand im Rahmen des ALEPH-Experimentes, das vom Bundesministerium für Forschung und Technologie gefördert wird.

Lebenslauf

Anschrift

Dipl.-Phys.
Steffen Roehn
Rheinessenblick 18
D-6551 Hackenheim

Persönliche Daten

geboren am	20.05.1964 in Mainz
Eltern	Wolfgang und Eve-Angela Roehn
Familienstand	verheiratet
Staatsangehörigkeit	deutsch
Konfession	evangelisch

Bildungsgang

1970 – 1974 Besuch der Grundschule (Kleistschule) in Bad Kreuznach
1974 – 1982 Besuch des Gymnasiums am Römerkastell in Bad Kreuznach;
Abschluß mit dem Abitur am 21. Juni 1982
1982 – 1984 Studium der Physik an der Universität Kaiserslautern;
Abschluß mit dem Vordiplom am 27. September 1984
1984 – 1986 Fortsetzung des Physikstudiums an der Universität Karlsruhe;
seit dem Vordiplom Förderung durch die
Studienstiftung des Deutschen Volkes
1986 – 1988 Fortsetzung des Physikstudiums und Erstellung der Diplomarbeit
“Messung des relativen Verzweigungsverhältnisses
 $R_{K_S} = \Gamma(K_S \rightarrow \pi^+\pi^-)/\Gamma(K_S \rightarrow 2\pi^0)$ am Experiment NA31”
am Lehrstuhl von Prof. Dr. Kleinknecht an der Universität Mainz;
wissenschaftlicher Hilfsassistent am Institut für Physik;
Abschluß mit dem Diplom am 7. März 1988
seit 1988 Durchführung der Promotion
am Lehrstuhl von Prof. Dr. Kleinknecht;
wissenschaftlicher Angestellter am Institut für Physik;
Antrag auf Zulassung zur Promotion am 16. August 1990,
Titel der Dissertation: “Measurement of τ Production and Decay
Parameters with the Process $e^+e^- \rightarrow Z^0 \rightarrow \tau^+\tau^-; \tau \rightarrow \mu\nu\tau\nu_\mu$ ”,
Promotionsprüfung am 26. Juni 1991